Charge Transfer in Catalysis Studied by In-situ Microwave Cavity Perturbation Techniques

vorgelegt von
Master of Science
Maria Heenemann
geb. in Köthen/Anhalt

von der Fakultät II - Mathematik und Naturwissenschaften
der Technischen Universität Berlin
zur Erlangung des akademischen Grades

Doktor der Naturwissenschaften
– Dr. rer. nat. –

genehmigte Dissertation

Promotionsausschuss:

Vorsitzender: Prof. Dr. Reinhard Schomäcker
Gutachter: Prof. Dr. Robert Schlögl
Gutachter: Prof. Dr. Peter Hildebrandt
Gutachter: Prof. Dr. Malte Behrens

Tag der wissenschaftlichen Aussprache: 19.07.2017

Berlin 2017

Die Neugier steht immer an erster Stelle eines Problems, das gelöst werden will.

(Galileo Galilei)

Acknowledgements

First, I would like to express my sincere gratitude to my advisor Prof. Dr. Robert Schlögl. I appreciate all the great scientific work opportunities in his department of Inorganic Chemistry at the Fritz-Haber Institut der Max-Planck-Gesellschaft. I greatly thank him for the immense support and extensive guidance during my PhD-days ("Doktorandentage"), project days, and test presentations.

Second, I am extremly grateful to my former supervisor Dr. Maik Eichelbaum. He provided great ideas and gave strong support to my scientific work during his time as group leader of the charge transport group. I also thank for all the guidance and opportunities provided by Prof. Dr. Thomas Risse. With his critical and detailed reviewing process, he significantly improved my scientific work.

Besides my advisors, I would like to thank my additional thesis committee members where I particularly mention Prof. Dr. Peter Hildebrandt and Prof. Dr. Malte Behrens for reviewing my thesis. Prof. Dr. Reinhard Schomäcker is acknowledged for taking the chair of the examination board.

I am deeply grateful to Prof. Dr. Reinhard Stößer for his clear and demonstrative introduction in microwave electronics. My sincere thanks go to Dr. Sabine Wrabetz for her faith in me. I also wish to thank to Prof. Dr. Klaus Hermann for his support at the end of my thesis.

Further, I appreciate all help I received from the members of the former charge transport group: Dr. Christian Heine, Anna Maria Wernbacher, and Elisabeth Hannah Wolf. We had fruitful scientific and nonscientific discussions. Furthermore, I thank Dr. Julia Schumann for the synthesis and preparation of ZnO and ZnO:M samples, Gudrun von der Waydbrink for her help with the construction of the MHE setup, Dr. Olaf Timpe for XRF analysis, Maike Hashagen for BET measurements, and Dr. Gerado Algara-Siller for HR-TEM images.

In addition, I would like to thank all members of our department and our collaborators for their support. Here, I mention all my coauthors in alphabetical order: Dr. Lukas Braun, Dr. Sébastien Cap, Ann-Kathrin Elger, Dr. Elias Frei, Dr. Frank Girgsdies, Dr. Marc Gluba, Dr. Michael Hävecker, Prof. Dr. Christian Hess, Dr. Tobias Kampfrath, Marie-Mathilde Millet, and Dr. Annette Trunschke.

My special thanks go to the colleagues of electrical and mechanical workshop, who invested a lot of time to construct my microwave cavities and to solve all my problems.

The International Max-Planck-Research School "Functional Interfaces in Physics and Chemistry" is gratefully acknowledged for its support during the discussion meetings, the informative block-courses, and all conference trips. German research foundation (DFG project: EI 950/1-1,2) is acknowledged for financial support.

Finally, I will never forget the fun and jokes during all the conferences, coffee breaks, after-work hangouts, and on our fantastic department trips.

Last but not least, I would like to express heartfelt thanks to my family, and my dear Henry for his unsurpassed support and extensive day-by-day encouragement.

Abstract

The efficient use of our natural resources and the reduction of CO_2 emissions are key aspects for future industrial processes. Important challenges are to convert hydrocarbons and to activate CO_2 into useful chemical intermediates. In order to improve such chemical reactions, a fundamental understanding of the underlying mechanisms is required. The present thesis considers two heterogeneously catalyzed reactions: (i) the selective oxidation of propane to acrylic acid over vanadyl pyrophosphate and (ii) the CO_2 activation over Cu/ZnO based catalysts. The electronic structure changes modified by the gas phase chemical potential were monitored by microwave cavity perturbation and microwave Hall effect measurements. These contact-free techniques enable the determination of charge carrier dynamics in a working catalyst – in particular its electrical microwave conductivity, microwave Hall mobility, and absolute charge carrier concentration.

An improved in-situ microwave conductivity setup based on previous work of Eichelbaum *et al.* is utilized with cylindrical TM_{0n0} ($n = 1, 2$) cavities. The validity of this experimental setup is tested with differently promoted ZnO catalyst supports at high temperature under reducing and oxidizing gas feed conditions. In line with results obtained with a contact method the n-type conductivity is identified for all catalyst supports. Furthermore, frequency-dependent conductivity measurements reveal a dominating contribution of free charge carriers at high-temperature in accordance with the Drude model.

Based on the reference study described above, the industrial catalyst vanadyl pyrophosphate is investigated in the selective oxidation of propane. Water in the propane feed leads to a decrease of the conductivity, and the selectivity towards the industrially important intermediate acrylic acid increases. This observation is complemented by near-ambient pressure X-ray photoelectron-, and X-ray absorption spectroscopy. The surface elemental composition (enrichment of V^{5+} species) is modified by water and at the same time the energy position of the valence band onset is unaffected. Therefore, a change of the charge carrier mobility is discussed for the decrease in conductivity.

Another part of this thesis deals with the development of an in-situ microwave Hall effect setup. To the best of my knowledge, the charge carrier mobility is measured for the first time under reaction conditions with a modified bimodal TE_{112} cavity. As a proof of concept, Cu/ZnO based catalysts are tested in the reverse water-gas shift reaction for CO_2 utilization. Additionally, these catalysts are promoted with different amounts of Al^{3+}. The change of charge carrier concentration in the catalyst due to the promoting agent is quantified. It turns out that, the concentration of electrons as the majority type of charge carrier increases with increasing Al^{3+} content. Moreover, the significant increase is accompanied by an increase in CO formation and a decrease in apparent activation energy. The increased availability of electrons under reaction conditions allow an enhanced electron transfer to form the proposed intermediate CO_2^- which is further converted to CO. In this special case, the experimentally observed effect is in perfect agreement with the electronic theory of catalysis, where such a relationship between charge carrier concentration and catalytic performance is already predicted.

In summary, this thesis demonstrates that the consideration of the so-called electronic factor in catalysis is a crucial criterion for catalyst optimization processes.

Zusammenfassung

Die effiziente Nutzung unserer nachwachsenden Rohstoffe und die Verringerung der CO_2 Emissionen sind wichtige Aspekte für die zukünftige Chemikalienproduktion. Um diese meist heterogen katalysierten Reaktionen zu optimieren, ist ein fundamentales Verständnis des katalytischen Mechanismus erforderlich. In der vorliegenden Dissertation wurden die (i) selektive Propanoxidation zu dem industriell nutzbaren Zwischenprodukt Acrylsäure über Vanadylpyrophosphat und die (ii) CO_2 Aktivierung über Cu/ZnO basierte Katalysatoren näher betrachtet. Die dynamische Änderung der elektronischen Katalysatorstruktur, induziert durch die chemische Gasphase, wurde vor allem mit Hilfe der Mikrowellen-Resonator-Störungsmethode und des Mikrowellen-Hall-Effektes analysiert. Diese beiden kontaktfreien Techniken ermöglichen eine Charakterisierung pulverförmiger Katalysatorsysteme – im Speziellen ihre elektrische Mikrowellenleitfähigkeit, ihre Mikrowellen-Hall-Beweglichkeit und ihre absolute Ladungsträgerkonzentration.

Für die präzise Bestimmung der Volumenleitfähigkeit wurde ein experimenteller Aufbau, welcher auf Vorarbeiten von Eichelbaum *et al.* beruht, mit zylindrischen TM_{0n0} ($n = 1, 2$) Resonatoren entwickelt. Dieser Versuchsstand wurde mit promotierten ZnO Katalysatorträgern bei hoher Temperatur unter reduzierenden und oxidierenden Bedingungen getestet. Es ergab sich eine gasphasenabhängige Elektronenleitfähigkeit für alle Katalysatorträger, die durch Kontaktmessungen bestätigt wurde. Weiterhin konnte mit einer frequenzabhängigen Leitfähigkeitsmessung gezeigt werden, dass bei hohen Temperaturen freie Ladungsträger nach dem Drude Modell einen dominierenden Einfluss haben. Basierend auf diesen Referenzexperimenten wurde der Selektivoxidationskatalysator Vanadylpyrophosphat in der Propanoxidation unter dem Einfluss von Wasserdampf untersucht. Wasser im reaktiven Gasgemisch führte zu einer Abnahme der Leitfähigkeit während es gleichzeitig zu einer Selektivitätszunahme hinsichtlich der Acrylsäure kam. Zum näheren Verständnis der Leitfähigkeitsabnahme wurde die elektronische Struktur der Katalysatoroberfläche näher untersucht. Eine Verbindung zwischen der Ladungsträgermobilität (und einer Oberflächendipoländerung) wurde diskutiert, welche durch die effektive Masse sowohl die Valenzbandstruktur als auch die Leitfähigkeit verknüpft ist.

Ein weiterer Teil dieser Dissertation war die Entwicklung einer in-situ Mikrowellen-Hall-Effekt Anlage unter Verwendung eines bimodalen TE_{112} Resonators. Nach meinem jetzigen Kenntnisstand kann mit dem entwickelten Aufbau die Ladungsträgermobilität zum ersten Mal unter Reaktionsbedingungen vermessen werden. Als Modelreaktion wurden Kupfer-Zink basierte Katalysatoren in der reversen Wassergaskonvertierungsreaktion für die CO_2 Nutzung getestet. Zusätzlich dazu wurden die Katalysatoren mit verschiedenen Al^{3+} Konzentration promotiert. Mit ansteigender Al^{3+} Dotierung nahm die Ladungsträgermobilität ab, wohingegen die Ladungsträgerkonzentration stark anstieg. Weiterhin wurde ein Anstieg in der CO Bildung und ein Absinken der Aktivierungsenergie beobachtet. Die bessere Verfügbarkeit von Elektronen, die als Hauptladungsträger fungierten, ermöglichten einen gesteigerten Ladungstransfer zur Bildung des postulierten Zwischenzustandes CO_2^-, der wiederum weiter zu CO reagiert. In diesem besonderen Fall ergab sich eine sehr genaue Übereinstimmung mit den halbleiterphysikalischen Konzepten, die diesen engen Zusammenhang zwischen Ladungsträger und katalytischen Aktivität vorhersagten.

Zusammenfassend demonstriert diese Arbeit, dass die Einbindung des sogenannten elektronischen Faktors ein besonders wichtiges Kriterium für die Optimierung von Katalysatoren zur Entwicklung nachhaltiger Prozesse ist.

Contents

1 Introduction

Recently, the scientific effort in energy-related research has been increased considerably [1]. This is, amongst others, due to the oil price shock in 2000 [2] or to primary greenhouse issues [3,4] discussed extensively. In order to optimize corresponding chemical reactions at an industrial level, an understanding of underlying catalytic mechanisms at an atomic level is substantial [5–7]. To develop efficient catalytic systems, concepts like site isolation of regenerative redox active metal centers were phenomenologically applied in catalysis. However, reaction induced changes are not implement in these strategies. Several studies emphasize that the electronic structure, especially the surface electronic structure, plays an important role to understand the working mode [6,7]. Insight into corresponding processes can be achieved by model systems and investigations in technical applications under reaction conditions. In the latter approach, the geometric and electronic structure of the catalyst needs to be investigated in order to understand their influence on desired reaction products [6]. This link between structure and activity is of utmost importance for catalyst optimization. Due to technical and physical limitations, only few techniques allow the study of bulk and surface changes at high temperatures and pressures.

In this thesis, contact-free in-situ electrical conductivity, and mobility measurements are used to probe the (electronic) structure. Here, the focus is on two energy-related heterogeneously catalyzed reactions for the in-situ characterization, the selective oxidation of propane and the hydrogenation of CO_2. Chapter 1.1 gives a general introduction highlighting the importance of conductivity measurements in catalysis. Chapter 1.2 addresses the selective oxidation of propane catalyzed by vanadyl pyrophosphate. This reaction was chosen in response to the need for efficient selective oxidation catalysts caused by the oil crisis and to the limited amount of fossil fuels. Chapter 1.3 presents results for the hydrogenation of CO_2 by the reverse water-gas shift reaction over Cu/ZnO based catalysts. This reaction was examined in order to obtain a more detailed mechanistic understanding of the CO_2 activation which may pave the way for the efficient conversion into valuable chemical intermediates.

1.1 The role of charge transfer in catalysis

The charge transport in a heterogeneous semiconducting catalyst is strongly affected by charge transfer processes between adsorbent and adsorbate.

The results of early studies showed the applicability of electrical conductivity measurements to monitor these processes, e.g., propene over a VMgO oxide[8] catalyst or a $MoVTeNbO_x$ catalyst[9], propane over a MoVSbNbO catalyst[10], or the oxidative coupling of methane[11]. Owing to its industrial importance, also the $(V^{IV}O)_2P_2O_7$ catalyst was extensively investigated during the oxidation of n-butane[12–14].

In the past, contact techniques pressing the powder catalyst between two metal electrodes were applied in most cases. However, the stability of the electrical contact between the electrode and the pressed sample is challenging[15]. Here, a contact-free alternative is the measurement of the conductivity at high frequencies. This high frequency technique is known as microwave cavity perturbation technique[16]. In 2012, Eichelbaum *et al.* introduced this microwave approach in the field of heterogeneous catalysis as an in-situ method[15]. The cavity perturbation technique was successfully applied to selective oxidation reactions over vanadium based catalysts[17–22], as well as to probe the redox properties of ZnO model catalysts[23]. The varying conductivity was mainly attributed to changes in the charge carrier density together with an almost constant charge carrier mobility[12,15,18]. However, providing experimental proof for constant carrier mobility is challenging. In particular, when it comes to polycrystalline materials, the low mobility and the already mentioned contact-related problems have to be taken into account.

The microwave Hall effect technique is another technique to measure charge carrier mobility of powder samples in a contact-free experiment[24]. In the past, this Hall technique was used to measure Hall mobilities of bio macromolecules[25–29], organic semiconductors[30], single crystals[28,31–36], and perovskites[37]. In addition, it has proven useful in analyzing ZnO powder[28,38–42]. Na *et al.* reported a change in conductivity and carrier mobility after ex-situ treatment of ZnO powder under different gas atmospheres and at various temperatures[38,39]. The mobility of ZnO decreased after evacuation at 673 K, due to the formation of oxygen vacancies. Simultaneously, the conductivity and the electron density increased[39]. Surface related charge transfer processes are also relevant in catalysis. Walters *et al.* developed a two-charge carrier model for ZnO to elucidate the importance of surface charge carriers[41]. In his theoretical treatment, the change in conductivity at different gas atmospheres is induced by a variation in surface electron density. Here, both bulk and

surface mobilities are assumed to be constant. However, it is still unclear how the carrier mobility and carrier density variations influence the working mode of a real catalyst.

To predict the working mode of the oxidation catalyst, a so-called electronic factor theory was proposed[43–45]. In this simplified semiconductor theory, which is one example among others in catalysis research (e.g., site isolation and phase cooperation model[46]), the Fermi-potential of a semiconducting catalyst and the redox potential of adsorbates play an important role. This potential was described as the driving force for charge transfer[43]. The first experimental proof was published by Eichelbaum *et al.* where this surface potential barrier was suggested as a descriptor for selective alkane oxidation catalysts[47].

1.2 Selective oxidation of propane catalyzed by vanadyl pyrophosphate

Natural gas contains, among others, methane, ethane, butane, and propane. The petrochemical industry is based on the efficient and direct oxidation of these short alkanes into olefins or oxygenates. Therefore, the improvement of selective oxidation catalysts is essential. For instance, the industrial production of acrylic acid is performed by a two-step oxidation process via acrolein from propane[48]. Acrylic acid is needed for the production of plastics (e.g., polyacrylic acid), pharmaceutical binders, coating, etc. Direct conversion with efficient catalysts would reduce the process complexity, minimize waste, and increase efficiency[49]. At present, the most promising candidate for direct acrylic acid production is a $MoVTeNbO_x$ catalyst[50].

From a chemical point of view, the acrylic acid formation requires the transfer of eight electrons, the abstraction of four hydrogen atoms from the substrate, and the insertion of two oxygen atoms (cf. Scheme 1.1). Furthermore, a redox active catalyst is needed to guarantee a dynamic cycle.

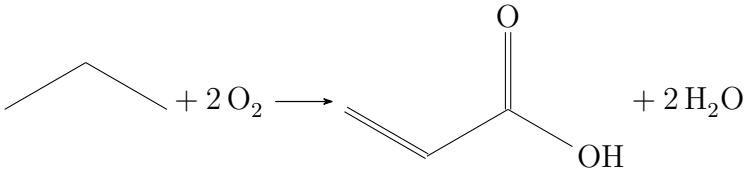

(1.1)

Scheme 1.1: *Selective oxidation of propane to acrylic acid.*

The vanadium-phosphorous oxide catalyst (VPO) is the most widely applied catalyst for the selective oxidation of n-butane to maleic anhydride. The BASF company synthesis maleic anhydride over VPO which consists mainly of the a single $(V^{IV}O)_2P_2O_7$ phase (vanadyl pyrophosphate, VPP)[51–53]. However, only few peer-reviewed studies have evaluated the role of VPO-based catalysts for the selective oxidation of propane to acrylic acid[48,54,55]. Even though propane is in the same class of homologous compounds as butane, it is still not clear why VPP could not be used as a catalyst in the acrylic acid synthesis from propane oxidation.

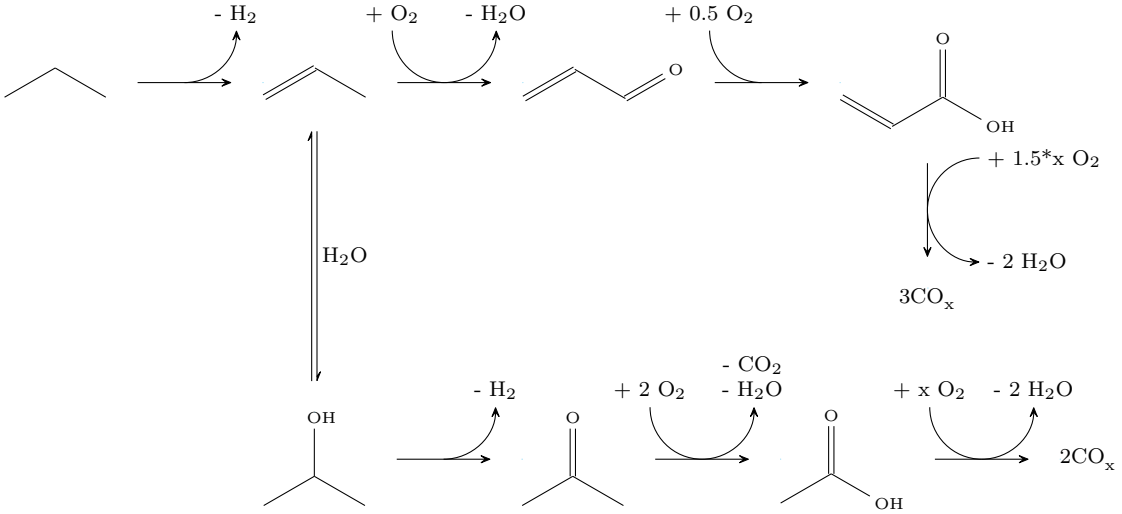

Scheme 1.2: *Proposed reaction pathways for selective oxidation of propane over a Te-VPO catalyst (according to[54]).*

Ai found an acrylic acid yield of 10 % and an acrylic acid selectivity of 37 % over a Te doped VPO catalyst[54]. Unfortunately, a very low productivity with a high oxygen feed content was reported which is not appropriate for industrial applications[49]. In a subsequent study, an acrylic acid yield of 10 % with a propane conversion of 45 % was reported, but at the same time acetic acid was found with a yield of 5 %[55]. A V/P ratio of 1.15 gave the highest acrylic acid selectivity. No significant influence of promoters either TeO_2 nor SO_3 was published[55]. When adding steam to the reaction mixture, the selectivity towards acrylic acid increased. The authors explained this phenomena with an enhanced desorption rate[48,49,56,57].

In this context, Ai proposed a reaction pathway with Te doped VPO as a catalyst where propane is dehydrogenated to propylene in a first step[54,55]. Scheme 1.2 shows two reaction pathways of propylene. In the upper part, propylene is oxidized to acrolein and to acrylic acid. In the lower part, propylene is hydrolyzed to 2-propanol, and dehydrogenated to

acetone. In the next step, acetone is oxidized to acetic acid. At the end, the total oxidation products CO and CO_2 are formed. Different other reaction pathways were published depending on the catalytic system[58] for example $MoVTeNbO_x$ catalyst[59,60], NiMoTeP oxide catalyst[61].

1.3 Hydrogenation of CO_2 via reverse water-gas shift reaction

Efficient CO_2 activation yields valuable chemicals, reduces the greenhouse gas effect, and avoids undesired climate changes[3,62,63]. CO_2 is a thermodynamically stable molecule and does not react easily with other molecules[64]. Possible CO_2 conversion reactions are mainly divided into three classes: reduction, addition or coupling, and acid-base reaction[65]. The process investigated in most cases is the hydrogenation of CO_2 to yield liquid fuels (e.g., methanol[66]) or oxygenates. These liquid fuels have a high energy density and allow safe storage[65]. Methanol, which is an industrially important intermediate, is commercially produced from synthesis gas ($CO/CO_2/H_2$) over a Cu based catalyst[67]. In the so-called CAMERE process CO is produced via reverse water-gas shift reaction and further hydrogenated to methanol[68].

The hydrogenation of CO_2 (cf. Scheme 1.3) has a favorable reaction enthalpy (ΔH) due to the formation of water[64].

$$CO_2 + H_2 \rightleftharpoons CO + H_2O \tag{1.2}$$

Scheme 1.3: *Reverse water-gas shift reaction, with* $\Delta H_{298\ K} = 41.2\ kJ\ mol^{-1}$ *[64].*

The mechanism of the reverse water-gas shift reaction over Cu based catalysts is still controversial. The most often proposed reaction pathways are the redox and the associative formate mechanism[69–72]. In the latter mechanism, formate is frequently described as spectator due to its high stability[73]. Scheme 1.4 presents the surface redox mechanism over a Cu based catalyst. In this mechanism, the dissociative CO_2 adsorption is identified as the rate-limiting step[69,71]. The charge transfer occurs at the Cu surface which is oxidized and reduced ($Cu^0 \rightleftharpoons Cu^I$)[70]. The direction of charge transfer for the Cu/ZnO catalyst, which is proposed as a Schottky-Mott-junction, is still under debate[74–76]. However, this charge transfer and binding to the surface might play a crucial role in CO_2 activation[64]. The

importance of the Cu/ZnO interface was shown in a recent study[77]. A similar finding was reported by Graciani *et al.* and Senanayake *et al.*, who considered a CeO_X/Cu(111) and Cu/ZnO(000$\bar{1}$) interface as an important adsorption and reaction sites.[78,79] At this metal oxide interface, multiple intermediates like carboxylate or formates are formed[73,78,79]. For the Cu/ZnO system, the importance of Cu for the CO_2 activation is not fully explored, but it is generally accepted that Cu is the active phase in the methanol synthesis[67]. A recent study has demonstrated that methanol synthesis activity varied with the coverage of zinc atoms on the copper nanoparticles[80]. The authors showed experimentally and theoretically that the ZnO nanoparticle size determines the zinc coverage on the copper surface which controls the catalyst activity[80,81].

$$CO_2 + 2\,{}^* \rightleftharpoons CO^* + O^* \tag{1.3}$$
$$CO^* \rightleftharpoons CO + {}^* \tag{1.4}$$
$$H_2 + 2\,{}^* \rightleftharpoons 2\,H^* \tag{1.5}$$
$$2\,H^* + O^* \rightleftharpoons H_2O^* + 2\,{}^* \tag{1.6}$$
$$H_2O^* \rightleftharpoons H_2O + {}^* \tag{1.7}$$

Scheme 1.4: *Surface redox mechanism for the reverse water-gas shift reaction, where * represents an active vacancy*[71].

1.4 Outline of the present thesis

In the present thesis, the role and influence of charge transfer as well as charge transport at heterogeneous polycrystalline catalysts under reaction conditions is investigated. Another goal is the implementation of contact-free conductivity and mobility techniques for their application in catalysis. The microwave cavity perturbation and the microwave Hall effect are applied. Chapter 2 explains the physical basis of these two contact-free techniques.

Furthermore, the thesis proposes procedures to increase the sensitivity of in-situ conductivity measurements with TM_{0n0} cavities where the specific transverse magnetic (TM) field is explained in Chapter 2.1.1. The second method applied in this thesis is the resonant microwave Hall effect technique to measure the Hall mobility in a contact-free manner. Based on previous research, the development of an in-situ microwave Hall effect setup with a so-called bimodal cavity was another task of this thesis.

Chapter 3 presents the experimental results. Chapter 3.1 describes the conductivity measurements for unpromoted and promoted (Mg, Al, and Ga) polycrystalline ZnO. The conductivity was measured in its dependence on frequency, temperature and gas phase (O_2, and H_2). For these experiments, the improved conductivity setup using TM_{0n0} cavities was used. The gas-phase-induced changes were compared with contact conductivity measurements to validate the setup. The TM_{0n0} cavities (J-, C-, S-, and L-band) were investigated in different TM modes (TM_{010} and TM_{020}). These modes allow a multi-frequency conductivity analysis at different temperatures. The frequency-dependent measurement gives a systematic insight into the nature (local and itinerant) of charge carriers. The measurements in a GHz range (1 to 12 GHz) are complemented by contact-free conductivity experiments in a THz range (500 to 2500 GHz) using Terahertz spectroscopy.

Chapter 3.2 discusses the influence of steam on the electronic behavior of an industrial vanadium-phosphorous oxide catalyst which consists mainly of $(V^{IV}O)_2P_2O_7$. This catalyst was tested in selective oxidation of propane in the presence and absence of steam. These changes in conductivity were complemented by in-situ near-ambient pressure X-ray photoelectron, and X-ray absorption spectroscopy.

Chapter 3.3 demonstrates the evaluation and validation of an in-situ microwave Hall effect setup. This setup was successfully applied to a quantitative charge carrier analysis of Cu/ZnO based model catalysts. Chapter 3.4 describes these results and their influence on the charge transfer to activate CO_2 via reverse water-gas shift reaction.

Chapter 4 presents a final conclusion of the findings obtained by the thesis work.

2 Experimental methods

This Chapter outlines the two resonant methods of measuring the dielectric properties at microwave frequencies. Chapter 2.1 presents the microwave cavity perturbation technique while Chapter 2.2 introduces the resonant microwave Hall effect technique[a].

2.1 Microwave cavity perturbation technique

In the cavity perturbation method a sample is placed in the electric field inside a cavity to measure its complex electrical permittivity which is related to the conductivity of the sample. Chapter 2.1.1 describes the boundary condition for a cylindrical cavity resonator and the principle of measurement. Chapter 2.1.2 discusses the advantages and disadvantages of this method. Chapter 2.1.3 describes the experimental setup which was developed in this thesis work.

2.1.1 Principle of measurement

Cylindrical cavity resonator

In the experiment, a sample is put into an oscillating electric and magnetic field which is confined by a cylindrical cavity. This requires an understanding of the spatial and time dependence of these fields in order to appreciate the experimental data. Further information can be found in Jackson and Frieser[82,83]. Maxwell's equations are the main basis for explaining the propagation of electromagnetic fields inside a cavity[84]. These electromagnetic fields are excited by a coupling which will be analyzed at the end of this section.

Figure 2.1.1 illustrates a cylindrical cavity resonator. In the empty cylindrical cavity there are two types of field configurations. Depending on the boundary conditions, the

[a] All reported equations for the microwave conductivity and microwave Hall mobility are based on the cited literature and used throughout this thesis work.

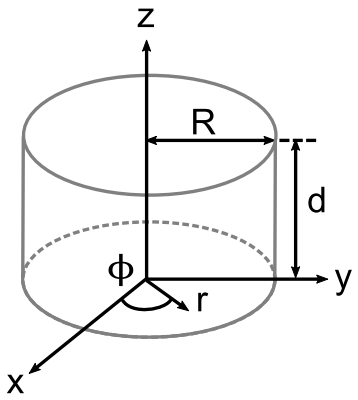

Figure 2.1.1: *Geometric structure of a cylindrical cavity resonator.*

fields can be divided into transverse magnetic (TM) and transverse electric (TE) waves. Here, **E** is the electric field and **B** is the magnetic induction[b]. These two modes depend on the axial component z and can be distinguished as follows: $\mathbf{B}_z = 0$ for a TM mode, $\mathbf{E}_z = 0$ for a TE mode. For illustration purposes, the electric field **E** is divided into a transverse and parallel component ($\mathbf{E} = \mathbf{E}_z + \mathbf{E}_t$). Hence, for TM fields it is required that transverse component $\mathbf{E}_t$ disappears at z = 0 and z = d (where d is the cavity height, cf. Figure 2.1.1). This is valid for cavity walls with infinite conductivity, and the cavity is filled with a lossless dielectric.

The cylindrical cavity resonator shown in Figure 2.1.1 has a height of d and an inner radius of R. The electric field inside a cylindrical TM_{mnp} cavity has three components: radial (E_r), angular (E_Φ), and longitudinal (E_z). The integers m, n are related to the (transverse) x and y directions (m = 0, 1, 2,... and n = 1, 2,...) and p refers to the z direction (p = 0, 1, 2,...). The notation of TM_{mnp} and TE_{mnp} is used throughout this thesis. The general expression of the TM_{mnp} electric field distribution in cylindrical coordinates is given by[83]

$$\begin{bmatrix} E_r \\ E_\phi \\ E_z \end{bmatrix} = \begin{bmatrix} -\frac{a_{mn}p\pi}{Rd} J'_m\left(\frac{a_{mn}}{R}r\right) cos\left(m\phi\right) sin\left(\frac{p\pi}{d}z\right) \\ \frac{1}{r} J_m\left(\frac{a_{mn}}{R}r\right) \frac{mp\pi}{d} sin\left(m\phi\right) sin\left(\frac{p\pi}{d}z\right) \\ \left(\frac{a_{mn}}{R}\right)^2 J_m\left(\frac{a_{mn}}{R}r\right) cos\left(m\phi\right) cos\left(\frac{p\pi}{d}z\right) \end{bmatrix} \tag{2.1}$$

where J_m and J'_m define the mth order of the Bessel function, and its first derivative, a_{mn} is the nth order root of the mth order Bessel function. The roots of the Bessel function

[b]The magnetic induction $\boldsymbol{B}$ is proportional to the magnetic field $\boldsymbol{H}$ according to, $\boldsymbol{B} = \mu\boldsymbol{H}$.

a_{mn} are tabulated[82,85]. With the known electric field distribution, the resonance frequency f_{mnp} (often defined as cut-off frequency) of a TM mode inside a cavity resonator is given by[82]

$$f_{mnp} = \frac{c}{2\pi\sqrt{\mu\varepsilon}}\sqrt{\left(\frac{a_{mn}}{R}\right)^2 \left(\frac{p\pi}{d}\right)^2} \tag{2.2}$$

where c is the speed of light, μ is the relative permeability and, ε is the permittivity inside the cavity.

For example, the lowest TM_{mnp} mode has $m = 0$, $n = 1$, and $p = 0$. The a_{01} has a value of 2.405[82]. The X-band cavity in the experiment has an inner radius R of 0.125 m, μ and ε are assumed to be 1. Consequently, this cavity has a resonance frequency f_{010} of 9.1 GHz. The corresponding resonance wavelength λ_{010} is 0.033 m^{-1}. As a result of this example, if R is larger, the resonance frequency f_0 is lower. Furthermore, this mode is independent of the height of d.

In practice, an external source (e.g., network analyzer) transmits energy to the cavity which is so-called coupling. As was mentioned in the introduction of this Chapter, the coupling of microwaves into a resonator plays an important role. Three basic methods of coupling energy into a cavity are reported: (i) probe, (ii) loop, and (iii) aperture coupling[86]. In probe coupling, a wire is located in the maximum of the electric field (capacitive coupling coefficient). Whereas in loop coupling, the loop is located in the maximum of the magnetic field (inductive coupling coefficient)[87]. Furthermore, the coupling coefficient κ specifies the strength of the coupling, where $\kappa > 1$ describes overcoupled, and $\kappa < 1$ is undercoupled. Under critical coupling ($\kappa = 1$) conditions, the impedance of the microwave cavity and the microwave transmission line is matched[88]. In electron paramagnetic resonance spectroscopy, the microwave is coupled via an iris (aperture coupling), which consists of an iris hole and iris screws, into the cavity. The critical coupling conditions are achieved by moving the iris screws up and down. By this movement, the impedance of both the cavity and the waveguide are matched.

Microwave conductivity

The cavity perturbation technique was pioneered by Slater[16]. This technique is widely used to perform complex electrical permittivity ($\varepsilon = \varepsilon_1 + i\varepsilon_2$) and complex magnetic permeability ($\mu = \mu_1 + i\mu_2$) measurements[24,89]. Here, the magnetic permeability was ignored. The present thesis focused on the electrical permittivity which is related to the electrical microwave conductivity. To evaluate the electrical conductivity from these

parameters, the general expression for small-object perturbation inside a cavity is introduced in the following. To obtain the equation for this expression, a resonant cavity with a perfect geometry, which is made of a perfectly conducting material, is assumed. Furthermore, the original medium inside the cavity is lossless and the sample is homogeneous and smaller, compared with the size of the cavity. Additionally, the electromagnetic field is assumed not to change when the sample is introduced.

After various transformations (more details are shown in Chen *et al.*[24], cf. page 253 ff.), the following equation is obtained taken on small-object perturbation for relative frequency differences

$$\begin{aligned} \frac{\omega_l - \omega_e}{\omega_e} &\approx -\frac{\int_{V_S} \left(\Delta\varepsilon \boldsymbol{E}_e^* \cdot \boldsymbol{E}_l + \Delta\mu \boldsymbol{H}_e^* \cdot \boldsymbol{H}_l \right) dV}{\int_{V_C} \left(\varepsilon_e \boldsymbol{E}_e^* \cdot \boldsymbol{E}_l + \mu_e \boldsymbol{H}_e^* \cdot \boldsymbol{H}_l \right) dV} \\ \Delta\varepsilon &= \varepsilon_l - \varepsilon_e \\ \Delta\mu &= \mu_l - \mu_e \end{aligned} \tag{2.3}$$

where V_C and V_S are the volumes of the cavity and sample, ω_e and ω_l are the resonant angular frequencies of the empty cavity and sample-loaded cavity, respectively. $\mathbf{E}_{e,l}$ refer to the electric field of the empty and sample-loaded cavity. The electric fields are coupled with the corresponding magnetic fields $\mathbf{H}_{e,l}$ according to Maxwell's equations, $\Delta\varepsilon$ and $\Delta\mu$ are the complex permittivity and complex permeability, respectively. Here, the difference $\Delta\varepsilon$ and $\Delta\mu$ corresponds to the sample (subscript l) and to the cavity (subscript e).

Based on equation 2.3, more simplified equations have been derived to determine the complex permittivity of a sample[24]. This is achieved by first transforming the complex angular frequency ω of a resonant cavity to the real frequency f as well as the quality factor Q according to equation 2.4.

$$\omega = \omega_r + i\omega_i \ , \ \omega_r = 2\pi f \ , \ Q = \frac{\omega_r}{2\omega_i} \tag{2.4}$$

Then, the cavity perturbation equations used throughout this thesis are given by

$$\frac{f_e - f_l}{f_e} = A(\varepsilon_1 - 1)\frac{V_S}{V_C} \tag{2.5}$$

$$\frac{1}{Q_l} - \frac{1}{Q_e} = B\varepsilon_2 \frac{V_S}{V_C} \tag{2.6}$$

where A and B are cavity constants, f_e and f_l are the empty and sample-loaded frequencies, Q_e and Q_l are the quality factors of the empty and sample-loaded cavity.

The quality factor Q of a resonant cavity can be shown to describe the ratio of the total energy storage in the cavity and the average energy dissipation within the cavity (cf. equation 2.4)[20,24]. Experimentally, Q is obtained from equation 2.8 of Chapter 2.1.3 for the empty and the sample-loaded cavity, respectively. The cavity constants A and B in equation 2.5 and 2.6 are determined by a calibration with materials of known permittivity[c] or by theory for a known electric field distribution of a specific resonant mode.

Equation 2.5 and 2.6 are valid with the following four assumptions: (i) the sample perturbation does not change the field distribution in the cavity; (ii) the medium inside the cavity is vacuum ($\mu_e = \mu_l$ = vacuum permeability μ_0, and ε_e = vacuum permittivity ε_0); (iii) The stored energy is approximately the same for the loaded and empty cavity; (iv) The quality factors of loaded and empty cavity are measured at the same resonance frequency[24,91].

Considering these assumptions, the effective microwave conductivity σ of the sample is given by

$$\sigma = \varepsilon_0 \omega_l \varepsilon_2 \tag{2.7}$$

where σ can be transformed into bulk values using the effective medium approximation (e.g., Landau-Lifshitz-Looyenga[92–94] Maxwell-Garnett, or Bruggeman[15] formalism). The Landau-Lifshitz-Looyenga formalism was applied throughout this thesis due to its suitability for semiconducting powder materials in the micro- and radio-wave regime[20,94].

2.1.2 Advantages and disadvantages

The main advantage of the cavity perturbation method using cylindrical cavities compared with conventional contact methods is the contact-free measurement. Further, cylindrical cavities are very sensitive due to their higher quality factor compared with rectangular cavities[24]. These cylindrical cavities are stable, simple to build, and their standing waves easily tunable (cf. equation 2.2). The simultaneous measurement of two modes (the first TM_{010} and the second TM_{020} mode) at the same time is possible and saves measuring time when implementing two coupling loops (left and right side of the cavity). Additionally, the sample position in the electric field maximum of TM_{0n0} cavities allows a high sensitivity for small conductivity variations. This conductivity is measured as a bulk property since the microwaves pervade the complete sample[24]. Altogether, resonant methods

[c] The reference sample and the investigated sample must have the same geometry, identical positions in the cavity or rather in the electric field, and must resonate in the same frequency range (with the same mode of operation)[90].

are more accurate and sensitive for heterogeneous semiconducting catalysts compared with nonresonant methods[15,17,18,20–22,24].

From a practical point of view, one disadvantage is the decrease of the quality factor of the empty cavity due to surface roughness, imperfect construction, and a deviation from the ideal cavity shape by inserting holes. In addition, the measurement is limited to a certain frequency range determined by the cavity dimension. The principle of measurement may fail when measuring metals or insulating materials, because the assumptions made in Chapter 2.1.1 for the small-object perturbation (quasi-static approximation) might not be valid.

2.1.3 Experimental setup

The first in-situ microwave cavity perturbation (MCPT) setup was published by Eichelbaum *et al.* using a cylindrical X-band TM_{110} cavity[15]. This setup was modified during the present thesis work. Figure 2.1.2 illustrates the improved MCPT setup with the TM_{0n0} cavity in a sketch. This TM_{0n0} cavity can be changed to achieve a broad frequency range (from L-band to J-band, cf. Chapter 3.1).

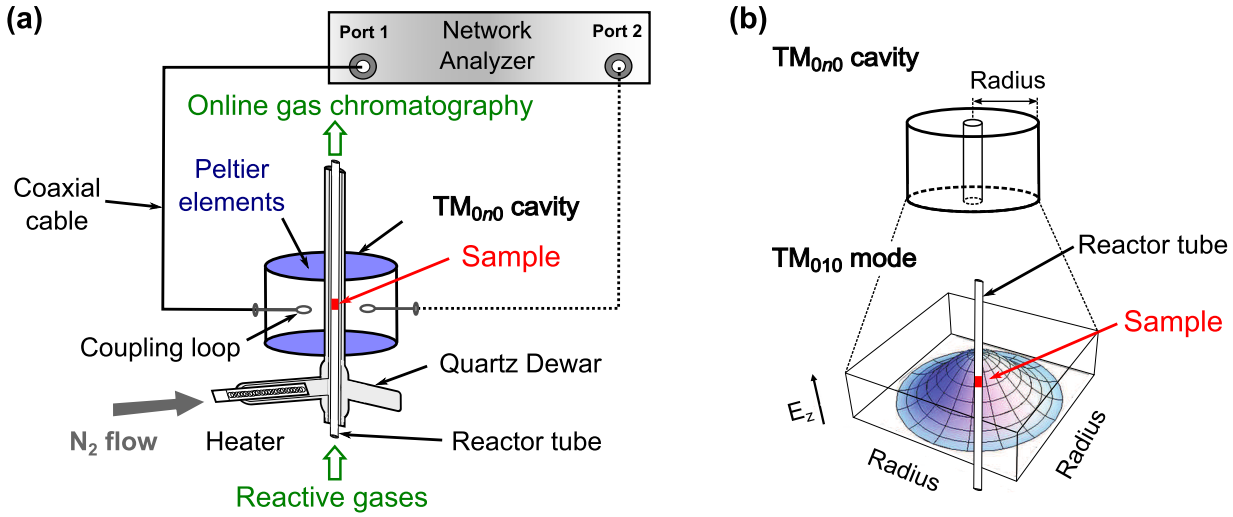

Figure 2.1.2: ***(a)*** *Sketch of the MCPT setup using a cylindrical TM_{0n0} cavity allowing the investigation of powder samples in a fix-bed flow-through reactor under reaction conditions.* ***(b)*** *Sketch of the implementation of the reactor tube and the position of the sample in the electric field E_z of a TM_{010} mode shown at the bottom.*

In the previous investigation, a TM_{110} cavity was used where the microwave was coupled via an iris screw[15]. In this work, a coupling loop inductively couples the microwaves into

the TM_{0n0} cavity. This enhances the measurement stability and facilitates the coupling due to easy rotations of the loop wire. The vector network analyzer is connected via a semi-rigid coaxial cable with the cavity and used in reflection mode. The network analyzer measures the complex reflection factor (defined by the ratio between incoming power and outcoming wave) to obtain f and Q. Experimentally, Q is expressed by the ratio of the resonance frequency and the full width at half maximum (Δf) of the power peak[15,20] i.e., by

$$Q_e = \frac{f_e}{\Delta f_e}, Q_l = \frac{f_l}{\Delta f_l} \tag{2.8}$$

where e represents the empty and l the sample-loaded cavity.

The fix-bed flow-through reactor is connected to a gas supply. The gas supply can introduce various gas mixtures, and the effluent gas flow is analyzed by an online gas chromatograph. Additionally, the reactor tube is surrounded by a double-walled quartz Dewar mantle which is placed in the center of the cavity. This evacuated Dewar mantle and Peltier elements protect the inner cavity walls against heat-induced modifications. The sample is located in the middle of the cavity and heated with a preheated nitrogen flow. This gas flows past the reactor tube and heats the sample. To heat the nitrogen gas flow, a furnace (tungsten alloy heater) is used.

2.2 Microwave Hall effect technique

In the following, the resonant microwave Hall effect is outlined. The principle of measurement of the direct current and the microwave Hall effect is explained in Chapter 2.2.1 while advantages and disadvantages of the microwave Hall effect technique are summarized in Chapter 2.2.2. Finally, Chapter 2.2.3 describes the in-situ setup developed during this thesis work.

2.2.1 Principle of measurement

Direct current Hall effect

In 1879, Edwin Hall discovered that an additional voltage occurs along the z axis, when a current $\mathbf{I}$ along the x axis (I_x) and a perpendicular magnetic field $\mathbf{B}$ along the y axis (B_y) are applied at the same time[95]. The origin of this effect is a charge carrier drift in the z direction, cf. Figure 2.2.1.

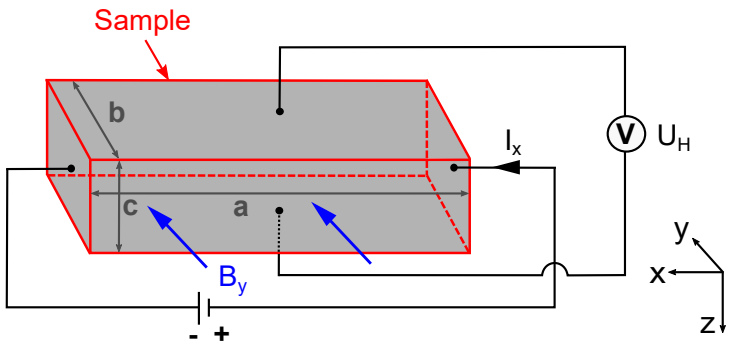

Figure 2.2.1: *Sketch of a direct current Hall effect setup using a rectangular sample, where b is the sample thickness, c its height, and a its length. Further, B_y describes the external magnetic field in y-direction, I_x the current source in x-direction, V the voltage meter, and U_H the Hall voltage.*

This drift in z direction is due to the Lorentz force which pushes the charge carriers perpendicular to both I_x and B_y. The Lorentz force law describes the force $\mathbf{F}_L$ on a charge q moving with a velocity υ in a magnetic field, $\mathbf{F}_L = q(\mathbf{E} + \boldsymbol{\upsilon}\times\mathbf{B})$ [82]. According to this law, the charge carriers are deflected downward and an electric field is created which causes an additional voltage (the Hall voltage U_H) that can be measured. This is expressed by a so-called Hall coefficient R_H defined as

$$R_H = U_H \frac{b}{I_x B_y} \tag{2.9}$$

where b is the sample thickness. Moreover, the sign of R_H depends on the charge carrier type (negative for electrons or positive for electron holes) [96]. Without the external magnetic field, the resistivity ρ of a sample is determined by

$$\rho = \frac{(b\,c)\,U_p}{a\,I_p} = \frac{1}{\sigma} \tag{2.10}$$

where a, b, c, are the length, thickness, and height of the sample (cf. Figure 2.2.1), U_p is the sample voltage, I_p is the (constant) current, and σ is the conductivity. Then, the Hall mobility $\mu_{H,DC}$ is given by

$$\mu_{H,DC} = R_H \sigma \tag{2.11}$$

After introducing the general expression for the mobility, which describes the carrier motion, the following will focus on semiconductors. The reason for this is that the samples

under investigation for this thesis are mainly semiconducting catalysts. Moreover, in semiconducting materials both electrons e and electron holes h contribute to the overall conductivity and mobility. Therefore, the Hall coefficient R_H needs to be defined by a difference

$$R_H = \frac{N_h\ \mu_{H,h}^2 - N_e\ \mu_{H,e}^2}{e(N_h\ \mu_{H,h} + N_e\ \mu_{H,e})^2} \tag{2.12}$$

where N_h and $\mu_{H,h}$ are the charge carrier concentration and Hall mobility of holes, N_e and $\mu_{H,e}$ are the charge carrier concentration and Hall mobility of electrons, and e is the elementary electric charge[96]. This results in a conductivity σ for a semiconducting solid[97]

$$\sigma = |e|\,(N_e\mu_{H,e} + N_h\mu_{H,h}) \tag{2.13}$$

Microwave Hall effect

One option for observing the microwave Hall effect (MHE) is the use of a so-called bimodal MHE cavity. This type of cavity is a key component and has two important characteristics: (i) the existence of two isolated and perpendicularly degenerated modes (bimodal); (ii) the sample position is in the maximum of the electric field. The main geometric MHE cavity forms are cylindrical and rectangular[24]. As introduced in Chapter 2.1.1, the electromagnetic field inside a cavity has a characteristic distribution. Here, the focus is on TE_{mnp} (transverse electric) modes. In particular, following bimodal cavity systems are reported in the literature for example, cylindrical TE_{111}[28,98,99], cylindrical TE_{112}[32,100–102], and rectangular TE_{102}[32] cavities[24]. All these cavities (and the majority of bimodal MHE cavities) operate at X-band frequencies (8 - 12 GHz) which results in an ideal sample to cavity volume ratio. This thesis work concentrates on the cylindrical bimodal TE_{112} cavity which is based on the work of Ong *et al.*[103] and Na *et al.*[104].

The contact-free microwave Hall effect is illustrated in Figure 2.2.2 in a simplified sketch[24]. A bimodal MHE cavity with two perfect orthogonal modes is assumed, c.f. Figure 2.2.2a. The principle of measurement is based on the coupling between these modes of two orthogonal microwaves due to the external magnetic field. The first mode corresponds to the driving field E_x and the second orthogonal mode corresponds to the Hall field E_H, c.f. Figure 2.2.2b, where the charge carriers move in ellipsoid orbits (shown in Figure 2.2.2 as averaged charge carrier motion). Without an external magnetic field energy cannot be transferred between the two decoupled modes. In an external magnetic field (along the z direction) applied perpendicular to the driving field (along the y direction), the charge carriers are deflected by the Lorentz force orthogonally to both the driving mode

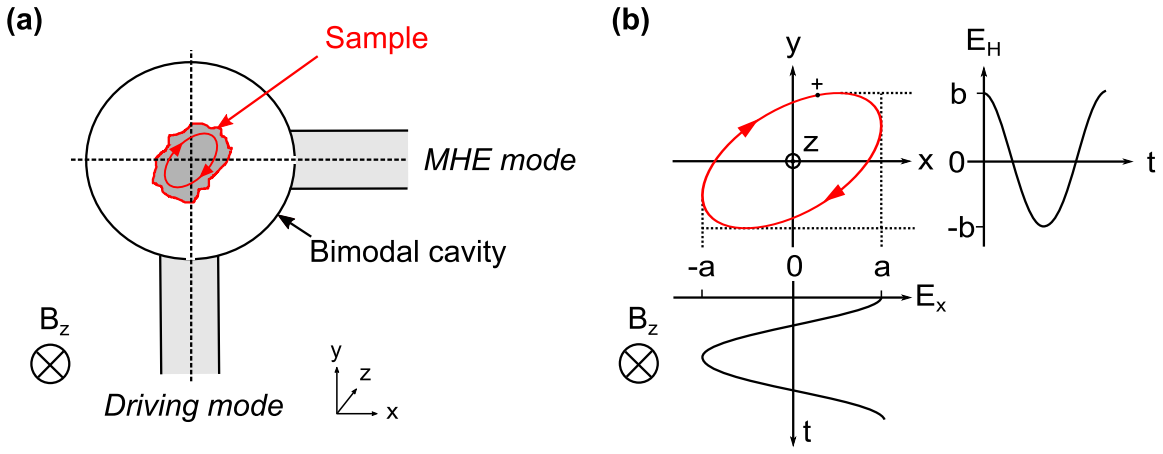

Figure 2.2.2: ***(a)*** *Microwave Hall effect of a sample in a bimodal cavity is presented where the averaged motion of charge carriers is shown applying a static magnetic field perpendicular to the direction of the electric fields of both modes.* ***(b)*** *Detailed sketch of charge carrier motion which is the origin of the Hall power (from E_H) at the secondary mode (according to[24]).*

and the magnetic field. By this effect, energy is transferred from the driving mode into the orthogonal MHE mode (along the x direction) the microwave Hall mobility can be determined from the relationship between the input and output signals.

Usually, a two-port vector network analyzer attached to both ports of the cavity is used to excite one mode of the cavity and detect the microwave response through the other port. The network analyzer measures the scattering matrix assuming ideally matched conditions. This matrix relates the outgoing waves b_1, b_2 to the incoming waves a_1, a_2 (indices denote the ports) according to

$$\begin{bmatrix} b_1 \\ b_2 \end{bmatrix} = \begin{bmatrix} S_{11} & S_{12} \\ S_{21} & S_{22} \end{bmatrix} \begin{bmatrix} a_1 \\ a_2 \end{bmatrix} \tag{2.14}$$

where the matrix elements S_{11}, S_{12}, S_{21}, and S_{22} refer to the scattering parameters (S-parameters). The diagonal elements of the matrix (S_{11}, S_{22}) are the reflection coefficients of port 1 and 2, respectively, while the off-diagonal terms are the transmission coefficients, S_{21} from port 1 to port 2, and S_{12} from port 2 to port 1[24,98,105,106].

Microwave conductivity In general, microwave cavities can accommodate different modes (standing waves) and the accurate determination of their characteristic resonance frequency f and quality factor Q depends strongly on the coupling network between the resonator and the external elements. Different reflection or transmission methods are reported to

define Q[15,107,108]. For the MHE technique the 3 dB method is applied in reflection mode as proposed by Na *et al.*[39]. The S_{11} parameter measures the reflected microwave power vs. frequency spectrum and Q is calculated according to equation 2.8.

Depending on the microwave power absorbed in a sample the resonance properties of the cavity will change. Various theoretical models are proposed for different ranges of conductivity. Here, the focus is on single crystals and powder samples for which the conductivity σ is of intermediate and low range, respectively[32,39]. Furthermore, the so-called quasi-static approximation is assumed to determine the conductivity equations which implies that perturbation of the cavity can be considered small and the oscillating electric fields inside the samples are uniform[24,32]. In the intermediate conductivity region ($0.1 \leq \sigma \leq 100$ S cm^{-1})[32] the conductivity σ is given by

$$\sigma = 4\pi\varepsilon_0 f_l \left(\frac{f_e - f_l}{f_e}\right)^2 \left(\frac{Q_e Q_l}{Q_e - Q_l}\right) \frac{1}{\alpha} \tag{2.15}$$

where the subscrips e and l refer to empty and sample-loaded cavity, α is the apparent filling factor, and ε_0 is the vacuum permittivity. For a cylindrical bimodal TE_{112} cavity α is 2.1 V_S/V_C, where V_S and V_C are the volumes of the sample and cavity, respectively[32]. This apparent filling factor α depends on the cavity geometry (c.f. Appendix C for further details) and is solved numerically. In the low conductivity region ($\sigma < 0.1$ S cm^{-1})[32] σ is given by

$$\sigma = \pi\varepsilon_0 f_l \left(\frac{Q_e - Q_l}{Q_e Q_l}\right) \frac{1}{\alpha} \tag{2.16}$$

Further details of these conductivity equations are given in Appendix C of this thesis.

Microwave Hall mobility To obtain the microwave Hall mobility μ_H critical coupling (i.e., the maximum power is transferred between the resonator and the transmission line[109]) is assumed at both ports. Then, μ_H can be expressed by the incident and transmitted power at the two ports and is determined by[25]

$$\mu_{H,MW} = K\frac{10^4}{B}\left(\frac{Q_e}{Q_e - Q_l}\right)\left(\frac{1}{1-\Gamma^2}\right)\left(\frac{P_H}{P_1}\right)^{1/2} \tag{2.17}$$

where K is the cavity constant, Q_e and Q_l are the quality factors of the primary mode (driving field) of the empty and sample-loaded cavity, B is the external magnetic field, Γ is the reflection coefficient, P_1 is the microwave power of the incident primary mode, and P_H

is the Hall power detected for the secondary mode[25,104]. The factor 10^4 is required if the magnetic flux density B is inserted in Tesla units.

Na *et al.* used a network analyzer to tune and to measure the coupling between the two orthogonal modes for a bimodal cavity[104]. In this case the transmission parameter S_{21} is measured which can be related to the input power at port 1 (P_{i1}) and the output power at port 2 (P_{o2}), respectively, according to [dB] = 10 log(P_{i1}/P_{o2})[104,106]. Hence, equation 2.18 is valid if the bimodal cavity can be considered as a simple two port device[24,98].

$$\left(\frac{P_H}{P_1}\right)^{1/2} = \left(\frac{P_{o2}}{P_{i1}}\right)^{1/2} \rightleftharpoons S_{21} \tag{2.18}$$

Thus, the Hall mobility μ_H can be determined from the change in the scattering parameter S_{21} as a function of magnetic field

$$\mu_{H,MW} = K\frac{10^4}{B}\left(\frac{Q_e}{Q_e - Q_l}\right)S_{21} \tag{2.19}$$

Sayed and Westgate have shown for a bimodal TE_{111} cavity that different input and output coupling can be taken into account by a coupling correction factor and yielded a different equation to determine μ_H[98]. Furthermore, the cavity constant K was introduced to implement cavity imperfections in order to determine absolute Hall mobilities of unknown catalytic samples. Trukhan calculated a K value[25] of 2 based on theoretical considerations assuming $\Gamma = 0$ in equation 2.17. Eley *et al.* calibrated their system with n- and p-type Si and Ge and got a value[27,104] of 2.6 assuming $(1 - \Gamma^2)^{-1}$ = constant for their samples (cf. equation 2.17). Na *et al.* calibrated the cavity constant K with equation 2.19 for a TE_{112} cylindrical cavity using two detection methods: the source modulation method and the network analyzer[104]. Using the source modulation method, the averaged K value was 2.0 ± 0.41 for differently doped n-type (three) and p-type Si (one) samples with well-known charge carrier mobilities. They obtained values of 2.14 and 2.97 for two differently doped n-type Si samples with the network analyzer[104]. Using the same calibration method and the network analyzer, other authors[102] reported values between 2.01 - 2.05. In this thesis the network analyzer was used to calibrate the system. More details about the calibration procedure and the application of the microwave Hall effect in catalysis is given in the result part of this thesis, cf. Chapter 3.3 and Chapter 3.4.

2.2.2 Advantages and disadvantages

Overall, Hall effect measurements are widely applied to measure charge transport properties, i.e., absolute carrier concentration, its type (electron or electron hole), and carrier mobility. Temperature-dependent measurements provide a deeper information on impurities, imperfections, uniformity and scattering mechanisms[110,111]. The significant advantage of the resonant microwave Hall effect method compared with the contact direct current (DC) Hall effect is its high accuracy, the high sensitivity, and the possibility of contact-free measurement. This is crucial for the application to powder samples which are the usual form of industrial catalysts. The preparation of the catalytic sample is easy as a flow-through reactor can be used and the sample is fixed between quartz-wool. Another advantage is the measurement of surface and bulk properties since the microwave penetrates through the sample. These electrical properties, in particular the charge carrier concentration, are given in absolute values after calibration.

One disadvantage is the need to develop a heatable flow-through reactor for high temperatures studies since there is no commercial equipment available. Another problem is the considerable ambiguity with regard to non-ideal mode coupling, imperfections, and residual transmission of the empty cavity system[28,31,112]. This residual transmission comes from non-ideal mode coupling without an external magnetic field which reduces the sensitivity to measure samples with low-mobility[24]. This problem can be solved in parts by introducing a canceling channel where, due to destructive phase overlay, the residual transmission is damped. The Hall effect at the cavity end walls gives an additional increase of the signal caused by external magnetic fields. Thus, all elements need to be free of magnetic components when developing a microwave Hall effect setup.

To the best of my knowledge, an in-situ microwave Hall effect setup has not been developed before.

2.2.3 Experimental setup

The concept of a microwave Hall effect setup using a network analyzer was published by Na *et al.*[39] and is shown in Figure 2.2.3a. According to previous investigations of Ong *et al.*[101], a cylindrical bimodal TE_{112} cavity is used and modified in the present thesis. A flow-through reactor, a gas supply for various reactive gases, and an heating system for high temperature is implemented.

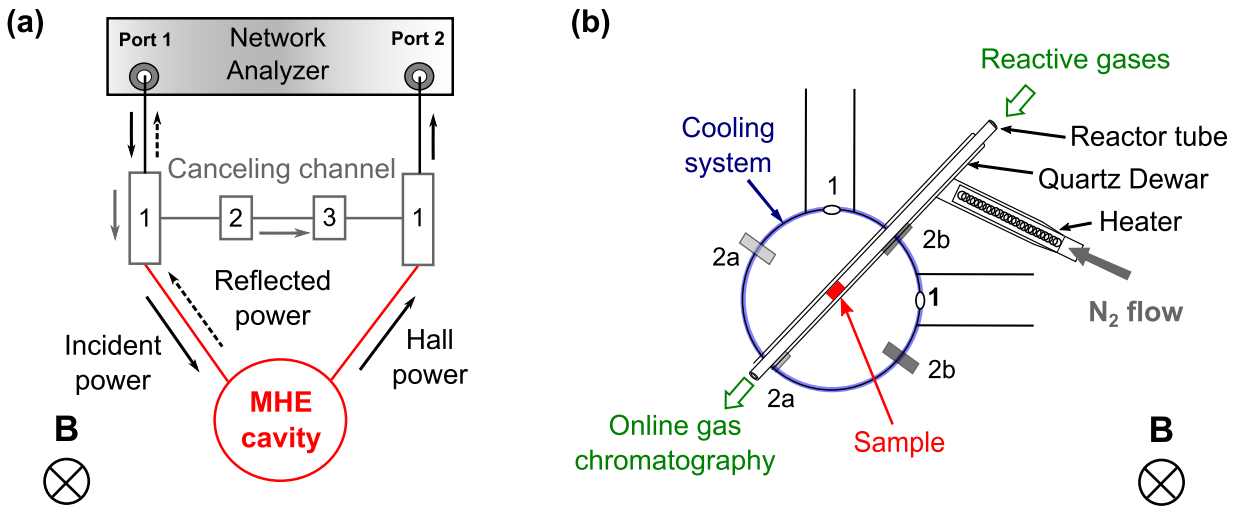

Figure 2.2.3: ***(a)*** *Basic sketch of the microwave Hall effect system, where 1 is the 3 dB directional coupler, 2 the attenuator, and 3 the phase shifter (according to*[24,104]*).* ***(b)*** *A bimodal microwave Hall effect cavity with an implemented flow-through reactor, where 1 is an iris screw, 2a a tuning screw with wood tip, and 2b a tuning screw with metallic tip.*

Figure 2.2.3b illustrates the in-situ cylindrical bimodal TE_{112} cavity which was modified for the studies in heterogeneous catalysis. The cavity tuning, the calibration of the cavity constant K, and the high-temperature verification of the in-situ setup are discussed in the results part, c.f. Chapter 3.3. Here, only a short description of the devloped setup is presented. The in-situ bimodal cavity is connected with the network analyzer via flexible coaxial cables and waveguides. In order to tune the bimodal cavity, four different tuning screws (two with wood tip and two with metallic tip) are needed. These screws are inserted in the lower part of the bimodal cavity (cf. Figure 3.3.2 of Chapter 3.3.3). Imperfections in the cavity geometry and aberrations caused by sample holes are compensated by a tuning procedure. Furthermore, the flow-through reactor in the upper part of the cavity is connected to a gas delivery manifold where various reactive gas feeds can be introduced. To analyze the effluent gas flow, an online micro gas chromatograph is connected of the flow-through reactor. This reactor tube is surrounded by a single walled quartz Dewar mantle. To reach high-temperatures for real catalytic reactions preheated nitrogen flows alongside the reactor tube and heats the sample. The nitrogen is heated by a custom-designed tungsten heater. At the same time, the cavity inner walls are protected against this heat with a water-cooling circuit.

3 Results

3.1 Frequency-, temperature-, and gas-phase-dependent permittivity and conductivity of unpromoted and promoted (Mg, Al, Ga) polycrystalline ZnO

The frequency and temperature-dependent permittivity and conductivity of unpromoted and promoted (Ga, Al, Mg) polycrystalline ZnO have been studied to elucidate the nature of charge carriers and the charge transport mechanism. Permittivity and conductivity studies were performed in the DC, GHz and THz frequency range from room temperature up to more than 200 °C in inert, reducing, and oxidizing gas atmospheres. The measurements show that, the charge transport at room temperature is dominated by bound charge carriers (Lorentz oscillator model) whereas at 230 °C - where ZnO becomes catalytically active, e.g., as part of the $Cu/ZnO/Al_2O_3$ catalyst for methanol synthesis - the conductivity trend suggests the dominating contribution of free charge carriers (Drude model). The type of (free) charge carriers (e.g., electrons) and the influence of the different promoters on the charge transport were analyzed in H_2/O_2 redox cycles at elevated temperatures.

3.1.1 Introduction

A commercially relevant heterogeneously catalyzed hydrogenation reaction of CO_2 is the production of methanol which is an essential intermediate and product in the chemical industry. Methanol is produced over a $Cu/ZnO/Al_2O_3$ catalyst from a $H_2/CO/CO_2$ synthesis gas mixture where Cu is supposed to be the active phase whereas the role of ZnO in the catalytic reaction is still subject of intense investigations [67,113–116].

ZnO is not only important in catalysis research but it has many other industrial applications, e.g., in optoelectronic devices, as white paint pigment or as light emitter [117–119].

Impurity doping of ZnO is associated with the modification of the electrical and chemical (structural) properties,[74,117,120–127] but also modifies its catalytic properties. Deeper insights into the charge transport mechanism and the influence of the dopants can be obtained from frequency-dependent permittivity and conductivity measurements.

The standard model to describe the frequency-dependent transport of free charges is the Drude model. In this approach, the charge carriers are neither damped by a restoring force nor by collision with other electrons[128,129]. H. A. Lorentz advanced this model further and included an electron restoring force. In the underlying model, electrons are bound to the nucleus and assumed to oscillate harmonically. In order to identify the nature of charge carriers based on the aforementioned models, the conductivity/ permittivity has to be measured over a broad range of frequencies. Moreover, to elucidate correlations with catalytic properties the measurements have to be performed at catalytically relevant temperatures or even in reactive atmospheres with polycrystalline materials. So far, only few studies have evaluated the frequency and temperature dependence of the charge transport in polycrystalline samples (powders)[130–132].

In order to identify correlations between the nature of charge carriers, the charge transport mechanism, and the catalytic properties of ZnO, specifically its redox behavior, complex conductivity and permittivity data of polycrystalline ZnO over a broad frequency range were investigated. The analysis at room temperature was complemented by a high temperature measurement at 230 °C, where ZnO becomes catalytically active. Unpromoted ZnO was compared to promoted ZnO samples (trivalent (Al^{3+} and Ga^{3+}) and divalent (Mg^{2+}) dopants, respectively). Since recent studies have shown that Mg doping reduced while Al and Ga doping increased the activity of a Cu/ZnO:M model catalyst in the reverse water-gas shift and methanol synthesis reaction[23]. The conductivity was analyzed in the DC range by a contact technique, in the GHz range by a MCPT with several TM_{0n0} ($n = 1$, 2) cylindrical cavities, and in the THz range by a time-domain THz spectroscopy setup equipped with a high temperature cell. The conductivity and permittivity behavior over this wide frequency range offer unique insights into the nature of the charge carriers at room temperature (23 °C) and elevated temperature (230 °C). Only this combination of techniques gives the opportunity to differentiate between free (Drude model) and bound (Lorentz oscillator model) charge carriers under catalytically relevant conditions which has not been unequivocally demonstrated so far.

3.1.2 Experiment

Samples

ZnO and promoted ZnO:M with 3 mol% doping (M = Al, Ga, and Mg) were prepared by co-precipitation[23,133] (cf. Appendix A for further details). Powder X-ray diffraction (XRD) verified the phase purity, cf. Figure A.1 of Appendix A. The measurements were performed in Bragg-Brentano geometry on a Bruker AXS D8 Advance II theta/theta diffractometer, using Ni filtered Cu Kα radiation and a position sensitive energy dispersive LynxEye silicon strip detector. The Rietveld analysis yielded the size of the coherently diffracting domain of all samples, shown in Table A.1 of Appendix A. Nitrogen adsorption experiments were carried out at -196 °C using a Quantachrome Autosorb-1 analyzer. Prior to the measurement, the samples were degassed in vacuum at 70 °C for 2 h. The specific surface area was calculated according to the multipoint Brunauer-Emmett-Teller method (cf. Table A.1 of Appendix A). High resolution Transmission Electron Microscopy (TEM) images were taken on a JEOL JEM-ARM200F Microscope. Figure A.2 of Appendix A summarizes the high resolution TEM images of all ZnO:M samples.

High temperature DC conductivity technique

The high temperature DC conductivity measurements were performed in a teflon cell using a gas sensor chip (Al_2O_3 substrate with interdigitated Pt electrodes). Figure 3.1.1a shows the experimental setup[134]. The electrical resistance R_{meas} was measured and calculated into the electrical resistivity ρ according to, $\rho = (R_{meas}bc)/a$ where a is the layer length (6 mm), b is the layer width (2.2 mm), and c is the layer thickness (3 mm). Here, the assumption of an ideal, rectangular shaped layer is made (cf. Figure 2.2.1)[135]. The electrical conductivity σ_{DC} is shown which is the inverse of the electrical resistivity values ($\sigma = 1/\rho$).

The catalyst (15 mg) was suspended in 80 μl deionized water. The suspension was added dropwise onto the measurement chip and the solvent was evaporated in an external oven (80 °C). The coated chip was then placed inside the reaction cell. The temperature was increased to 230 °C in nitrogen and kept there for 10 min. A reducing feed (95 vol% N_2, 5 vol% H_2) was applied for 10 min, inert gas (100 vol% N_2) for 60 min, followed by the oxidizing gas feed (95 vol% N_2, 5 vol% O_2) for 10 min, and inert atmosphere (100 vol% N_2) for 55 min. The total gas flow was 40 ml/min.

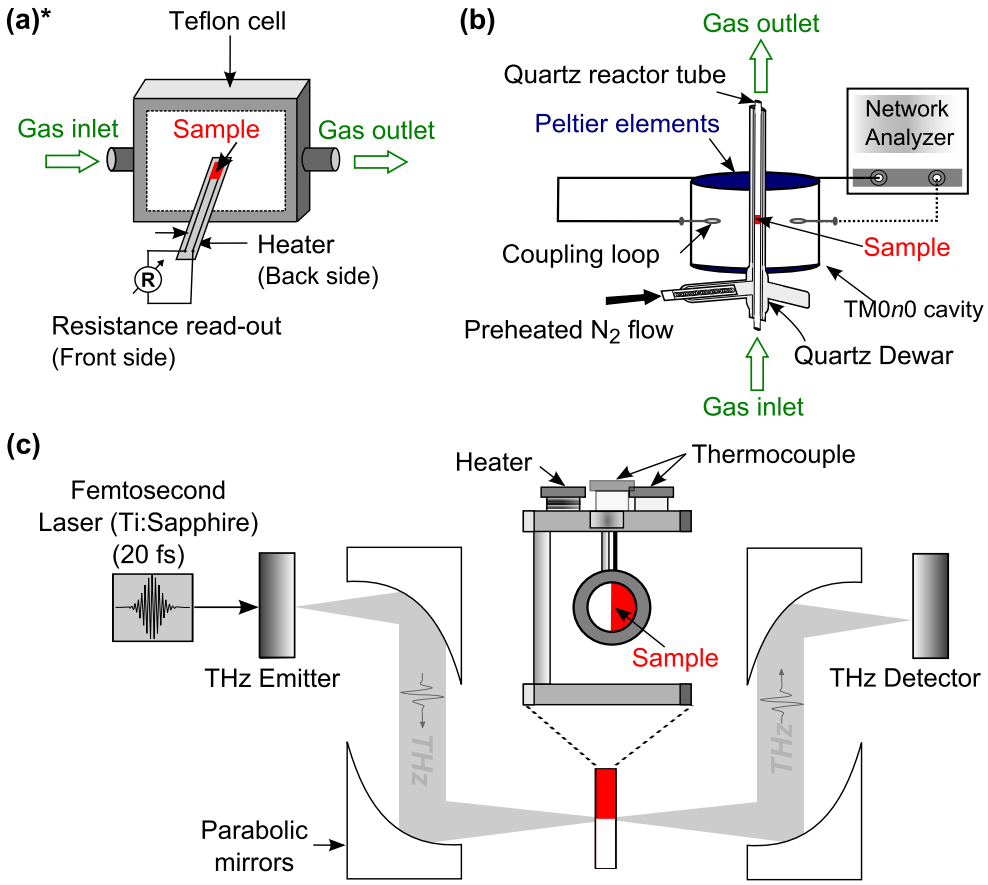

Figure 3.1.1: *Sketch of* ***(a)**** *The DC conductivity setup (*modified from Sänze et al.*[134]*), and* ***(b)*** *The high temperature MCPT setup, and* ***(c)*** *The high temperature THz spectroscopy setup.*

High temperature microwave cavity perturbation technique

The high temperature MCPT setup has been used to measure the microwave conductivity. A microwave cavity is a special type of resonator consisting of a closed metal structure that confines electromagnetic fields in the microwave region of the spectrum. The boundary conditions at the cavity walls force the fields to exist only at certain quantized resonant frequencies. The energy carried by the wave must be conserved forcing the cavity to store this energy in standing waves which oscillate with nodes at the boundaries of the cavity, where the electric field is zero. When a powder sample in a fix-bed flow-through reactor is introduced inside the cavity, the electric and magnetic field changes due to its dielectric properties. This small interaction between microwave and sample leads to a shift in resonance frequency f and a changed line shape at full width at half maximum of the resonance frequency Δf in the cavity. The quality factor is defined as $Q = f/\Delta f$.

The changes of f and Q due to the introduction of the catalyst relates to the complex permittivity ($\varepsilon = \varepsilon_1 + i\varepsilon_2$)[15,16,18,20,24,83,89] according to equation 2.5 and 2.6. Finally, the microwave conductivity is obtained from equation 2.7 as described in Chapter 2.1.1.

In the present study, the experiments were performed in a cylindrical silver- and gold-plated TM_{0n0} (n = 1, 2) cavity. In addition, the first (TM_{010}) and second mode (TM_{020}) of this cavity were investigated. Figure 3.1.1b illustrates the experimental setup which was introduced earlier (cf. Chapter 2.1.3). Different cavities were designed with a frequency range between 1 and 17 GHz (cf. Table A.2 of Appendix A). To analyze the redox behavior of the ZnO:M sample, the first mode TM_{010} (5 GHz) of the C-band cavity was used. The cavity was connected via a semi-rigid coaxial cable (PE3492LF, Pasternack Enterprises) with a microwave source and a detection unit (Vector network analyzer, Agilent PNA-L N5230C-225). The coaxial cables had specific coupling loops at their ends which were used to inductively couple the microwaves into the cavity. The position of the powder sample in a quartz tube reactor was in the middle of the cavity which means at the electric field maximum (cf. Figure 2.1.2b of Chapter 2.1.3)[83]. The quartz tube reactor was filled with powder sample (100 - 200 μm sieve fraction) to a bed length of 5 mm (corresponding to 30 mg). The sample was heated up in a preheated nitrogen flow using an air heater (Sylvania Tungsten Heater Series III) to 230 °C with 10 °C/min while the temperature of the cavity was kept at 20 °C (Peltier elements). Mass flow controllers (Bronkhorst EL-Flow) regulated various gases. The redox response of all samples was investigated by sequentially applying inert/reducing/inert/oxidizing/inert gas feeds. A reducing feed (95 vol% N_2, 5 vol% H_2) was applied for 30 min; inert atmosphere (100 vol% N_2) for 60 min followed by the oxidizing atmosphere (95 vol% N_2, 5 vol% O_2) for 30 min and an inert atmosphere (100 vol% N_2) for 55 min. The total gas flow was set at 5 ml/min.

High temperature terahertz time-domain spectroscopy

Broadband Terahertz time-domain spectroscopy (THz-TDS) was employed to obtain direct access to the carrier dynamics[128]. The phase-sensitive time domain detection of the THz-pulse transmitted through the sample and a reference (N_2) provide direct insight into the conductivity mechanism. Therefore, the complex conductivity from 0.5 to 2.5 THz[136] is measured with an electromagnetic THz transient that interacts with the material. A detailed explanation of the evaluation procedure can be found in Appendix A. Here, a standard THz-TDS configuration[136] was used with laser pulses from a Ti:sapphire oscillator (pulse duration: 20 fs, center wavelength: 800 nm, repetition rate: 80 MHz, pulse energy:

1 nJ) which generate THz pulses by difference frequency mixing in a 1 mm thick ZnTe (110) crystal. A sketch of the setup is shown in Figure 3.1.1c. All experiments were performed in dry nitrogen atmosphere to avoid absorption of water from air. The THz electric field is transmitted through the sample which leads to an attenuation and phase delay of the field and is detected by electro-optic sampling in a 0.5 mm thick ZnTe (110) crystal[137]. The sample temperature is modified and controlled in an in-situ cell sample holder[138].

All samples were pressed with pressure of 3 tons resulting in a powder pellet with a diameter of 13 mm and a thickness of 0.1 mm. Various sample spots were measured to ensure the homogeneity of the samples. The measurements were performed at 23 °C, 230 °C, and 330 °C.

3.1.3 Results and discussion

Validation of complex permittivity measurements over a broad spectral frequency range

To confirm the consistence of the results obtained with different techniques in the MHz, GHz and THz range, test measurements on a ZnO:Ga sample were performed. For a direct comparison of results from the MCPT with those of THz spectroscopy all complex powder permittivity values ε_p for the ZnO:Ga sample were converted to complex bulk permittivity values ε_s using effective medium theory. Specifically, the Landau-Liftshitz-Looyenga formalism was used for the transformation[93,94].

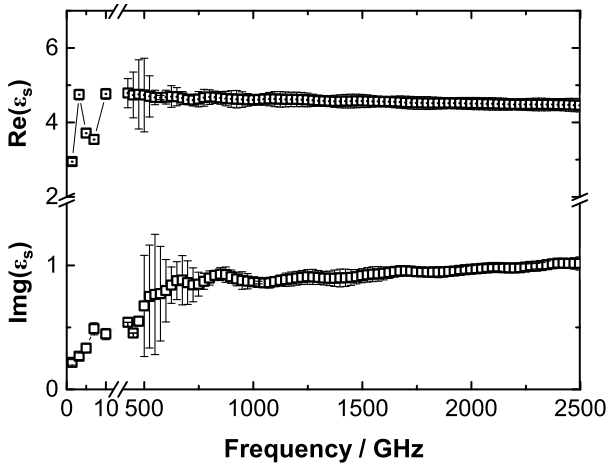

Figure 3.1.2: *Complex bulk permittivity ε_s measurements of polycrystalline ZnO:Ga (GHz - THz) at 23 °C.*

The real part of the permittivity ($\varepsilon_{1,s} = \mathrm{Re}(\varepsilon_s)$) increases in the GHz range and stays constant in the THz range (cf. Figure 3.1.2). The imaginary part of the permittivity ($\varepsilon_{2,s} = \mathrm{Img}(\varepsilon_s)$) shows a characteristic increase for both the GHz and THz range. The stepless continuation from 10 to 500 GHz within the same order of magnitude shows the reliable measurement of the permittivity over a broad spectral range (1 to 2500 GHz).

Multi-frequency and temperature-dependent permittivity in the GHz to THz frequency range

To gain a more detailed insight into the nature of charge carriers, the resonance frequency and the reaction temperature were varied. In actual measurements the focus is on the comparison between complex powder permittivity values of all polycrystalline ZnO:M samples (M = Al, Ga, and Mg) since both methods have direct access to the real and imaginary part without using the Kramers-Kronig relationship. The obtained complex permittivity ε_p is related to the complex conductivity σ_p [20,103] by

$$\sigma_p = \sigma_{1,p} + i\sigma_{2,p} = \varepsilon_0\omega(\varepsilon_{2,p} + i\varepsilon_{1,p}) \tag{3.1}$$

where σ and ε are frequency-dependent ($\sigma(\omega)$ and $\varepsilon(\omega)$).

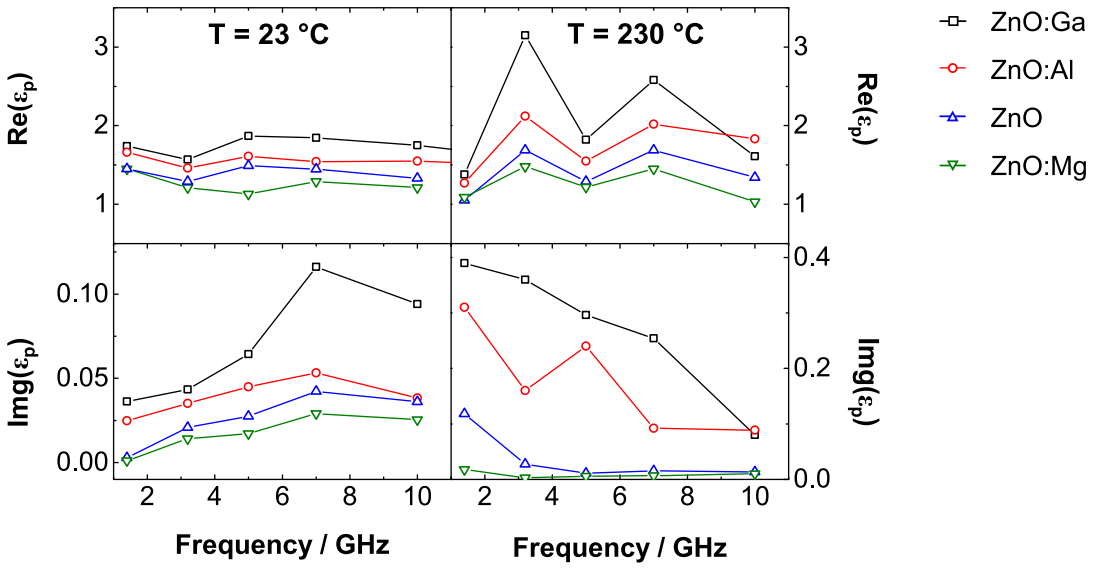

Figure 3.1.3: *Multi-frequency complex powder permittivity ε_p measurements of polycrystalline ZnO:M (M = Al, Ga, and Mg) using MCPT at 23 °C and 230 °C in inert atmosphere.*

The results for all ZnO:M samples at room temperature (23 °C) and elevated temperature (230 °C) using multi-frequency permittivity measurements are depicted in Figure 3.1.3. At 23 °C, the real part of the permittivity ($\varepsilon_{1,p} = \mathrm{Re}(\varepsilon_p)$) yielded almost constant values whereas the imaginary part ($\varepsilon_{2,p} = \mathrm{Img}(\varepsilon_p)$) increased slightly with increasing frequency. After heating to 230 °C no definite changes were observed for the real part, but the imaginary part decreased with increasing frequency. The conductivity differences between the differently promoted samples will be discussed in detail when describing the response in different atmospheres.

In the next step, the ZnO:Ga sample was analyzed in an extended GHz and THz range using THz spectroscopy. The results are shown in Figure 3.1.4. This sample was chosen since it showed the largest frequency-dependent changes in the microwave permittivity measurements. The real part of the permittivity yielded rather constant values as it was observed above for the MCPT. At 23 °C, the imaginary part increased up to about 900 GHz and remained almost constant at higher frequencies. At 230 °C, and even more pronounced at 330 °C, the trend was reversed. Here, the conductivity showed a monotonic decrease with increasing frequency up to about 700 GHz.

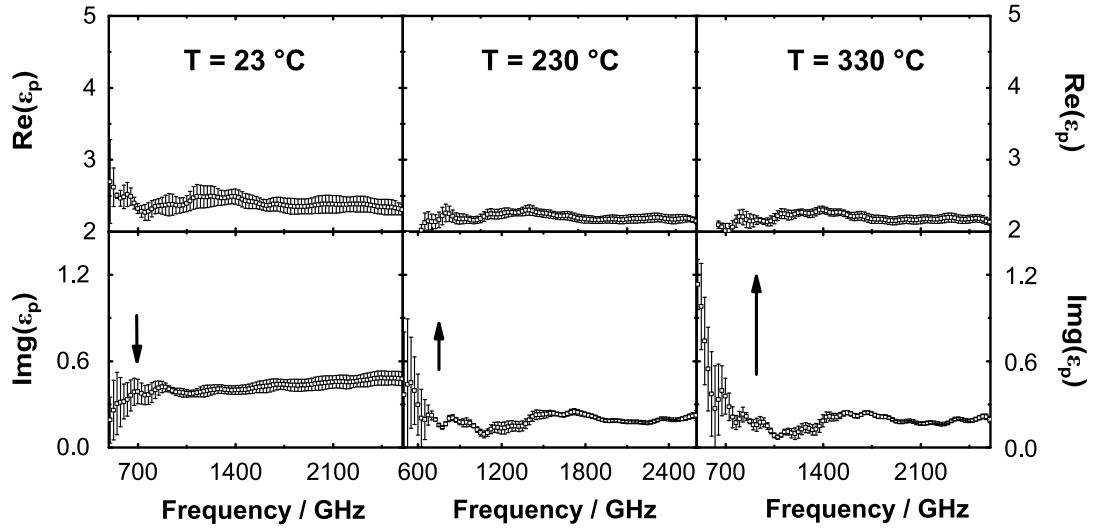

Figure 3.1.4: *Multi-frequency complex powder permittivity ε_p measurements of polycrystalline ZnO:Ga using THz spectroscopy at 23 °C, 230 °C and 330 °C in inert atmosphere.*

High temperature and gas-phase-dependent DC and microwave conductivity

In Figure 3.1.5a, the DC electrical conductivity response and in Figure 3.1.5b, the contact-free microwave conductivity response are shown in effective powder values. Overall, the

reported data reveal a lower conductivity values for the DC method compared to the microwave method.

It is known from literature that unpromoted ZnO has an n-type semiconducting behavior due to intrinsic defects such as oxygen vacancies and interstitial zinc atoms[117]. In comparison with the unpromoted ZnO samples the trivalent dopants Al^{3+} and Ga^{3+} enhanced both the microwave conductivity, and DC conductivity. A difference between both methods was observed for the divalent dopant Mg^{2+} which lowered the microwave conductivity and enhanced the DC conductivity compared with pure ZnO.

In reducing gas feed (N_2/H_2) all ZnO:M samples showed an increase in microwave/DC conductivity, and when applying an oxidizing gas feed (N_2/O_2), the microwave/DC conductivity decreased. Different absolute conductivity changes were found corresponding to the different gas compositions. While the reducing gas feed showed a large increase, the absolute changes in oxidizing gas feed were smaller. Possible explanations for these findings could be the pronounced gas sensing properties of ZnO for hydrogen described in literature[117,139]. However, these methods take a different view at the equilibrating process in inert gas feed after reducing or oxidizing gas feed. The observed changes in conductivity are almost reversible for both methods which can be seen when going back to measurements at inert atmosphere. The slightly lower value in the second and third inert feed might be due to structural change/damage, residual gas molecules, or a longer relaxation of the ZnO:M samples.

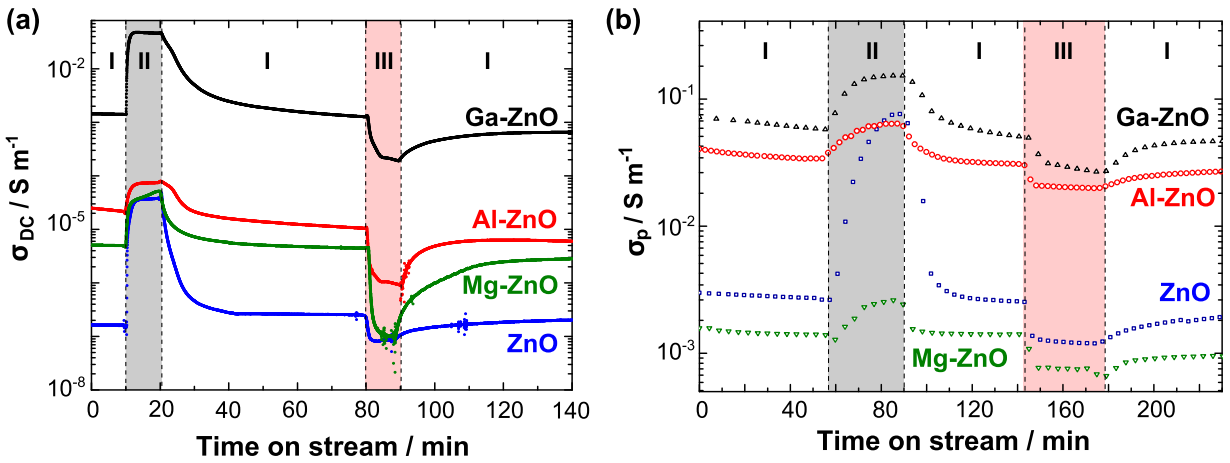

Figure 3.1.5: ***(a)*** *DC conductivity changes and* ***(b)*** *Microwave conductivity changes in different reactive atmospheres at 230 °C. Here, the gas composition was as follows: I 100 vol% N_2 (highlighted in white), II 5 vol% H_2/ 95 vol% N_2 (highlighted in gray), and III 5 vol% O_2/ 95 vol% N_2 (highlighted in red).*

Frequency and temperature dependence of the complex permittivity

To the best of my knowledge, such a broadband investigation (DC-GHz-THz) of the permittivity and conductivity of polycrystalline ZnO samples at room and high temperature is observed for the first time. The reported data reveal a strongly temperature-dependent charge transport mechanism. Two classical microscopic models were used to describe the relation between the frequency dependence of the permittivity and the microscopic properties of the sample. The complex permittivity at 23 °C was fitted with a Lorentz-Oscillator function which is usually associated with bound charge carriers (cf. Figure A.3 of Appendix A). At 230 °C, the trend in the complex permittivity reversed in particular, for $\mathrm{Img}(\varepsilon) = \varepsilon_2$. The overall conductivity increased with increasing temperature and the $\mathrm{Img}(\varepsilon)$ decreased with increasing frequency. This behavior can be described by the Drude model and is usually associated with free charge carriers. In conclusion, while at room temperature the conductivity and permittivity was dominated by bound charges at high temperature a strong contribution of free charges to the overall conductivity response was observed.

The influence of promoters on the conductivity of polycrystalline ZnO

The influence of the different dopants in ZnO was studied by measuring a conventional DC conductivity and by applying the newly developed MCPT method. As a result, an increase in conductivity with trivalent dopants (Al^{3+} and Ga^{3+}) was observed for both methods which is consistent with literature[23,117,119,140]. The concentration of defects is increased due to the fact that Al and Ga form shallow donor states in the band gap of ZnO. Further, it is known from the literature that Al^{3+} prefers tetrahedral sites and Ga^{3+} prefers octahedral sites[120,140]. The effective ionic radii of the impurities are different[141] which means that the interaction between donor and acceptor defects is different and causes a change in electrical properties.

Only the absolute conductivity of ZnO:Mg disagreed between DC conductivity and microwave conductivity measurements. A higher value in the DC conductivity and a lower value in the microwave conductivity measurements compared with the undoped ZnO was found. It is reported, that divalent substitution compensates the intrinsic impurity level in ZnO via the reduction of donor states or the formation of deep level traps[119] which means that a lower conductivity for ZnO:Mg compared with ZnO should be expected. Additionally, less oxygen vacancies (double ionized $V_O^{\cdot\cdot}$ or single ionized $V_O^{\cdot}$) might give an explanation.

In Kröger-Vink notation, the decrease in $V_O^{\cdot\cdot}$ or $V_O^{\cdot}$ is accompanied by less mobile electrons e' which is related to a lower conductivity, c.f. equation 3.2.

$$V_O^x \rightleftharpoons V_O^{\cdot} + e' \rightleftharpoons V_O^{\cdot\cdot} + 2e' \tag{3.2}$$

Obviously, the MCPT measurements show the expected behavior of the divalent promoter Mg^{2+} in ZnO. These fixed-bed reactor experiments avoid effects of contact resistance or of powder-electrode stability[15]. The difficulties are usually associated with contact measurements of thin films or polycrystalline samples. Therefore, a comparison between the differently promoted ZnO samples and their absolute values is challenging and might explain the deviation in the experiments.

A redox cycle was performed to investigate the changes in the electronic structure under reducing and oxidizing reactive atmospheres. The gas-phase-dependent changes obtained from high temperature DC conductivity and microwave conductivity measurements are consistent with each other. The conductivity increased in N_2/H_2 due to electron injections. Hence, hydrogen is fully ionized and forms hydroxide defects which equilibrate to water vapor or shallow donor states (O-H bonding unit)[122,142–145]. Apparently, due to the high concentration of charge carriers in ZnO:Al and ZnO:Ga the effect of hydrogen doping is less pronounced compared with the unpromoted catalyst. Furthermore, hydrogen can diffuse into the ZnO and occupy interstitial sites[146]. In a model density functional theory study, it is proposed the charge transfer occurs at the sites and corners of ZnO where oxygen gains electrons from the hydrogen (assuming a ZnO-H bond)[147]. Assuming hydrogen adsorption at the surface the additional electrons lead to metallization of the ZnO surface[148,149] which may be another explanation of the increased conductivity since metallic ZnO is more conductive than semiconducting ZnO. Figure 3.1.5 shows a decreasing conductivity with oxidizing feed (N_2/O_2). This effect results from the extraction of conduction band electrons and formation of O^{2-}, O_2^-, O^- (or O_O^x in Kröger-Vink notation) species at 230 °C[40] according to

$$O_{2,gas} + 2V_O^{\cdot} + 2e' \rightleftharpoons 2O_O^x \tag{3.3}$$

Khranovskyy *et al.*[150] reported for nanostructured ZnO films that oxygen diffuses into the bulk and fewer oxygen vacancies are formed resulting in a lower conductivity. Here, different impurities (Al, Ga, and Mg) affect the oxygen diffusion coefficient[151] which leads to a different response of the ZnO:M samples in oxygen gas atmosphere.

When going back to inert atmosphere (cf. Figure 3.1.5 gas feed I 100 vol% N_2) an equilibrating process for all samples was observed. The results indicate that the equilibrating behavior for high temperature DC conductivity is faster compared with high temperature microwave conductivity measurements. This observation is related to the different sample regions probed in the experiments which can be also seen in the absolute microwave/DC conductivity values. At this point it is important to mention that the transformation to absolute DC conductivity values is not straightforward, i.e., polycrystalline material, sample preparation, layer inhomogeneity, Schottky barriers at electrode-sample interfaces. However, the DC conductivity measurements yielded order of magnitudes lower values compared to the MCPT. Therefore, it is presumed that the surface of the catalyst is more probed and a different charge transport mechanism takes place which, in addition, includes electrical and chemical electrode effects[135]. In literature, it was speculated that for contact-free MCPT measurements both surface and bulk contribute to the signal[15,18] where bulk diffusion is associated with slower diffusion constants and, hence, longer relaxation times. Such a behavior (AC conductivity > DC conductivity) was reported for crystalline silicon and explained by polarization caused by hopping processes[152] which is in agreement with other research publications[153,154].

In summary, Al^{3+} and Ga^{3+} dopants enhance the conductivity and Mg^{2+} dopant lowers the conductivity compared with unpromoted ZnO. The same electrical response in reducing (increasing conductivity) and oxidizing (decreasing conductivity) gas atmospheres is observed for all samples. Both high temperature techniques (contact and contact-free) are in line with changes in the electronic structure of all ZnO:M samples as well as changes in different gas atmospheres which is in close agreement with a large body of literature. As a result of this study, the MCPT with a TM_{0n0} cavity is better suited for measuring polycrystalline samples under catalytic relevant conditions. This refers to the detection of effects of doping and charge carrier mobility/ charge carrier concentration rather than on overall current transport (DC conductivity). The advantage of directly using powder samples in flow-through fixed bed reactors for MCPT measurements is ideally suited for catalytic measurements. Another advantage is the analysis of the effluent gas flow using an online gas chromatography (cf. Figure 2.1.2). Compared to the contact technique, the absence of grain boundaries, intergrain regions, etc. and electrode contacts increases the sensitivity towards absolute values for powder samples in MCPT measurements. Additional advantages and also disadvantages are summarized in Chapter 2.1.2.

The activity in methanol synthesis is high for Al and Ga promoted Cu/ZnO catalyst compared with Mg promoted and pure Cu/ZnO model catalysts [23]. All investigated samples show a clear change in complex permittivity as a function of frequency and temperature. This effect is most pronounced in ZnO:Ga which indicates the highest density of free charge carriers among all samples. For future work, this increase in charge carrier density can be verified by in-situ microwave Hall effect measurements (cf. Chapter 3.3). Since the observed conductivity order of ZnO:Mg < ZnO < ZnO:Al < ZnO:Ga perfectly reflects the activity trend of a Cu/ZnO:M model catalyst for reverse water-gas shift and methanol synthesis reaction. The catalytic performance could be related to the concentration of free charge carriers and, hence, an alleviated charge transfer in the hydrogenation reaction. This is further investigated in Chapter 3.4 where an in-situ charge carrier analysis is reported for Cu/ZnO based catalysts.

3.1.4 Conclusions

Multi-frequency permittivity and conductivity measurements revealed that the charge transport mechanism and the nature of charge carriers change from room to high temperature in unpromoted and promoted polycrystalline ZnO. While at room temperature the conductivity is dominated by bound charge carriers a significant contribution of free charge carriers to the signal is observed at higher temperature. Moreover, intentionally introduced impurities into the ZnO wurtzite structure change the electrical behavior. It was found that these promoting agents increase (Al, Ga) or decrease (Mg) the initial intrinsic n-type conductivity of ZnO. In addition, the change in electrical properties in reducing and oxidizing feed proves that electrons are the major (free) charge carriers under reaction conditions. Recent studies showed that Mg doping reduces while Al and Ga doping increase the activity of a Cu/ZnO model catalyst in the reverse water-gas shift reaction and methanol synthesis. Thus, a direct causal relationship between the free charge carriers, modified by the promoters, and catalytic performance can be expected. This is related to the mechanistic need in CO_2 chemistry to activate the molecule by adding an electron to it that results in bending of the linear molecular geometry which is pre-requisite for breaking the stable bonds between carbon and oxygen.

3.2 Influence of steam on a vanadyl pyrophosphate catalyst during propane oxidation

The (surface) electronic and catalytic modifications of the p-type semiconducting selective oxidation catalyst vanadyl pyrophosphate have been investigated for propane oxidation in the presence and absence of steam. Steam is found to increase the selectivity towards the oxygenates acrylic acid, acetic acid and the olefin propylene. A reduction in selectivity of the undesired total oxidation products CO and CO_2 was observed together with a decreasing propane conversion. Contact-free in-situ microwave conductivity measurements at 1 bar revealed that the modified catalytic performance is accompanied with a reduced electrical conductivity. Surface sensitive Near-Ambient-Pressure X-ray Photoelectron/ Absorption spectroscopy measurements at 0.25 mbar showed that steam depletes the topmost surface of VPP in phosphorus and enhances the average vanadium oxidation state slightly. These findings are accompanied by a decreased work function, but no detectable shift of the valence band edge is observed. Thus, the chemical surface modification changes the surface dipole but leaves the barrier height of the surface induced space charge layer basically unaffected. It is concluded that steam does not affect the electron hole concentration (majority charge carriers) and, hence, the oxygen vacancy concentration. The reduced conductivity can be understood in terms of charge carrier mobility changes which may affect the selectivity of VPP towards the oxygenates with steam.

3.2.1 Introduction

Upcoming raw material changes in the chemical industry call for innovations in heterogeneous catalysis technologies[46,155]. Oxidative dehydrogenation and selective oxidation of short-chain alkanes (e.g., ethane, propane, and butane) are desirable reactions that often suffer from low selectivity. A trendsetter in the direct alkane oxidation is the VPP catalyst[17,18]. VPP is used in the maleic anhydride synthesis from n-butane oxidation on an industrial scale with a yield of 65 mol%[17,51–53]. This oxidation reaction has been among the most studied topics in oxidation catalysis in recent decades. In contrast, VPP is found to be also active in propane oxidation but less selective[156]. Even though propane is in the same class of homologous compounds (less CH_2) as butane, it is still not clear why VPP could not be used as a catalyst in the acrylic acid synthesis from propane oxidation (cf.

Chapter 1.2). Direct synthesis of acrylic acid from propane can be achieved with the $MoVTeNbO_x$ (M1-phase) catalyst[157–160] at moderate temperatures of 400 °C[59,159,161,162]. However, this mixed metal oxide catalyst is still not efficient enough (acrylic acid yield of 48 %[161,163]) to compete with the industrial two step catalytic process (acrylic acid yield of 98 %)[48,164].

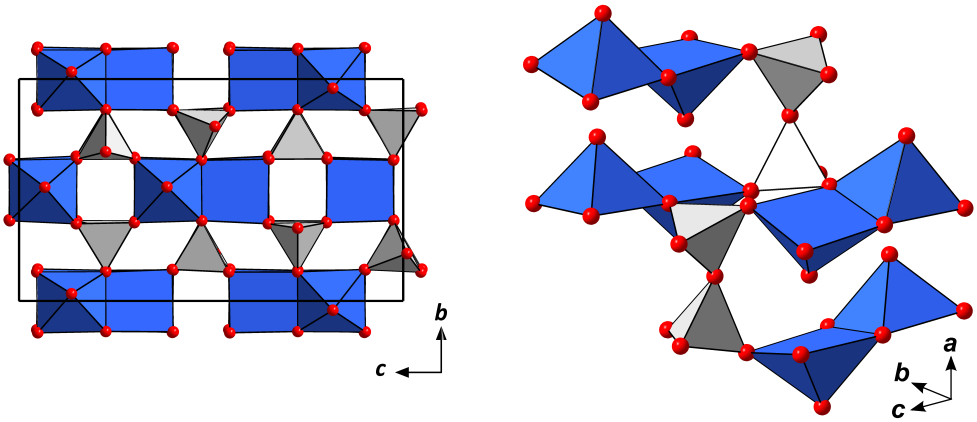

Figure 3.2.1: *Schematic illustration of the VPP structure with oxygen atoms in red, [VO_6] octahedrons (or [$O_4V{=}O$] square pyramids) in blue and [PO_4] tetrahedrons in grey.*

Oxidation catalysts were developed applying empirical strategies guided by phenomenological concepts[6,58]. These strategies do not give insight about the catalyst's state of operation on an atomic scale. Several studies emphasize that the (surface) electronic structure plays an important role to understand the catalyst working mode[6,47,58,165]. For instance, insights into the electronic structure can be achieved by measuring the electrical conductivity. Recent developments of the in-situ MCPT allow conductivity measurements of powder catalysts in a realistic fix-bed reactor geometry[15,20]. Here, $MoVTeNbO_x$ (M1-phase) and VPP revealed a gas-phase-dependent conductivity response at reaction temperatures like oxide gas sensors[17,18,21,22]. To achieve such conductivity response, charge carriers are exchanged between the gas phase reactants and the active oxidation catalyst[17]. Obviously, the exchange of charge carriers takes place at the surface of the catalyst. The role of the charge carrier type, however, remains unclear, since VPP is a p-type semiconductor with electron holes as major charge carriers[13,18,166] while $MoVTeNbO_x$ (M1-phase) is a n-type semiconductor with electrons as major charge carriers[21,22]. Therefore, a closer look at the surface electronic structure should provide deeper insight into the exchange processes. Near-Ambient-Pressure X-ray Photoelectron (NAP-XPS), and Absorption Spectroscopy

(XAS, measured in total electron yield) are highly surface sensitive methods to further investigate the charge carrier dynamics during the catalytic reaction[22].

Figure 3.2.1 shows the crystal structure of VPP which consists of distorted [VO_6] octahedra sharing edges which are joined by edges. A pair of [VO_6] octahedra is equatorial linked to [PO_4] tetrahedra forming a layered structure in the (100) plane[49]. The oxygen polyhedron of vanadium is often considered as a [VO_5] square pyramid with a short apical V=O bond (1.6 Å). The V=O bonds are in *trans* position and the layers are connected by pyrophosphate groups (P_2O_7)[49,167,168].

Vanadium has the oxidation state +4 in the bulk. At the surface it is higher and fluctuates between 4.0 and 4.3 depending on the applied gas phase[18,19,169]. This discrepancy has given rise to fierce discussions in the literature. The contribution of surface species V^{5+} increases the averaged oxidation state and represents a defect in terms of the ideal bulk geometric and electronic structure. The remarkable amount of V^{5+} defect states indicates that the surface termination layer differs from the VPP bulk. Furthermore, the surface V^{4+}/V^{5+} redox couple changed with varying concentration of the reaction feed and correlated well with the energy position of the XP valence band onset and secondary electron cutoff[18]. These changes were interpreted as variation in the surface induced band bending and electron affinity[47]. The band bending is associated with a large space charge layer in which the majority charge carries are accumulated or depleted. Thus, band bending variation can explain the observed conductivity changes induced by the catalytic reaction. The control of the electron supply to the catalysts surface was discussed in terms of oxygen activation[58,170–173]. Following this hypothesis, the catalytic reaction would be self-regulated by the potential barrier of the space charge layer. As pointed out in the literature these physical descriptors might be a promising attempt to understand the selectivity of oxidation catalysts[47].

$MoVTeNbO_x$ (M1-phase) studies provided another interesting phenomenon. The selectivity to acrylic acid is triggered by steam in the reactive propane feed which is accompanied by modifications of the electronic structure decreasing the conductivity due to the added steam[22,59,174]. This observation was further investigated by NAP-XPS/XAS studies. Interestingly, the V^{4+} concentration and the binding energy position of the valence band onset remain unaffected during the steam induced surface modification of the elemental composition, i. e. enrichment of V, Te, and depletion of Mo[22]. It turns out that the V^{5+} concentration increases with steam addition[22,59]. Therefore, a modification of the surface

induced band bending can be excluded to explain the decreased conductivity with steam. Instead, a change of the charge carrier mobility may occur[22].

The aim of this work was to investigate the effect of steam on the electronic structure of VPP during propane oxidation. Since H_2O is omnipresent as a by-product in alkane oxidation reactions, this study is of fundamental interest and can give detailed information about the steam induced modifications at a selective oxidation catalyst. The steam induced changes in electronic structure were monitored by in-situ microwave conductivity measurements in a contact-free manner at ambient pressure. Surface modifications were further analyzed by NAP-XPS and NEXAFS in the total electron yield mode at 0.25 mbar. The core level spectra of the $V2p_{3/2}$ and $P2p_{3/2}$ as well the NEXAFS L_3-edge were also measured to determine the surface elemental composition, the vanadium oxidation state, and the P/V ratio. These findings were completed with valence band and secondary electron cutoff measurements to investigate a change of the energy band alignment induced by steam.

3.2.2 Experiment

Sample

The VPP catalyst was prepared via an alcohol route and activated[18]. Phase purity of the $(V^{IV}O)_2P_2O_7$ catalyst (FHI ID.: 10449) was proven by powder XRD, cf. Figure B.1 of Appendix B[17,18].

In-situ microwave cavity perturbation technique

Electrical conductivity measurements were conducted to monitor the influence of steam on the charge transport properties of VPP. This electrical conductivity analysis was performed in a contact-free manner using the MCPT[15,16,20]. The MCPT was introduced in Chapter 2.1.1. In brief, the measurement principle is based on the fact that the electric and magnetic field distribution inside a microwave cavity is modified by a dielectric sample. The electromagnetic field inside the cavity is at resonance with a characteristic resonance frequency f and a quality factor Q. The introduction of the dielectric catalyst in the maximum of the electromagnetic field shifts f and decreases Q. This dielectric response is described by the complex permittivity ($\varepsilon = \varepsilon_1 + i\varepsilon_2$)[16,18]. The real and imaginary part of the complex permittivity can be computed according to equation 2.5 and 2.6. The obtained effective values for the polycrystalline catalyst are transformed to

effective bulk values applying the Landau-Liftshitz-Looyenga formalism (cf. equation 4.3 of Appendix A)[93,94]. Finally, the electrical microwave conductivity σ is obtained from equation 2.7 of Chapter 2.1.1.

For the in-situ microwave conductivity measurements, a custom-designed cylindrical microwave cavity (height of 20 mm and an inner diameter of 45 mm) was used. The experiment was performed with the first transverse magnetic mode (TM_{010}) at an empty resonance frequency of about 4.79 GHz. A network analyzer was used to generate microwaves (Agilent PNA-L N5230C) and was connected via a coaxial cable with the cavity. Here, a coupling loop inductively coupled the microwave into the cavity. For the catalytic studies a plug-flow reactor is used which was located in the electric field maximum and connected with a gas supply (Bronkhorst, El-Flow). The reactor tube was filled with the catalyst (100 - 200 μm sieve fraction) to a bed length of 9.8 mm corresponding to a weight of 52.3 mg. A total gas flow of 20 ml/min was applied (gas hourly space velocity of 17 323 h^{-1}). The catalyst was heated to 400 °C with a heating rate of 10 °C/min. Preheated nitrogen (8 l/min) passed the reactor tube and heated the catalyst. After reaching the final temperature the experiment was performed subsequently under dry, wet, dry, wet, and dry feed conditions. The dry gas atmosphere contained 3 vol% propane, 6 vol% oxygen, and 91 vol% nitrogen. The wet gas atmosphere contained 3 vol% propane, 6 vol% oxygen, 5 vol% steam, and 86 vol% nitrogen. The gas purity was 99.95 vol%. The effluent gas flow was analyzed with an online gas chromatograph (Agilent 7890, equipped with poraplot and molesieve columns connected to a thermal conductivity detector and DB1 column connected to a flame ionization detector). A similar description of the method and the setup, which was improved throughout this thesis, was reported previously[15,20].

Near-ambient pressure X-ray photoelectron and soft X-ray absorption spectroscopy

In a subsequent step, the catalyst was investigated with NAP-XPS and NEXAFS spectroscopy in the total electron yield (TEY) mode. The experiments were conducted at the Innovative Station for In-Situ Spectroscopy beamline located at the BESSY II synchrotron in Berlin (Germany). The experimental setup is described in literature[175,176].

The catalyst (10 mg) was pressed into a pellet (diameter of 8 mm, 1 ton pressing pressure). Spectroscopic measurements were performed at 0.25 mbar and 400 °C with a heating rate of 10 °C/min. A near-infrared laser (808 nm, continuous wave) was used for heating. The experiment was started in dry propane gas atmosphere (1 N ml/min C_3H_8, 2 N ml/min O_2, 3 N ml/min He), changed to wet propane gas atmosphere (1 N ml/min C_3H_8,

2 N ml/min O_2, and 3 N ml/min steam), and vice versa. The reaction products were analyzed with proton-transfer reaction mass spectrometry (IONICON).

Core level spectra of C1s, V2p, and P2p were recorded at different kinetic energies. In the literature V_2O_5 is used as a model substance to calculate the inelastic mean free path (IMFP) applying the Tanuma formalism[177,178]. For this study, the computed IMFP was 0.55 nm, 1.4 nm at kinetic energies of 150 eV and 750 eV, respectively. In the following, it is referred to 0.55 nm as surface sensitive and 1.4 nm as "bulk" sensitive. The binding energy (BE) calibration was done using the C1s peak (BE of 284.4 eV). The $V2p_{3/2}$, P2p, and O1s peaks were fitted with Gaussian-Lorentzian functions after a Shirley background correction with CasaXPS software[179]. Gaussian-Lorentzian functions are a convolutions of Gaussian (considers instrumental response, thermal broadening, X-ray line shape) and Lorentzian (considers lifetime broadening) functions[180]. The averaged V oxidation state for the surface and "bulk" sensitive measurement was derived from the V^{4+} and V^{5+} peak area of the $V2p_{3/2}$ core level while the P/V ratio was calculated from the photon intensity and cross section corrected peak areas[181].

The secondary electron cutoffs and the valence band spectra were measured with constant photon energy of 100 eV. A voltage of -18.2 V was applied between detector and sample for the photoelectron cutoff measurements. A pass energy of 2 eV has been used.

The vanadium L_3-edge was recorded with photon energies of 505 - 560 eV and normalized to their maxima for a better comparison. The π^*-resonance of gas-phase oxygen (530.8 eV) was used for energy calibration[182].

3.2.3 Results and discussion

In-situ microwave conductivity

In order to probe the semiconducting and catalytic properties of the VPP catalyst the mirowave electrical conductivity was measured in propane oxidation under dry and wet feed conditions. To allow a direct comparison between VPP and $MoVTeNbO_x$ (M1-phase) the experimental conditions were equivalent to those reported by Heine *et al.*[22]. Figure 3.2.2 shows the microwave conductivity σ in (a) and the corresponding catalytic data in (b).

After reaching the final temperature of 400 °C the conductivity decreased asymptotically towards 0.017 S m^{-1}. Steam was introduced after 156 min. Then, the conductivity rapidly decreased in the first 90 min reaching a constant value of 0.015 S m^{-1} after 36 min. When the dry propane feed conditions were reapplied the conductivity spontaneously increased to

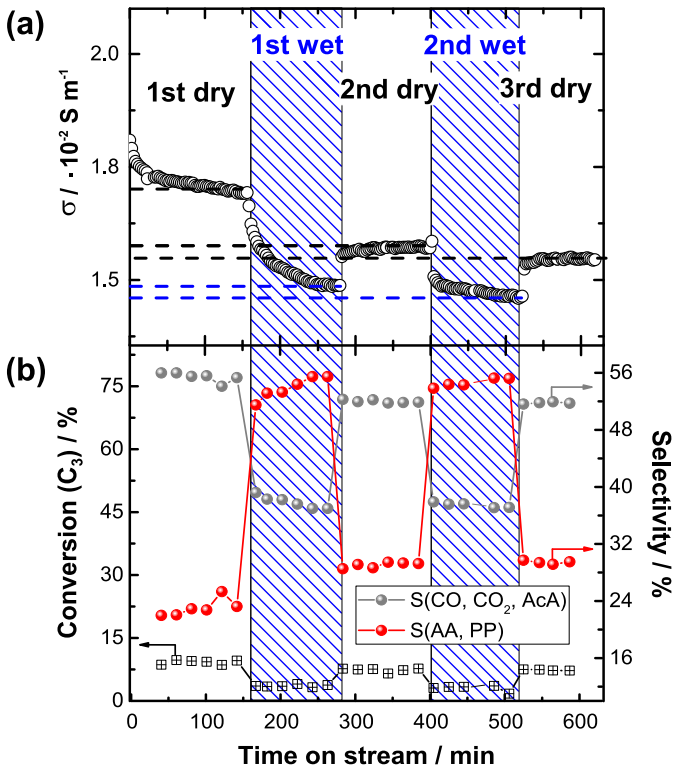

Figure 3.2.2: ***(a)*** *Microwave conductivity σ of VPP, and* ***(b)*** *Simultaneously measured catalytic performance under dry (3 vol% C_3, 6 vol% O_2, inert) and wet (3 vol% C_3, 6 vol% O_2, 5 vol% steam, inert) feed conditions at 400 °C. Further, S describes the selectivity of the oxidation products CO, CO_2, and acetic acid (AcA) as well the selective products acrylic acid (AA), and propylene (PP).*

0.016 S m^{-1}. After subsequent introduction of the reaction mixture the same conductivity changes were observed, i.e., a reduction (σ of 0.0146 S m^{-1}) under wet feed conditions in comparison to dry feed conditions (σ of 0.0155 S m^{-1}).

Overall VPP (0.017 S m^{-1}) is less conductive than $MoVTeNbO_x$ (M1-phase) (2.3 S m^{-1}) under similar experimental conditions[22]. It is well-known that VPP acts as a p-type semiconductor[13,14,17,18,166] in contrast to the n-type semiconducting $MoVTeNbO_x$ (M1-phase)[21,22]. The major charge carriers are electron holes in VPP[17,166]. Therefore, the electron hole concentration $h^{\cdot}$ increases when double ionized oxygen vacancies $V_O^{\cdot\cdot}$ are filled by oxygen O_2 from the reactive gas feed which is shown in equation 3.4 (Kröger-Vink notation). This means that the conductivity increases for VPP ($d\sigma/\mathrm{dp}(O_2) > 0$) and

decreases for $MoVTeNbO_x$ (M1-phase) ($d\sigma/\mathrm{dp}(O_2) < 0$) with increasing oxygen partial pressure in the gas feed [17,21,166].

$$O_2 + 2V_O^{\cdot\cdot} \rightleftharpoons 2O_O^X + 4h^{\cdot} \tag{3.4}$$

The impact of steam on conductivity seems to have different reasons, because the same conductivity response was observed for the p-type semiconductor VPP and n-type semiconductor $MoVTeNbO_x$ (M1-phase) [22] when steam was added to the propane feed. Therefore, a correlation between the charge carrier type and the observed behavior is excluded. To further investigate the influence of steam on the electrical conductivity, a reference experiment without propane was performed (cf. Figure B.3 of Appendix B). As a result, no conductivity response was found. Referring to equation 3.4, it is concluded that steam does not influence the double ionized oxygen vacancies $V_O^{\cdot\cdot}$ and, therefore, the overall electron hole concentration $h^{\cdot}$.

The catalytic performance was enhanced by steam in the propane feed (cf. Figure 3.2.2b) where the overall propane conversion alternated between 6 % (dry feed) and 4 % (wet feed) with a constant carbon balance close to 100 %. In agreement with the literature, propane is oxidized to propylene, CO, CO_2, acrylic acid, and acetic acid over VPP [48,54,55]. The selectivity towards the selective products (acrylic acid, interestingly also propylene) was increased by the presence of steam (dry feed: 23 %; wet feed: 54 %). This selectivity enhancement was accompanied by a reduced selectivity (dry feed: 77 %; wet feed: 47 %) of the oxidation products (CO, CO_2, and acetic acid). This could mean that, for example, a direct pathway of propane to CO_x is suppressed by steam addition. When the steam flow was turned off the selectivities returned close to the original values (selective products to 18 % and unselective products to 25 %) at the beginning of the experiment. More details about the catalytic performance including the product distribution are given in Figure B.2 of Appendix B.

There are some remarkable differences between $MoVTeNbO_x$ (M1-phase) and VPP in their catalytic performance as to the effect of steam in the propane feed. Steam increases the propane conversion over $MoVTeNbO_x$ (M1-phase) contrary to the present observation over VPP [22,59]. A comparable VPO study by Landi *et al.* also revealed a reduction of the propane conversion with steam [183]. Furthermore, steam reversibly triggers the selectivity towards propylene where the selectivity decreases over $MoVTeNbO_x$ (M1-phase) but increases over VPP. Some similarities were found regarding the increased selectivity to the desired product acrylic acid and the oxidation products (CO, and CO_2), however, keeping in mind the slight

reduced propane conversion in the presence of steam. The increase in acrylic acid selectivity was explained in the literature by the fact that steam suppresses the decomposition of acrylic acid to CO and CO_2 [22,48,59]. This change of different pathways through the reaction network and, therefore, a different reactant-product distribution, clearly influences the chemical potential of the abundant gas phase which affects the electronic and chemical state of the catalyst.

The general expression for the conductivity of a semiconducting solid is expressed by equation 2.13 where the conductivity of the p-type semiconducting VPP catalyst is determined approximately by its hole concentration N_h, Hall mobility $\mu_{H,h}$, and the elementary charge e; $\sigma(x) \approx |e| (N_h(x)\mu_{H,h})$ [97]. Furthermore, N_h can be expressed in terms of the effective hole density of states in the valance band N_{eff}^V, the difference between the valence band edge E_V and the Fermi level E_F and the thermal energy kT according to

$$N_h(x) = N_{eff}^V exp\left[-\frac{E_V(x) - E_F}{kT}\right] \tag{3.5}$$

Eichelbaum *et al.* showed that the surface induced band bending of VPP is triggered by the V^{4+}/ V^{5+} redox couple which changes with the abundant reaction gas feed [17,18,47]. Thus, a different chemical environment induced by steam in the reaction feed could possibly change the band bending (modifying the gap between $E_V(x)$ and E_F) and, therefore, the hole concentration N_h. A schematic band diagram for a p-type semiconductor is shown in Figure B.4 of Appendix B to further illustrate flatband, surface dipole, and band bending situations.

Above, a first indication to exclude such a concentration variation induced by steam for the conductivity reduction is reported. To confirm this statement, NAP-XPS core level and NEXAFS spectroscopy have been performed to identify changes in the surface chemical composition associated with the V^{4+}/ V^{5+} redox couple. These studies were accompanied by the valence band and work function measurement.

Near-ambient pressure X-ray photoelectron and Near-edge X-ray-absorption fine structure spectroscopy

XP survey spectra (E_{ph} of 860 eV, cf. Figure B.5 of Appendix B) were taken to check for impurities before performing high resolution XP core level scans. Impurities can promote or poison a catalyst and cause misleading interpretations of the XP spectra. V, P, O, and minor amounts of C and Si were found suggesting graphite and silica, respectively. Neither

graphite nor silica is known to influence selective oxidation reactions over VPP. Thus, these impurities do not interfere the analysis of the $V2p_{3/2}$, $P2p_{3/2}$ and V L_3-edge NEXAFS edge. The corresponding $V2p_{1/2}$ core level could not be evaluated since it overlaps with photoemission satellites of the $V2p_{3/2}$ core level. The $V2p_{1/2}$ core level is also affected by Coster-Kronig Auger-Meitner decay channels[184]. The analysis of the O1s core level is complicated by satellite peaks from the $V2p_{1/2,\ 3/2}$ in the oxidation state +5 and +4 reported by Zimmermann *et al.*[185]. Therefore, the O1s core level was not analyzed. The proton-transfer reaction mass spectrometry (PTR-MS) signal at m/z = 73 (mass of protonated acrylic acid) and m/z = 43 (mass of protonated propylene), recorded during all applied gas feeds, proves that the catalyst was under catalytic operation (cf. Figure B.6 of Appendix B). The general trend showed that the concentration of acrylic acid increases. The abundance of propylene decreases in wet feed and the trend for both species is reproducible.

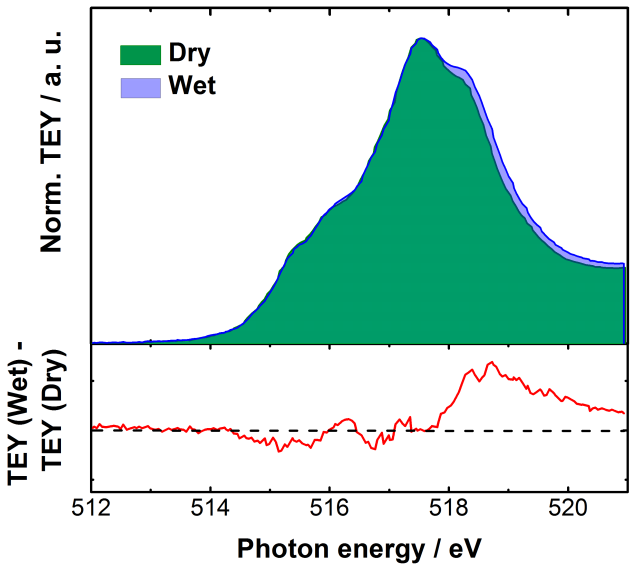

Figure 3.2.3: *V L_3-edge NEXAFS edge (TEY mode normalized to its maxima) of VPP (in dry $C_3/O_2/He$ (1/2/3 sccm) and wet $C_3/O_2/H_2O$ (1/2/3 sccm)) at 400 °C, 0.25 mbar. The difference spectra (TEY(Wet)-TEY(Dry)) is shown in the lower inset.*

The surface sensitive (IMFP: 0.55 nm) $V2p_{3/2}$ core level in dry and wet propane feed condition was analyzed together with the V L_3-edge NEXAFS edge. To achieve a physically and chemically reasonable fit to the $V2p_{3/2}$ core level the V L_3-edge NEXAFS edge was first analyzed due to the simple relationship between its edge energy position and the V oxidation state[186–188]. It is known that the photon energy position of the V L_3-edge edge increases with the V oxidation state. The edge position can be determined by a first momentum analysis[17,19,22,168,187].

Figure 3.2.3 illustrates the normalized V L_3-edge NEXAFS edge together with the difference spectrum between wet and dry feed conditions (TEY(Wet)-TEY(Dry)). A shift of intensities towards higher photon energies is found when introducing steam which can be clearly seen in the difference spectra. Accordingly, the first momentum of the V L_3-edge NEXAFS increases from 517.71 eV (dry feed) to 517.75 eV (wet feed) indicating an increase in the averaged V oxidation state.

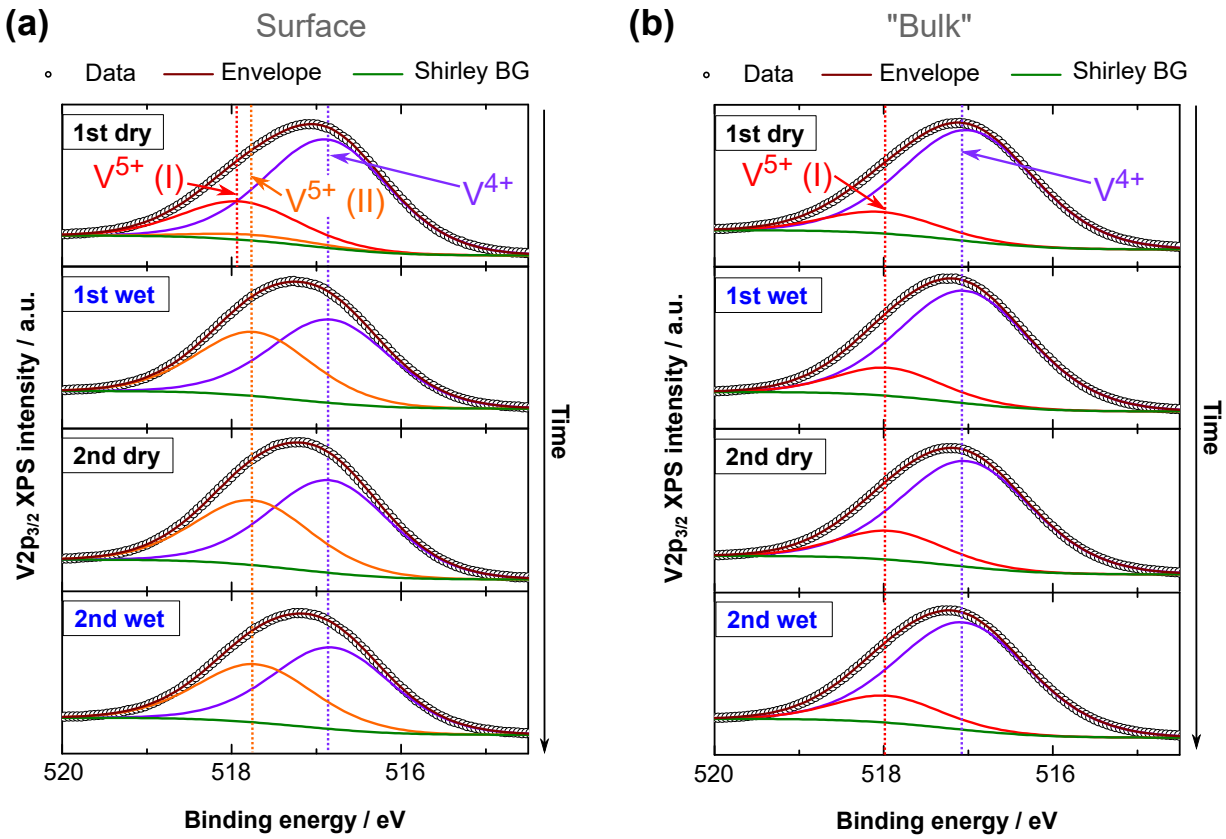

Figure 3.2.4: *V2$p_{3/2}$ core level spectra of VPP (in dry $C_3/O_2/He$ (1/2/3 sccm) and wet $C_3/O_2/H_2O$ (1/2/3 sccm)) **(a)** Surface sensitive mode and **(b)** "Bulk" sensitive mode at 400 °C, 0.25 mbar. Shirley BG describes the Shirley background correction.*

Keeping this finding in mind, the focus will now return to the analysis of the V2$p_{3/2}$ core level. The surface sensitive V2$p_{3/2}$ spectra are shown in Figure 3.2.4a. In the first dry propane feed, the best fit was achieved with three Gaussian-Lorentzian peaks with binding energies of 516.9, 517.8, and 518 eV. The peak at 516.9 eV binding energy is assigned to V^{4+} species[189–191] while the two peaks at 517.8 eV and 518 eV suggest V^{5+} species[18,192–195]. The peak at 517.9 eV is assigned to V^{5+} (I) since the energy splitting is about 1.1 eV and the

measured BE position is in good agreement with literature values (BE: 518 eV)[189–191]. The inclusion of a third peak at 517.8 eV (a second V^{5+} (II) species) significantly improved the accuracy of the fit quality. More details about the fit parameters are given in Appendix B (cf. Table B.3). Recently, a similar deconvolution of the $V2p_{3/2}$ core level into three species was reported for MoV and $MoVTeNbO_x$ (M1-phase) catalyst[196]. Next, steam was introduced in the chamber and the peak profile of the $V2p_{3/2}$ core level became narrower in comparison with the first dry feed condition. The V^{5+} (I) species (BE: 518 eV) was not observed while the peak area of the V^{5+} (II) species (BE: 517.8 eV) increased. The BE of V^{4+} remained constant. No significant changes in the subsequent variation between wet and dry feed and no significant changes of the V^{5+} (I) BE nor peak area in the "bulk" sensitive mode (IMFP: 1.4 nm) were found, c.f. Figure 3.2.4b.

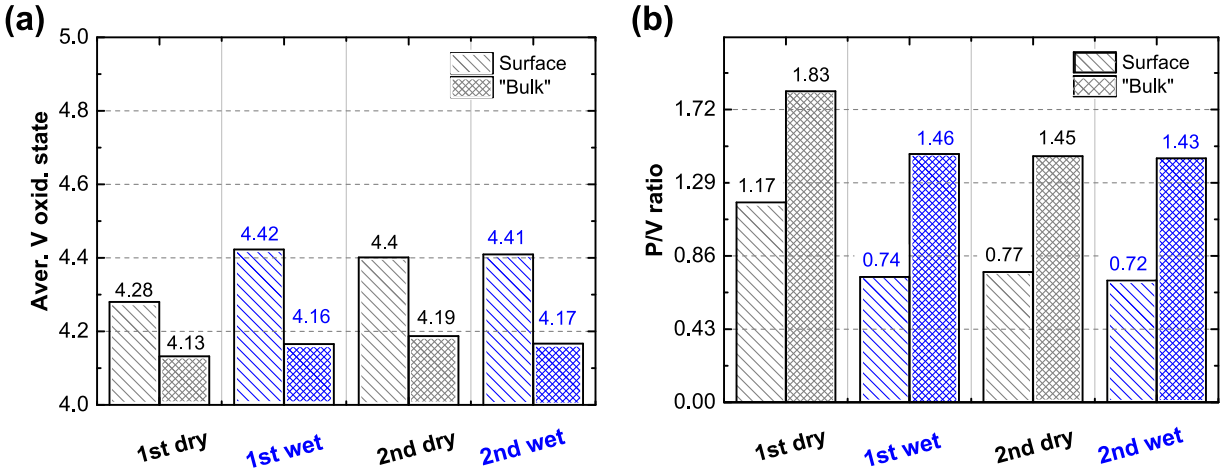

Figure 3.2.5: ***(a)*** *The averaged vanadium oxidation state of VPP as determined from $V2p_{3/2}$ core levels and* ***(b)*** *P/V ratio of VPP for surface and the "Bulk" sensitive mode in dry $C_3/O_2/He$ (1/2/3 sccm) and wet $C_3/O_2/H_2O$ (1/2/3 sccm).*

The averaged V oxidation state derived from V^{4+} and V^{5+} peak area of the $V2p_{3/2}$ core level is summarized in Figure 3.2.5a for all applied gas feed conditions. In the first dry feed an averaged V oxidation state of 4.28 for the surface sensitive mode and 4.13 for the "bulk" sensitive mode was found. The latter is close to the expected VPP bulk value of 4. These findings indicate that more V^{5+} species are present on the surface (higher degree of oxidation) and is in line with the shifted V L_3-edge NEXAFS edge. When steam is added to the propane feed the oxidation state increases to 4.42 (surface sensitive) and 4.16 ("bulk" sensitive), respectively. No significant changes were observed in the subsequent variation between wet and dry feed.

The overall V oxidation state in the range of 4.28 to 4.42 is in agreement with previous studies[18,47,197]. As already described in the introduction, the $MoVTeNbO_x$ (M1-phase) catalyst was found to exhibit an increasing averaged V oxidation state when steam is introduced in the propane feed[22,59]. The authors observed a reversible trend for the $MoVTeNbO_x$ (M1-phase) catalyst with steam in the propane feed which is in contrast to the presented results. The change in oxidation state was further analyzed for VPP by investigating the P/V ratio as a function of reaction conditions (cf. Figure 3.2.5b). For the surface sensitive mode a ratio of 1.17 was calculated for the first dry feed while in the first wet feed the ratio decreased to 0.74. In the subsequent treatment, the P/V ratio was almost constant (0.77 for the second dry feed and 0.72 for second wet feed). For the "bulk" sensitive mode the same trend was found. A ratio of 1/1/4.5 for V/P/O is proposed according to the Daltonid formula. This significant decrease of the P/V ratio indicates a loss of phosphorus. Hence, the hydrolysis of phosphate to P_xO_y is accelerated under the applied conditions leading to surface depletion in phosphorus. The phenomenon is well known. To compensate loss of phosphorus under real operation conditions, phosphorus organic reagents, such as trimethyl phosphate, are added in the industrial n-butane process[49,52].

Summarizing the XPS core level analysis steam in the propane feed irreversibly increases the averaged V oxidation state and depletes phosphorus in the topmost surface layer of VPP. After the first treatment in steam a new V^{5+} (II) species at lower binding energies (BE: 517.8 eV) increases. The species can be understood in terms of the modified chemical environment of the V^{5+} cation related to an increase in the overall oxidation state and a decrease in the P/V ratio in wet feed. These changes are detectable only in the surface sensitive mode, whereas the "bulk" sensitive mode just shows tiny changes. Steam leads to a rearrangement of the VPP surface chemical composition (formation of V_xO_y clusters) due to the loss of phosphorous. At this point it should be noted that the average V oxidation state in the $MoVTeNbO_x$ (M1-phase) catalyst which is more active and selective in propane oxidation compared to VPP, is always above 4.5[21].

Valence band spectra, secondary electron cutoff and work function

Referring to the in-situ microwave conductivity experiments, the conductivity reduce by steam is further analyzed. It is possible with photoelectron spectroscopy to determine the valence band position and, therefore, band bending variations which affects the electron hole concentration of VPP (cf. equation 3.5). Therefore, the valence band and the secondary electron cutoff E_{cutoff} were investigated in detail. In this context, one has to keep in mind

that photoelectron spectroscopy monitors the excited state of a solid[198]. In particular, photoelectron excitations into the conduction band affect the barrier height of the space charge layer in semiconductors[199].

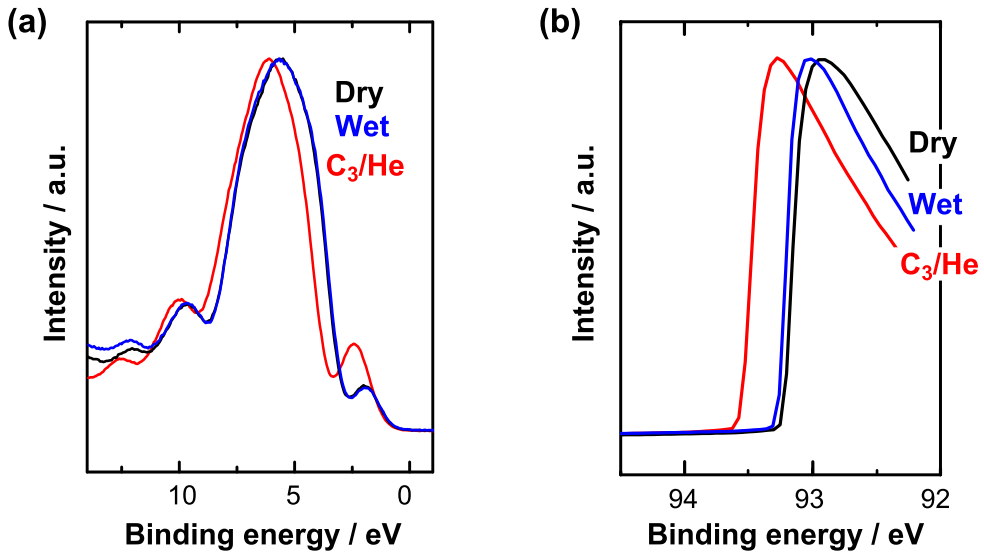

Figure 3.2.6: ***(a)*** *Valence band spectra (normalized to their maximum) recorded at $E_{h\nu}$ of 100 eV with constant photon flux, and* ***(b)*** *Secondary electron cutoff of VPP in different gas mixtures.*

The valence band spectra was recorded at $E_{h\nu}$ of 100 eV with constant photon flux for a comparison between valence band edge positions in VPP for different reaction feeds. The valence band spectra in the first dry, wet, and reducing C_3/He feed are depicted in Figure 3.2.6a. For a better comparison, the valence band spectra were normalized to their maximum. It can be clearly seen that the valence band edge position does not shift in a detectable manner by adding steam. The unaffected valence band edge position was also reported for the n-type semiconducting $MoVTeNbO_x$ (M1-phase)[22]. In addition, similar ultra-high vacuum studies of V_2O_3[200] and α-Fe_2O_3[201] did not exhibit any valence band edge variation upon steam adsorption. However, in reducing C_3/He feed a valence band shift to higher binding energies was observed. This shift is accompanied by a relative intensity increase of the valence band pre-edge feature at 1.9 eV BE (dry/wet feed) and 2.4 eV BE (C_3/He). This pre-edge shift to higher binding energy suggests a reduction of the surface induced accumulation layer as described by Eichelbaum *et al.*[47]. The corresponding states are assigned to occupied vanadium 3d states for VPP[47]. The increased pre-edge peak therefore indicates a higher V^{4+} concentration consistent with the oxidation state determined by analysis of $V2p_{3/2}$ core level peaks. Thus, the barrier height reduction is

caused by a change of the surface V^{4+}/V^{5+} redox couple. The change in the oxidation state induced by switching from dry to wet feed (cf. Figure 3.2.5a), however, is apparently too small to be reflected in the valence band spectra. Changes at the detection limit have been observed by variation of the alkane in the feed from ethane to propane to n-butane over $MoVTeNbO_x$ (M1-phase)[21].

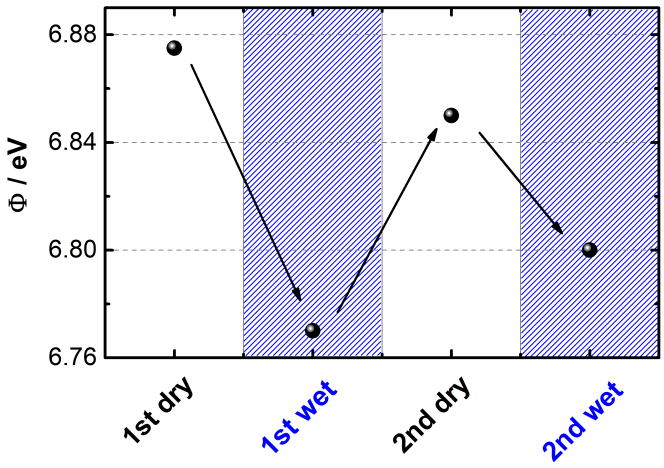

Figure 3.2.7: *Calculated work function Φ of VPP under dry $C_3/O_2/He$ (1/2/3 sccm) feed and wet $C_3/O_2/H_2O$ (1/2/3 sccm) feed at 400°C, 0.25 mbar.*

To confirm the results, the secondary electron cutoff E_{cutoff} is measured (cf. Figure 3.2.6b) from which the work function Φ at a given photon energy $E_{h\nu}$ can be deduced according to equation 3.6[202]. Figure 3.2.6 summarizes the results obtained for Φ. The above observed shift of E_{cutoff} is combined with a decreased Φ of 6.87 eV (first dry) to 6.77 eV (first wet). In the subsequent treatment, an increasing trend in dry (Φ of 6.85 eV) and decreasing trend in wet (Φ of 6.8 eV) feed was found.

$$\Phi = E_{h\nu} - E_{cutoff} \tag{3.6}$$

The reported values of Φ are comparable with those of previous studies for VPP (Φ = 6.94 - 6.7 eV in n-butane[47]) and V_2O_5 (Φ = 7 eV[203]). For the $MoVTeNbO_x$ (M1-phase) catalyst a clearly reversible work function change between 6.0 eV (wet) and 6.3 eV (dry) was found[22]. Hence, the change of Φ without changes in the valence band position can be interpreted as a modified surface dipole (cf. Figure B.4 of Appendix B). Steam does not change the space charge layer in VPP which is in agreement with previous observations[22,200,201].

3.2.4 Conclusions

The impact of steam on the selective oxidation of propane over VPP have been investigated. The propane conversion together with the selectivity towards the undesired products CO and CO_2 are reduced due to the addition of steam. Steam in the propane feed increases the selectivity towards the desired products acrylic acid and propylene. The combined microwave conductivity and near-ambient pressure X-ray photoelectron/absorption study reveals that these changes in the catalytic performance are accompanied by a modification of the electronic and (chemical surface) structure of the VPP catalyst. An incompletely reversible reduction of the microwave conductivity is observed when steam is present in the propane feed. Interestingly, the microwave conductivity is not affected by steam without propane. These findings are a strong indication that steam does not influence the electron hole concentration. This hypothesis is in line with the unaffected XP-valence band edge position and V3d pre-edge states. Since the electron hole concentration is influenced by the barrier height in the accumulation layer, as seen from equation 3.5, a modification of the charge carrier concentration by steam seems unlikely.

However, steam affects the electronic and chemical properties of the VPP surface. The complementary XP core level analysis showed that the VPP surface is irreversibly depleted in phosphorous which is accompanied by a modulation of the average vanadium oxidation state, i.e., increasing V^{5+} concentration. This observation can be understood in terms of a change in the anion-cation ratio (VO^{2+} vanadyl and $P_2O_7^{4-}$ pyrophosphate) at the surface by introducing steam in the propane feed. Furthermore, another electronically different V^{5+} component at binding energy of 517.8 eV has been detected which increases in the present of steam. The changed chemical composition at the VPP surface leads to a reduced surface dipole moment as seen from the shifted XP secondary electron cutoff.

A possible explanation for the conductivity response in the absence of a modified space charge layer is a change of the charge carrier mobility. Contact-free microwave Hall effect measurements can separate the charge carrier concentration and their mobility. In-situ microwave Hall effect investigations might be a very promising approach to a better understanding of the observed phenomena and the differences in selectivity in propane and n-butane oxidation, respectively, over VPP. Local properties such as the concentration/ nature of acid sites and number of propane adsorption sites may also be affected and contribute to the observed selectivity changes.

3.3 Design of a microwave Hall effect setup for studying in-situ electrical properties of powder catalysts

The intrinsic electrical properties of polycrystalline catalytic materials have been studied with the microwave Hall effect technique. This contact-free technique probes simultaneously the electrical conductivity and the Hall mobility to derive an absolute charge carrier concentration. Bimodal cavities are needed to observe the Hall effect at microwave frequencies. However, in-situ measurements for heterogeneously catalyzed reactions in such microwave cavities are challenging. Here, the design and the applications of a bimodal TE_{112} cavity is discussed for in-situ experiments at elevated temperatures. Well-characterized semiconductors such as silicon, germanium and zinc oxide were used to verify the accuracy of the setup including the efficiency of the integrated heating approach. Temperature-dependent measurements on a reference ZnO single crystal proved sensitivity and accuracy of the setup to characterize the temperature dependence of the electrical conductivity which is crucial for a system aiming at measuring the electrical properties under reaction conditions. This also holds for polycrystalline ZnO which was analyzed in a flow-through reactor relevant for catalysis. As a proof of principle, a Cu/ZnO model catalyst is tested for the reverse water-gas shift reaction. The presented in-situ microwave Hall effect setup is expected to be a starting point for more detailed charge carrier analysis to understand mechanisms of redox catalysis.

3.3.1 Introduction

Understanding the electrical properties of semiconducting materials is crucial for a wide range of application involving charge transfer processes. Chemical reactions of gas phase molecules at the surface of a semiconducting material, acting as a heterogeneous catalyst, are known to often change the electrical properties of the catalyst. However, only a few studies have reported the detailed characterization of these properties under catalytic conversion condition[9,11,13,18,204]. This is partly due to the fact that conventional two- or four-point methods being well established to measure electrical properties of macroscopic solids suffer from considerable challenges such as electrode contact stability, contact resistances, or polarization effects if applied to powdered materials often used in heterogeneous catalysis[15]. Recently, it was shown that microwave cavity perturbation as a contact-free technique

can be used to measure the electrical conductivity of powdered materials[15]. In particular in-situ experiments, which allow to measure the conductivity under catalytic reaction conditions, are possible and show a correlation between electrical conductivity and chemical activity[15,17,18,21,22]. On a microscopic level the electrical conductivity is governed by the mobility and the concentration of charge carriers. Hence, the question about the origin of an observed change in conductivity cannot be given based on conductivity measurements alone. In many cases the mobility of charge carriers is assumed to be constant which allows to associate changes in conductivity with corresponding changes of the charge carrier concentration[12,15]. However, providing experimental proof for a constant carrier mobility is difficult. Especially, in case of powdered catalytic materials the low mobility and the above mentioned contact-related problems impede a distinct assignment of mobility and concentration of charge carriers[28,98].

The resonant MHE is one possible option to measure the charge carrier mobility of powdered materials in a contact-free fashion[24,25,33,205]. In addition, such an experimental setup allows to measure the electrical conductivity simultaneously. Hence, a setup to measure the MHE allows to assign changes in electrical conductivity to an alteration of charge carrier mobility and/or to changes in charge carrier concentration[32,104]. The contact-free MHE technique is based on the same physical principal as conventional static Hall effect measurements where a Hall potential is measured. In the MHE, this Hall potential arises if a magnetic field is applied orthogonal to moving charge carriers being excited by the oscillating electric field of the microwave radiation due to the Lorentz force acting on the moving charge carriers. The Hall potential depends directly on the mobility of the deflected charge carriers. The detection scheme utilizes the orthogonal orientation of the exciting electric field and the resulting electric field due to the Hall effect. A sensitive detection of the Hall field in a contact-free manner by applying microwave fields is possible if a bimodal cavity is used (cf. Figure 3.3.1) which can accommodate two orthogonal resonance modes of identical frequency. In case of perfect orthogonality of the two modes an excitation of one mode would not affect the orthogonal mode and no microwave power would be coupled into this mode. By introducing a sample with charge carriers into the electric field maximum of both orthogonal modes the Hall effect generates a field oriented such that the orthogonal mode can be excited. Hence, microwave power transferred into the orthogonal mode is directly related to the oscillating electric field generated by the MHE and in turn to the mobility of the charge carriers in the introduced sample. The bimodal cavity is designed

such that the two modes can be addressed individually through two ports of the cavity as indicated in Figure 3.3.1.

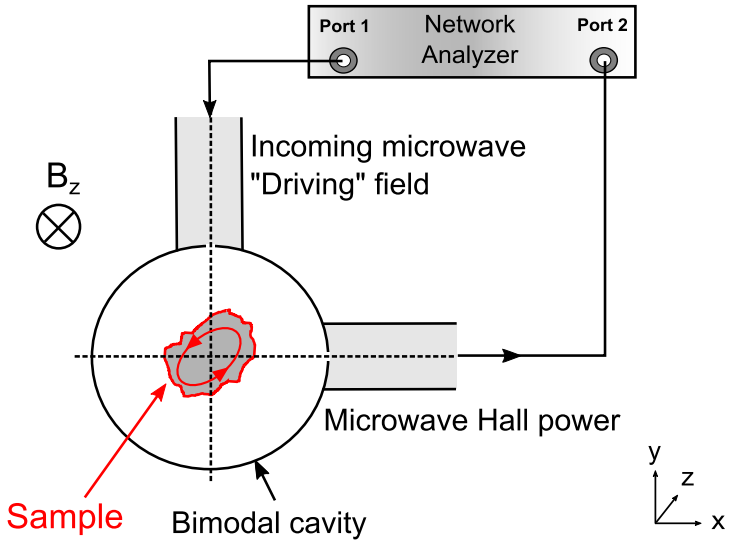

Figure 3.3.1: *Schematic sketch of the induced microwave Hall power of a bimodal cylindrical microwave Hall effect cavity, where the averaged charge carrier motion of the sample (red) is shown when applying a static magnetic field perpendicular to the direction of the electric fields of both modes.*

In the past, the MHE technique was successfully applied to various materials [26–28,40,98,102,104]. Further, MHE measurements after ex-situ treatment at elevated temperatures and different gases were reported, e.g., for ZnO powder [38,39,41]. However, for a proper use in heterogeneous catalysis measurements both elevated temperatures and controlled reactive gas atmospheres are required. Even though it has been shown for microwave cavity perturbation measurements that in-situ experiments in microwave cavities are feasible [15,206,207], it is still a challenge since no commercial equipment is available and a heatable quartz plug-through reactor has to be placed into the bimodal cavity needed for MHE experiments without diminishing the accuracy and sensitivity of the measurement. To the best of my knowledge this has not been reported for MHE measurements so far and is subject of the present work.

Here, an in-situ MHE setup is presented based on an optimized bimodal TE_{112} cavity operating at 9.4 GHz. This setup allows to measure both charge carrier mobility and electrical conductivity of powdered catalysts under catalytically relevant conditions. Well-known Si, Ge, and ZnO single crystals as well as ZnO powder are used to characterize the new setup. ZnO was used as material to prove the principle of the method due to its crucial and still debated role in the large scale industrial synthesis of methanol using a

$Cu/ZnO/Al_2O_3$ catalyst[67,116]. The temperature dependence of the electrical conductivity and of the charge carrier mobilities for a ZnO single crystal and ZnO powder are presented. ZnO, which is impregnated with Cu, is also active in the competitive reverse water-gas shift reaction. That is why in-situ measurements on a Cu/ZnO model catalyst under reverse water-gas shift reaction conditions at ambient pressure are performed and complete our results.

3.3.2 Experiment

Samples

Moderately doped single crystal standard samples were purchased from Crystal GmbH Berlin and n-, p-type Si and Ge as well as ZnO are investigated. The Si and Ge crystals were polished on one side. The sizes of the single crystals were chosen according to the microwave absorption (avoiding too strong absorption and hence disturbation of the fields in the cavity) resulting in volumes between 0.4 - 3.5 mm^3.

The synthesis and characterization of the investigated ZnO powder and Cu/ZnO model catalysts have been published earlier[23]. A detailed description of the ZnO and Cu/ZnO sample preparation is given in Appendix C.

Static Hall effect technique

To calibrate the MHE setup conventional static Hall-effect measurements were carried out in van-der-Pauw geometry. N- and p-type Ge, Si, and n-type ZnO samples were used with sizes ranging from 7 to 20 mm^2. The thickness of n-, p-type Si, and p-type Ge was 0.5 mm while the thickness of n-type Ge was 0.4 mm. The ZnO sample had a thickness of 1 mm. All samples were sonicated in acetone and isopropyl alcohol, afterward rinsed with deionized water and, in case of Ge and Si, treated by hydrofluoric acid to remove native surface oxides. Ohmic contacts to n- and p-type Ge were prepared by thermal evaporation of about 100 nm Ni and Al, respectively, followed by alloying at 340 °C. The Si sample was contacted similarly by Al while for ZnO a stack of 100 nm Ti and 25 nm Au was employed. Depending on the contact and the sample resistance the current through the sample was set between 0.2 to 15 mA and kept constant during the measurements. The Hall-voltage was measured in a magnetic field of about 640 mT. To confirm trends in temperature-dependent MHE measurements the temperature dependence of the Hall mobility was determined for the ZnO single crystal between 23 °C and 267 °C.

In-situ microwave Hall effect technique

The cavity perturbation and MHE technique were used to measure the microwave conductivity σ and microwave Hall mobility μ_H. The principle of measurement was described in the introduction part of this Chapter. Further information can be found in Chapter 2.2.1.

First, the microwave conductivity σ is calculated according to the equations 2.15 and 2.16 of Chapter 2.2.1. Here, the focus is on single crystals and powder samples for which the conductivity is of intermediate and low range, respectively. Furthermore, Appendix C shows the detailed derivation of the full equations. Second, the microwave Hall mobility μ_H is based on equation 2.19 introduced in Chapter 2.2.1. This equation will be discussed further in Chapter 3.3.3. Third, knowing the conductivity σ and mobility μ_H of a sample the concentration of charge carriers N_C can be obtained from the simple relationship

$$N_C = \frac{\sigma}{\mu_H e} \tag{3.7}$$

with e being the elementary charge[24,32].

The experimental equipment of the in-situ MHE setup is introduced in this Chapter. A detailed analysis of the in-situ bimodal TE_{112} cavity will be given later in Chapter 3.3.3. The custom-designed cavity is schematically drawn in Figure 2.2.3b which was introduced in Chapter 2.2.3. A cylindrical bimodal cavity with an inner diameter of 28 mm and a height of 42 mm was used[31,104]. The TE_{112} mode was excited for the experiment with a resonance frequency of 9.4 GHz of the empty cavity. The cavity was made of high purity copper and the inner walls were plated with 15 μm silver and subsequent 5 μm gold to suppress a degradation of the surface conductivity (made by company Detlef Janke, Berlin). The gold layer was polished. The bimodal cavity was connected with waveguides (WR 90; UKW-Berichte). An adapter (WR-90 waveguide square cover flange to SMA female; Pasternack) connected the waveguide with the coaxial cable (flexible precision cable; Pasternack) which was attached to the network analyzer (4-Port PNA N5222A operating between 10 MHz and 26.5 GHz; Agilent). The cables were calibrated by an electronic calibration module (N4691B ECal; Agilent). Four nylon tuning screws were developed with different tips (two with brass and two with wooden tips). These tuning screws (metric M4 thread) have a length of 65 mm and a tip length of 22 mm (Figure C.2a of Appendix C). The coupling of the microwave lines to the bimodal cavity was realized by irises consisting of an iris hole and an iris screw. The diameter of this iris hole was 5 mm[104] and a screw in front of the iris allows to adjust the matching conditions[88]. The iris screws were made

of teflon with metallic tips. The length of the iris screw (metric M6 thread) was 30 mm while the length of the metallic tip was 5 mm (Figure C.2b of Appendix C).

The quartz tube reactor had an outer diameter of 3 mm (CFQ tube; Rototec-Spintec GmbH). The tube reactor was surrounded by a 6 mm outer diameter single-walled quartz Dewar and connected upstream with a gas supply (EL-Flow; Bronkhorst). Heating of the sample was performed by a nitrogen stream (6 l/min) preheated in a furnace (tungsten heater). The temperature was measured by a thermocouple (Type K) and regulated using a proportional-integral-derivative controller (Eurotherm 2408). The thermocouple was located inside the reactor tube and outside the cavity. Prior to the measurements the temperature at the position of the sample was calibrated against the thermocouple reading. The bimodal cavity was water cooled by copper tubes soldered to the outside walls of the copper-body. The temperature of water-cooling circuit was controlled by a chiller (Polar Accel 250 SU LL; Thermo Scientific). An external magnet (1 Ω; ZWG) was used to apply the magnetic field measured by the Hall probe located in the center of the pole caps.

Temperature-dependent measurements were done using a ZnO single crystal and ZnO powder. The single crystal had a volume of 1.64 mm^3. The powder ZnO sample was filled into a reactor tube (sample weight of 21 mg, bed length of 5 mm, and a sieve-fraction of 100 - 200 μm). Both samples were heated up to 230 °C in inert atmosphere (100 % N_2) with a total flow of 5 ml/min to remove adsorbed water[23]. Then, the temperature was reduced stepwise to room temperature. The resonance frequency f_l and quality factor Q_l of S_{11} and S_{21} of the sample-loaded cavity were measured after reaching steady state conditions at the desired temperature. The time to establish a steady state varied slightly and the values of at least five averaged values (where each value is an average of three) were used. The measurement was repeated with an empty quartz tube reactor to obtain the response of the empty tube (f_e, Q_e of S_{11} and S_{21}).

The in-situ experiments were performed with ZnO and Cu/ZnO powder. The quartz tube reactor was filled with 10.8 mg (12.3 mg) of the sieved ZnO (Cu/ZnO) powder and fixed between two small quartz wool plugs. The sieve fraction was 100 - 200 μm. The quartz tube reactor was connected upstream with a gas delivery manifold and the model catalytic systems were tested under reverse water-gas shift reaction at 230 °C namely using a gas mixture of H_2/CO_2/He (3/1/6). A total gas flow of 3 ml/min was applied. The effluent gas flow was analyzed by an online micro gas chromatograph (Varian CP-4900, equipped with PoraPLOT and COx columns). Prior to the activity tests, the samples were reduced

in-situ in a 5 vol% H_2/95 vol% He flow (total flow of 5 ml/min) with a heating ramp of 2 °C/min to 250 °C for 30 min.

3.3.3 Results and discussion

Design of the in-situ bimodal TE_{112} cavity

Based on previous work[103,104] a cylindrical bimodal cavity operating in the TE_{112} mode was modified to measure MHE under in-situ conditions as detailed below. Figure 3.3.2a shows a sketch of the in-situ MHE setup with a TE_{112} cavity. This cavity has two electric field maxima[103] along the z-axis as seen from Figure 3.3.2b which shows the electric field amplitude of the cylindrical TE_{112} mode in the yz plane as a colored map. A sketch of electric and magnetic field distribution for this mode is shown in Figure C.3 of Appendix C. The sample position was chosen at the maximum of the electric field which according to the simulation is found at a quarter of the cavity height (middle of the cavity upper half part). Accordingly, the tuning screws are placed in the middle of the cavity lower half part (cf. Figure 3.3.2b labeled with 2a, and 2b). This follows the positions published by Ong *et al.*[103].

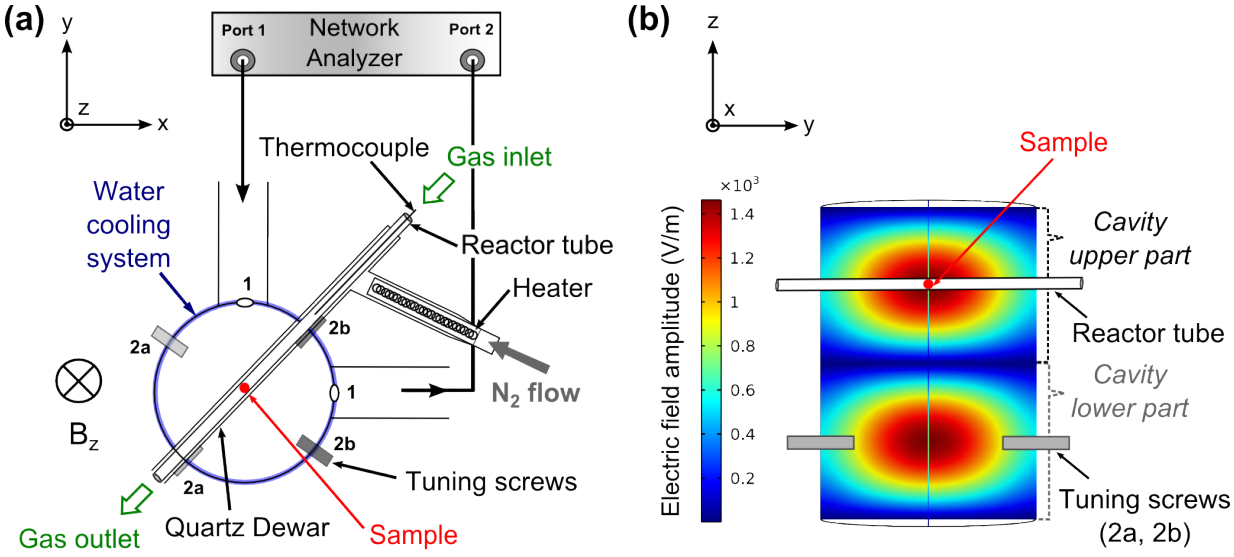

Figure 3.3.2: *Basic sketch of* **(a)** *In-situ bimodal TE_{112} cavity, with 1 iris screws, 2a tuning screws with wooden tip, and 2b tuning screws with metallic tip, and* **(b)** *Electric field amplitude simulated with COMSOL 5.1.*

As mentioned before, the inner wall of the bimodal cavity was silver-gold plated. This plating suppresses deterioration of the Q value of the cavity due to possible oxidation of

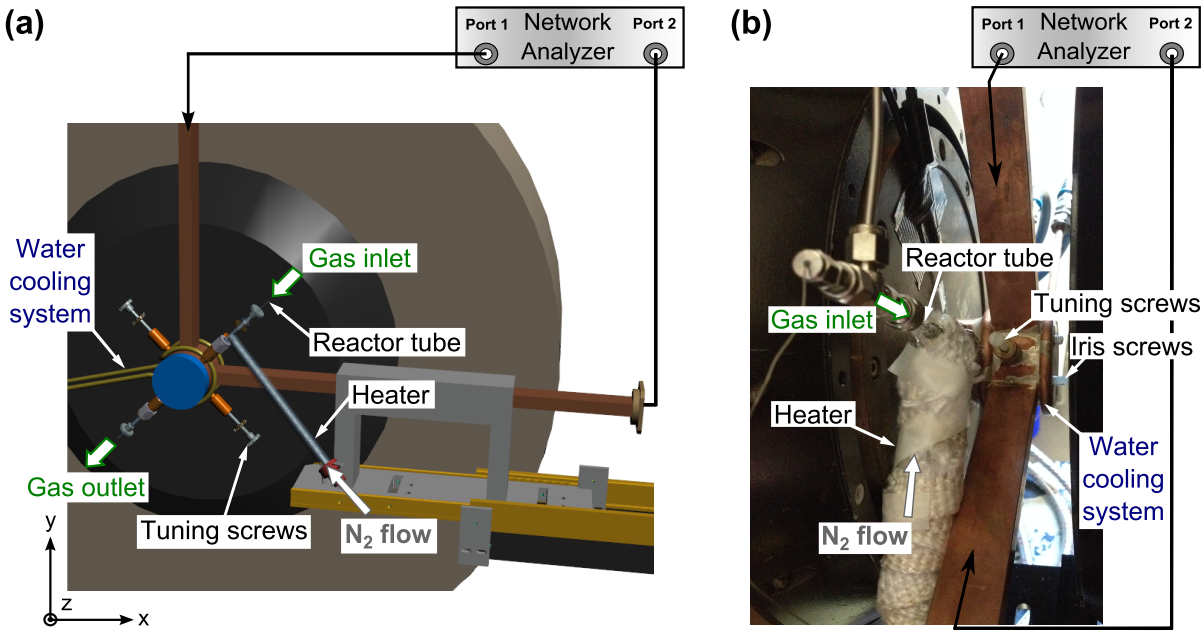

Figure 3.3.3: ***(a)*** *Basic design drawing, and* ***(b)*** *Photograph of the experimental setup.*

the inner surface of the cavity at elevated temperature. Nylon tuning screws (labeled with 2a,b in Figure 3.3.2a) were used due to their higher stability and better fixation compared with conventional brass screws. Holes of 6 mm diameter were inserted into the cavity walls to accommodate the stack of quartz Dewar and plug-through reactor. The size of these holes were chosen to maximize access without deteriorating the empty quality factor of the resonator significantly (cf. equation 2.19 of Chapter 2.2.1). As mentioned above, the microwaves were coupled into the cavity via a hole called iris. It was decided to use an iris coupling to achieve critical coupling conditions since it is easier to construct and to operate compared with fine slit coupling.

After increasing the sample holes a heating system was introduced to allow high temperature measurements. Similar to the work of Eichelbaum *et al.*[15] a quartz Dewar was implemented and a custom-designed spiral tungsten heater (0.6 mm wire, total length of 12.5 cm) was used. The heater was connected with a high current power supply (Cotek AE-800-24) to heat nitrogen gas which flows alongside the reactor tube to heat the sample. The flow-through reactor tube used for catalytic measurements was inserted into the quartz Dewar and connected upstream and downstream to the gas supply manifold and the gas analytics, respectively. A decrease of the quality factor Q from 5200 to 2000 was observed by introducing the quartz Dewar and the reactor tube into the empty cavity. The gas outlet

of the reactor is designed to attach an online gas analysis system for characterizing the gas phase composition during catalytic reactions.

Figure 3.3.3a illustrates the design drawing concept while Figure 3.3.3b shows a photograph of the in-situ bimodal TE_{112} cavity under operation conditions.

Tuning of the in-situ bimodal TE_{112} cavity

The excited TE modes are not perfectly orthogonal to each other due to imperfections of the cavity such as holes and screws[104]. Therefore, the different tuning screws are used to adjust both modes by their resonance frequencies and to correct for orthogonality. As discussed before, the reflection coefficients of the network analyzer were used to monitor the primary mode S_{11} and the secondary mode S_{22} simultaneously. The tuning of the cavity follows procedures given in literature[31,104]. For the first rough adjustment, all screws are removed and the Dewar and the reactor tube are inserted into the cavity. Second, the tuning screws with metallic tip (2b, Figure 3.3.2a) and the tuning screws with wooden tip (2a, Figure 3.3.2a) are inserted subsequently. The electric field is perturbed by the metallic tip and the resonance frequency is shifted to lower values whereas the wooden tip (dielectric material) leads to a shift of the resonance frequency to slightly higher values. Tiny changes in the shape of the resonance curve were observed (in other words, the resonance peak width which is related to Q, cf. equation 2.8 of Chapter 2.1.3). Initially, the screws were positioned to equalize the resonance frequencies of both modes. In a second step, the transmission coefficient S_{21} is minimized by adjusting the wooden screws. In addition, the iris screws are used to achieve critical coupling at both ports. After the first adjustment, all tuning screws are utilized for a final fine tuning. At optimum tuning conditions, S_{11} and S_{22} yielded the same frequency (with an isolation of 35 - 40 dB). The S_{21} curve had a symmetric resonance shape and an isolation of 30 dB. Ong *et al.*[31] reported 34 dB of isolation for the residual transmission signal. This residual signal can be further reduced by implementing a canceling channel[38,39] as discussed in Chapter 3.4.

Apart from the transmitted signal in the absence of an external magnetic field contributions to the transmitted signal introduced by the external magnetic field need to be considered. The Hall effect from the cavity inner wall was reported to contribute to the measured transmission signal S_{21}[28,39]. This wall Hall effect has been quantified in the past. Trukhan reported a theoretical mobility of 6.6 $cm^2V^{-1}s^{-1}$ and an experimental value of 4 $cm^2V^{-1}s^{-1}$ for a silver-coated cavity[208]. Fletcher measured 1 $cm^2V^{-1}s^{-1}$ for his system[112]. As a consequence, all above mentioned contributions (e.g., of the cavity

wall, non-ideal mode coupling, and others) have to be taken into account when measuring low-mobility samples. For example, Fletcher reported that microwave Hall mobility values lower than 1 $cm^2V^{-1}s^{-1}$ seem to be difficult to achieve[28,112].

The mobility found for the investigated samples (i.e., ZnO powder 2.5 - 125 $cm^2V^{-1}s^{-1}$)[41], is higher than the cavity wall Hall effect. Altogether, a characteristic increase of S_{21} is expected and due to the contributions discussed above, the Hall mobility μ_H is assigned in the following to the absolute change in $\Delta(P_H/P_1)^{1/2}$ / ΔS_{21} according to

$$\mu_H = K\frac{10^4}{B}\left(\frac{Q_e}{Q_e - Q_l}\right)\Delta\left(\frac{P_H}{P_1}\right)^{1/2} = K\frac{10^4}{B}\left(\frac{Q_e}{Q_e - Q_l}\right)\Delta S_{21} \tag{3.8}$$

where Δ = B-On - B-off is the difference between with and without external magnetic field B[24]. The Hall power P_H is connected with S_{21} according to equation 2.18 in Chapter 2.2.1. This procedure assumes a negligible mobility value of the empty reference measurement which may lead to an uncertainty in the absolute Hall mobility μ_H value for the sample. For future work this uncertainty of the empty cavity measurement can be corrected by coating of the cavity inner wall (cf. Chapter 3.3.5).

Calibration of the in-situ microwave Hall effect setup

The determination of absolute Hall mobilities using the in-situ MHE setup requires proper calibration, in particular the determination of the cavity constant K. Two strategies can be applied to calibrate the MHE setup, (i) single-point calibration where a reference sample is measured at a specific magnetic field and (ii) multi-point calibration where the measurement extends over a larger range of magnetic fields. The single-point calibration is fast and various reference samples can be measured quickly while it is less accurate. The multi-point calibration is more precise but the measurements are time-consuming. Both calibration methods were employed for the in-situ setup. N- and p-type Si were chosen as reference material to compare our results with the published data of Na *et al.*[104]. N- and p-type Ge as well as ZnO were additionally investigated to cover a broad range of materials with different electrical properties. The latter material was added to have a well-defined reference sample for comparisons with the ZnO powder and the Cu/ZnO model catalyst. In all cases the size of the single crystal samples were chosen small enough to ensure a homogeneous electric field over the entire sample.

The reference Hall mobility $\mu_{H,DC}$ of the single crystals is required to determine the calibration constant K and measured by conventional static Hall effect. The results for K

Table 3.1: *The determination of the calibration constant K is shown for the in-situ bimodal TE_{112} cavity system. The reference static Hall mobility values $\mu_{H,DC}$, the quality factor of the empty Q_e and sample-loaded Q_l cavity, the external magnetic field B, and the absolute change in $\Delta(P_H/P_1)^{1/2}$ are summarized for p-, and n-type Si and Ge. The arithmetic mean and its standard deviations are presented. The error of K is obtained from equation 4.28.*

	Si (p-type)	**Si (n-type)**	**Ge (p-type)**	**Ge (n-type)**
$\boldsymbol{\mu_{H,DC}}$ **/** $\boldsymbol{cm^2V^{-1}s^{-1}}$	266	1248	1754	2330
$\boldsymbol{Q_e}$	4086 ± 386	5022 ± 150	5191 ± 45	5081 ± 49
$\boldsymbol{Q_l}$	2479 ± 247	2206 ± 510	1774 ± 17	3768 ± 151
$\boldsymbol{B}$ **/** $\boldsymbol{T}$	0.6 ± 0.005	0.6 ± 0.005	0.6 ± 0.005	0.6 ± 0.005
$\boldsymbol{\Delta(P_H/P_1)^{1/2}}$ **/** $\boldsymbol{\cdot 10^{-2}}$	0.21 ± 0.01	2.9 ± 0.8	2.0 ± 0.1	1.4 ± 0.1
K	3.0 ± 1.1	1.5 ± 0.7	3.4 ± 0.4	2.5 ± 0.5

are presented in Table 3.1. Here, the lower and upper limit of K was determined from the maximum error of the combined measured quantity (cf. equation 4.28 of Appendix C). For the Si samples the computed K value was 3.0 ± 1.1 (1.5 ± 0.7) for p-type (n-type). For the Ge samples the experiments yielded a K value of 3.4 ± 0.4 (2.5 ± 0.5) for p-type (n-type). When comparing to the theoretical K value[25] of 2 and the experimental K values[104] of 2.14 and K values[102] of 2.97, 2.01 - 2.05 reported by others, the obtained calibration constant K is in a similar range. However, a large maximum error of K was calculated for p-type Si which is related to the significant contribution of standard deviations of Q_e and Q_l.

Further, a higher K value was observed for p-type doping compared to n-type doping for both Si and Ge. A closer look into literature confirms this trend (1.68 - 1.85 for n-type Si and 2.56 - 2.89 for p-type Si)[104]. However, this point has not been explained in the past. The difference could be related to the lower Hall mobility for holes compared to electrons in Si and Ge (cf. Table 3.1) because of different band structure and scattering mechanisms of these two carrier types[209]. These two charge carrier type have different effective masses which in turn determines the mobility (smaller effective mass results in a higher mobility).

In a next step, ZnO was investigated where the majority type of charge carriers are electrons since the native defects are attributed to oxygen vacancies, zinc interstitials, and Zn-on-O antisites[110,117,118]. The n-type ZnO gave a K of 2.8 ± 0.4 using the single-point

calibration. To confirm the validity of this value the multi-point approach was adopted. According to equation 3.8, the term $\Delta(P_H/P_1)^{1/2}$ should depend linearly on B. Therefore, the slope m of the linear regression is related to K and given by

$$K = \frac{\mu_{H,DC}\,(Q_e - Q_l)}{m 10^4 Q_e} \tag{3.9}$$

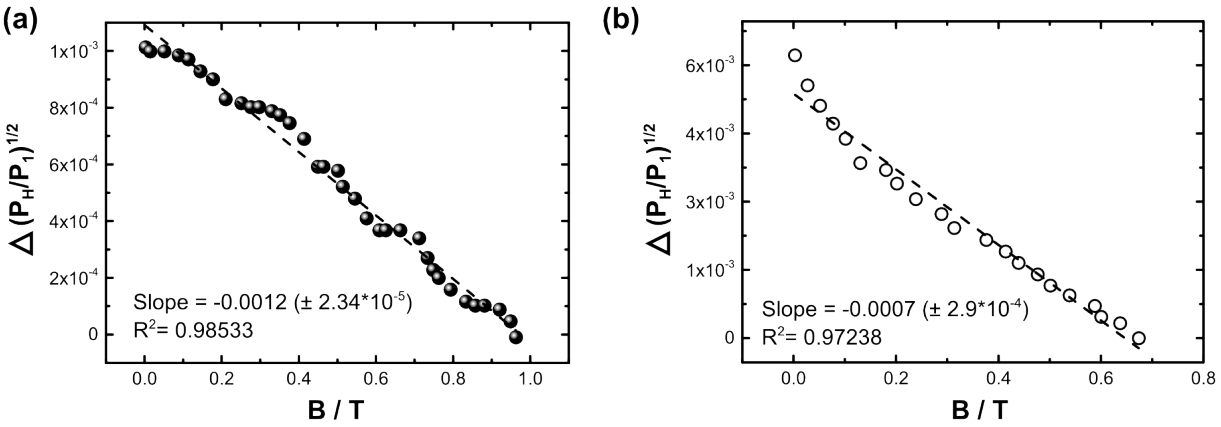

Figure 3.3.4: *Change of the Hall power $\Delta(P_H/P_1)^{1/2}$ with respect to the applied magnetic field B for* ***(a)*** *ZnO single crystal and* ***(b)*** *ZnO powder.*

Experimentally, an almost linear dependency of $\Delta(P_H/P_1)^{1/2}$ on B was obtained for the ZnO single crystal which shows that the in-situ setup performed properly, c.f. Figure 3.3.4a. The data are corrected by a cavity signal ($m = 7.76{\cdot}10^{-5}$) which is observed for the setup with an empty sample tube. The corresponding calibration constant K was 3.1 ± 0.3. In addition to the single crystal, ZnO powder was also studied which is shown in Figure 3.3.4b. Except for low fields the powder shows a linear dependence of $\Delta(P_H/P_1)^{1/2}$ on B. The slope of the curve is reduced to about 60 % of the value found for the single crystal. Using the cavity constant K of 3.1 ± 0.3, the effective Hall mobility μ_H for the ZnO powder was determined to be 23 ± 3 cm^{2}V^{-1}s^{-1}. This is in the range of reported microwave Hall mobilities for ZnO powders (2.5 - 125 cm^{2}V^{-1}s^{-1})[41].

In addition, the effective conductivity σ of ZnO powder was measured to yield $1.2{\cdot}10^{-4}$ S cm^{-1}, which is an order of magnitude lower than values for ZnO powders reported in literature using a MHE setup (2.4 - $3.3{\cdot}10^{-3}$ S cm^{-1})[38,39]. It is to be noted, that both conductivity and mobility of powders depend strongly on the crystallinity, defect density, surface etc. and, hence, on the preparation conditions which might be an explanation for the observed difference.

The single-point experiment at 600 mT is chosen for further investigations. This is justified as the cavity constant determined by the single point measurements are well in line with the ones extracted from the linear extrapolation scheme.

Temperature dependence of microwave conductivity and Hall mobility in ZnO

In a next step the MHE setup was tested at elevated temperature. ZnO was again chosen as a suitable test material since its single crystal can be measured both contact-free and contacted.

The contact measurements are shown as reference in Figure C.4 of Appendix C. Figure 3.3.5 shows results of the contact-free measurements of the conductivity σ and Hall mobility μ_H for a ZnO single crystal and for a ZnO powder. The data are corrected by the empty cavity signal.

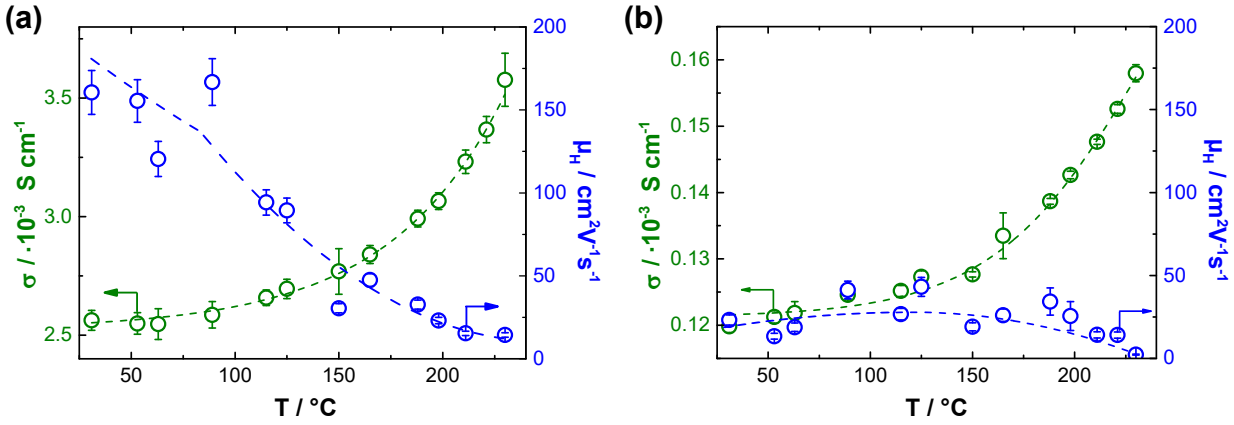

Figure 3.3.5: *Temperature dependence of the conductivity σ (green), and Hall mobility μ_H (blue) of* ***(a)*** *ZnO single crystal and of* ***(b)*** *ZnO powder in a flow-through reactor under inert gas atmosphere. A trend line was added to guide the eye.*

For ZnO single crystal (Figure 3.3.5a), an increase in conductivity σ and a decrease in Hall mobility μ_H was observed with increasing temperature. The conductivity rose slowly between 31 °C to 89 °C followed by a larger increase until 230 °C. The Hall mobility μ_H decreased slightly up to 100 °C followed by a larger decrease with increasing temperature. Obviously, the mobility value measured at 90 °C deviates significantly from the trend line. Temperature-programmed desorption measurements were performed, but no adsorbed species was identified that could explain this spike in the data. To confirm a different behavior for the microwave Hall mobility measurement, more data points are needed around 90 °C. The comparative static Hall measurements for the ZnO single crystal exhibit a

steady decrease of the Hall mobility μ_H with increasing temperature (cf. Figure C.4 of Appendix C). At lower temperatures, the microwave mobility is significantly larger than the static mobility, while the values converge at higher temperatures. The difference between the absolute conductivity must be due to the different type of measurement (different volumes probed by each method), cf. Chapter 3.1.

For ZnO powder (Figure 3.3.5b), a similar behavior was observed for the conductivity. With increasing temperature, the effective powder conductivity increases slowly between 31 °C to 150 °C followed again by a larger increase until 230 °C. In contrast, the Hall mobility μ_H remains constant until 160 °C, followed by a slight decrease for temperature above 160 °C. However, an interpretation for the ZnO powder sample may not be reliable due to the small variations and the scattering of μ_H.

Below about 150 °C, the absolute Hall mobility values for the ZnO single crystal are considerably higher compared to ZnO powder. A Hall mobility μ_H value of 160 ± 15 $cm^2V^{-1}s^{-1}$ at 31 °C was measured (132 $cm^2V^{-1}s^{-1}$ at 37 °C in the reference experiment, cf. Figure C.4 of Appendix C) for the single crystal. Static μ_H values for different ZnO single crystals reported in literature range from 205 $cm^2V^{-1}s^{-1}$ [210], 300 $cm^2V^{-1}s^{-1}$ [211] (Monte-Carlo simulation), 90 - 140 $cm^2V^{-1}s^{-1}$ [212], to 180 $cm^2V^{-1}s^{-1}$ [213]. This comparison shows that the measured values are consistent with published data which confirms the validity of the in-situ MHE setup. Furthermore, the increasing conductivity with increasing temperature for the ZnO single crystal is also in line with published data [118].

It is known that carriers which travel through a semiconductor encounter different scattering mechanisms which influence the carrier mobility [110]. The dominating scattering processes are phonon scattering and ionized impurity scattering. It is further explained that the $T^{-3/2}$ dependency describes phonon scattering whereas the $T^{+3/2}$ dependency describes scattering from charged defects [97,110]. Regarding ZnO, Rupprecht reported a dependence of $\mu_H \propto T^{-3/2}$ for a ZnO single crystal near room temperature [212]. Since the mobility decreased with increasing temperature, the phonon scattering might be also the dominating process for the investigated temperature range. The increased scattering due to thermal vibrations decreases the scattering time which is related to the lowered mobility. For polycrystalline ZnO, the decreasing μ_H with increasing temperature is small which shows that the charge transport process is more complex, e.g., contribution of multiple scattering processes.

Electrical properties under reverse water-gas shift reaction conditions

In the following a first model study is presented for the in-situ determination of the electrical properties using the reverse water-gas shift reaction ($CO_2 + H_2 \rightarrow CO + H_2O$, c.f. Chapter 1.3) at 230 °C as proof of concept. A Cu/ZnO model catalyst is compared to the pure ZnO powder sample already characterized above. The catalytic performance of the systems was measured by online gas chromatography (i.e., CO formation was detected and quantified). Prior to the catalytic test using a gas feed mixture of H_2/CO_2/He (3/1/6), the samples were reduced in-situ (see experiment section). The results for ZnO and Cu/ZnO are presented in Figure 3.3.6.

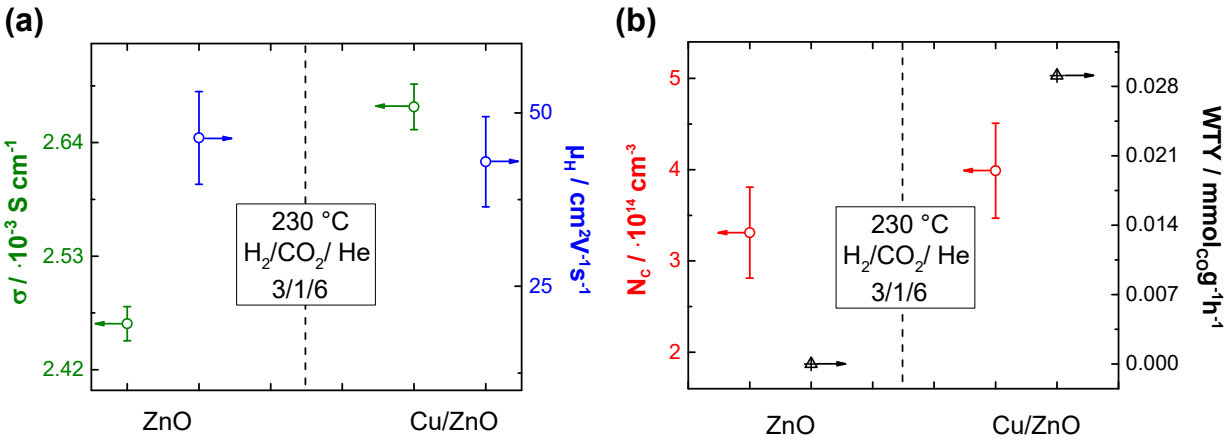

Figure 3.3.6: ***(a)*** *Microwave Hall mobility μ_H (blue), microwave conductivity σ (green), and* ***(b)*** *Calculated absolute charge carrier concentration N_C (red) and simultaneously measured catalytic data (weight time yield (WTY) of CO formation) as a function of ZnO and Cu/ZnO model catalyst.*

The ZnO reference system showed a conductivity σ of 2.46 ± 0.02·10^{-3} S cm^{-1} and a Hall mobility μ_H of 46 ± 7 cm^{2}V^{-1}s^{-1} under the applied conditions. Applying equation 3.7, the absolute charge carrier concentration N_C is 3.3 ± 0.5·10^{14} cm^{-3}. Very little formation of CO was detected in the in-situ experiment for ZnO whereas the Cu/ZnO model catalyst showed a clear increase in the weight time yield (WTY) of CO (cf. Figure 3.3.6b). This increase in CO formation is consistent with literature results since Cu is commonly assumed to be the active component of the catalyst[23,67,214]. The Cu/ZnO model catalyst showed a conductivity σ of 2.67 ± 0.02·10^{-3} S cm^{-1} and a Hall mobility μ_H of 43 ± 7 cm^{2}V^{-1}s^{-1} under reaction conditions. The corresponding charge carrier concentration N_C was 3.9 ± 0.6·10^{14} cm^{-3}.

When comparing to the ZnO reference system under reaction conditions, the Cu/ZnO model catalyst exhibited a higher conductivity and charge carrier concentration. The ZnO

studied under inert atmosphere yielded a lower conductivity. This increase in reaction atmosphere is related to the reducibility of the ZnO resulting in a higher conductivity. This observation is in accordance with Schumann *et al.*, who reported an increasing conductivity in reducing conditions for unpromoted and promoted ZnO[23]. The impregnation with Cu influences the reduction of ZnO to form ZnO_{1-x} which increases the charge carrier concentration due to oxygen vacancy formation. This metal-semiconductor interaction is explained by the so-called strong metal support interaction[114,215]. Under reducing conditions, an overlayer of partially reduced ZnO_x is formed and grows over the more disk-like Cu particles[23,114,216] resulting in an higher conductivity/charge carrier density compared to ZnO under reaction conditions. It seems that the Cu particles show no microwave absorption behavior under reducing conditions which was also found in preliminary experiments with Cu particles on differently promoted ZnO. Only oxidized Cu absorbs microwave radiation and would thus increase the microwave conductivity of the sample. Therefore, Cu does not directly contribute to the measured microwave conductivities and Hall mobilities. The observed changes are, in a first approximation, due to changes in the electronic structure of ZnO but influenced by the interaction with Cu. The conductivity of Cu/ZnO increases with increasing temperature under reducing conditions which is attributed to the changes in the ZnO support.

The results are chemically relevant as the reverse water-gas shift reaction requires activation of CO_2 to CO_2^- for which electrons from the catalysts are needed. These electrons are donated back to the catalysts through oxidation of hydrogen. The catalytic performance of the catalyst can be further increased by introducing promoting agents (e.g., Al^{3+}) which will be part of Chapter 3.4.

3.3.4 Conclusions

Based on the microwave Hall effect and the cavity perturbation technique a contact-free Hall mobility and a conductivity method have been developed for measurements of powder samples under catalytically relevant conditions. The microwave Hall effect system was calibrated using well-known single crystal samples with charge carrier mobilities determined by conventional static Hall effect measurements. With the known calibration constant, microwave Hall mobility values of catalytic powder materials can be obtained. The newly developed in-situ MHE setup consists of a fixed bed reactor geometry inserted into a X-band bimodal TE_{112} cavity. The reactor is connected with an external heater which allows to reach temperatures up to 500 °C. The implemented gas delivery system can supply

various gases. The newly developed MHE setup for contact-free in-situ measurements was successfully tested by studying the temperature dependence for ZnO single crystal and for ZnO powder. Finally, the conductivity and Hall mobility of an active Cu/ZnO model catalyst were determined during a reverse water-gas shift reaction. These measurements offer the possibility to gain new and important insights into the working mode of heterogeneous catalysts.

3.3.5 Outlook

The MHE setup was designed to observe charge transfer and charge transport processes in a working heterogeneous catalyst. To improve the experimental setup further and to address some aspects mentioned in the previous Chapters various changes and adjustments for future measurements are discussed in the following.

To achieve critical coupling conditions the coupling between the waveguide and the bimodal cavity can be improved by an iris slit instead of an iris hole[104]. A reduction of the empty cavity wall signal could be realized by different cavity coatings (for example, the n-type signal of the wall can be reduced by a p-type coating)[217]. A crossed-grid end wall could be another option[112]. This modification would allow investigating Hall mobilities lower than 1 $cm^2V^{-1}s^{-1}$ which is the lower limit suggested by Fletcher[112]. For comparison, a typical low-mobility semiconductor and model oxidation catalyst V_2O_5 exhibits a microwave Hall mobility of 3 - 5 $cm^2V^{-1}s^{-1}$ [28]. In addition, the sensitivity in low-mobility samples can be increased by a superheterodyne receiver or lock-in amplifier as detection units[104]. The sensitivity with the already installed 4-port vector-network analyzer can be improved by the canceling channel which is presented in the next Chapter. Further, the use of the so-called embedded system function where the elements of the canceling channel can be simulated in the network analyzer would reduce unwanted signals due to the additional elements (e.g., coaxial cables, attenuator, and phase shifter). As described before, the conductivity and Hall mobility are connected with the quality factor Q of the bimodal cavity. The determination of Q could be done with a resonant circuit fit model (e.g., Kaifez[108]) compared with the 3 dB method. This procedure is suggested to further implement the coupling coefficient and non-ideal mode coupling.

3.4 Charge Carriers power CO_2 activation: In-situ quantification on Cu/ZnO model catalysts

A quantitative charge carrier analysis and catalytic activity investigations of Cu/ZnO model catalysts have been combined in this Chapter. The promoting effect of Al^{3+} on the ZnO support for CO_2 activation via the reverse water-gas shift reaction has been analyzed in detail. To the best of my knowledge, this is the first time that the contact-free and in-situ microwave Hall effect technique is able to measure charge carriers in Cu/ZnO based model catalysts under reverse water-gas shift reaction conditions. This method allows to analyze the electrical conductivity, charge carrier mobility, and absolute number of charge carriers. An increase in charge carrier concentration with increasing Al^{3+} content as well as its direct correlation with the catalytic activity for CO formation is found. It is concluded that the increased availability of charge carriers plays a key role in CO_2 activation and CO formation which finds additional support in a concurrent decrease of the apparent activation energy and increase in the reaction order of CO_2. In conclusion, these results demonstrate the importance of in-situ measurements of the charge carrier mobility to obtain quantitative charge carrier concentrations in solid heterogeneous catalysts under working conditions.

3.4.1 Introduction

The tremendous quantities of anthropogenic CO_2 that have been released into the atmosphere over the last 200 years have begun to yield noticeable changes to the global climate. Extrapolating into the future, it is clear that continued temperature rises would have dire consequences to life on earth. Strategies are actively being sought to counteract the production of CO_2. One potential route is the conversion of CO_2 into value-added chemicals using energy inputs from renewable resources. This research area is part of the so-called carbon capture and utilization concept for a sustainable future[3,62,63]. Such processes will necessarily rely on efficient catalysts. One industrial heterogeneous catalyst that is already used for CO_2 activation is the $Cu/ZnO/Al_2O_3$ system producing methanol – an important chemical intermediate and alternative fuel – from synthesis gas ($CO/CO_2/H_2$)[67,214,218]. The Cu/ZnO catalyst is also active in the competitive reverse water-gas shift reaction (cf. Scheme 3.1). It is known that the reverse water-gas shift activity over Cu/ZnO-based catalysts is strongly

influenced by small amounts of Al added to the oxide support [23,120,124,216,219]. This cationic Al^{3+} dopant acts as structural and electronic promoter.

$$CO_2 + H_2 \rightleftharpoons CO + H_2O \tag{3.10}$$

Scheme 3.1: *Reverse water-gas shift reaction,* $\Delta H_{298\ K} = 41.2\ kJ\ mol^{-1}$ [64].

In general, two different mechanisms for the water-gas shift and reverse water-gas shift reaction over Cu-based catalysts have been proposed in literature. First, the formate decomposition and redox cycle have been discussed [69–72,220] where the formate, due to its high stability, is often depicted as a spectator [73]. Second, the commonly assumed surface redox mechanism proposes the dissociative CO_2 adsorption as the rate-limiting step [69,71].

Thus, understanding the interaction between the CO_2 molecule and the surface of the catalyst is of fundamental importance. On the basis of theoretical studies, the carbon-oxygen bond is activated by a transfer of electrons from the d-band of the metal into the antibonding orbital of CO_2 to form, e.g., $CO_2^{\delta-}$ [64,221,222]. Since heterogeneous catalysts are often used in a powdered form, the experimental analysis of such charge transfer processes under real operating conditions is challenging. In particular, methods measuring electrical conductivity, carrier mobility, and charge carrier density are very limited. Furthermore, electrical conductivity changes are governed by both the mobility and the concentration of charge carriers. To discriminate between these effects one has to measure not only the electrical conductivity but also the Hall mobility of the charge carriers [24]. Contact-free electrical conductivity measurements under catalytic relevant conditions have been introduced based on the MCPT [15,17,18,20,21]. The contact-free MHE offers one possibility to determine both electrical conductivity and carrier mobility changes. The MHE also yields the number of charge carriers since the conductivity is the product of the Hall mobility and charge carrier concentration [24,25,104]. The experimental setup for MHE measurements utilizes bimodal cavities which exhibit two orthogonal so-called modes which are standing waves at microwave frequencies. The principle of measurement is based on the fact that one of the two modes is excited by an external microwave source while energy is transferred to the orthogonal mode by the Hall effect. The energy transfer is due to the Lorenz force acting on moving charges in the presence of a magnetic field and is related to the Hall mobility of the charge carriers [24,25,104].

Using the above-mentioned MHE method, the influence of Al^{3+} dopants on the charge carriers and catalytic properties of Cu/ZnO model catalysts under reverse water-gas shift reaction conditions have been investigated. A series of Cu/ZnO:Al model catalysts containing different Al^{3+} concentrations were prepared by co-precipitation and subsequent impregnation. The aim is to identify how Al^{3+} modifies the reverse water-gas shift activity and how the collective electronic properties of these Cu/ZnO model series change. The catalyst support and model catalyst series have been thoroughly analyzed by additional techniques, powder XRD, X-ray fluorescence spectroscopy (XRF), and N_2-physisorption, for the catalyst supports and model catalysts in a precursor state. The apparent Cu surface area was quantified by N_2O-reactive frontal chromatography. The recently developed in-situ MHE setup (cf. Chapter 3.3) was used for microwave conductivity and Hall mobility measurements under 1 H_2/ 1 CO_2/ 8 N_2 feed at ambient pressure and 230 °C. In an additional reverse water-gas shift experiment, the kinetic behavior of Cu/ZnO:Al model catalysts were investigated to obtain the apparent activation energy and reaction order of H_2 and CO_2. Finally, the catalytic data were correlated with the electronic properties.

3.4.2 Experiment

Samples

The model catalysts were prepared as described in detail in Appendix D. Briefly, ZnO catalyst supports were prepared by pH-controlled co-precipitation [23,133]. The Al^{3+} promotion was varied (nominal 0 - 4 mol%) and the bare supports were calcined at 330 °C to yield nano-crystalline ZnO. In a subsequent step the samples were impregnated with Cu citrate for a nominal Cu loading of 10 wt%.

Characterization methods

Powder XRD measurements were performed in Bragg-Brentano geometry on a Bruker AXS D8 Advance II theta/theta diffractometer with Ni filtered Cu Kα radiation and a position sensitive energy dispersive LynxEye silicon strip detector. The sample powder was filled into the recess of a cup-shaped sample holder, the surface of the powder bed being flush with the sample holder edge (front loading). Both the ZnO supports and the CuO/ZnO:Al precursors were analyzed. A detailed description of the pattern fitting is given in Appendix D.

XRF was performed in a Bruker S4 Pioneer X-ray spectrometer.

Nitrogen-physisorption measurements were performed in a Quantachrome Autosorb-1 machine. Prior to the analysis, the samples were degassed for 2 h at 100 °C. The Brunauer-Emmett-Teller method was applied to determine the surface area of the catalyst supports and model catalysts.

Conductivity and Hall mobility measurements were performed with the MCPT and the MHE approach. The newly developed in-situ MHE setup and the measurement principle are described in Chapter 3.3. It extends previous work of Chapter 3.3 by including a canceling channel in the experimental setup, c.f. Figure 2.2.3a in Chapter 2.2.3. Prior to the MHE experiment the samples were reduced in-situ for 90 min at 250 °C with a heating rate of 2 °C/min in the presence of 10 vol% H_2 and 90 vol% He. Afterward, the temperature was decreased to 230 °C and the Cu/ZnO:Al catalysts were investigated in 10 vol% H_2 / 10 vol% CO_2 / 80 vol% Ar. The CO formation was analyzed by an online micro gas chromatograph (Varian CP-4900, equipped with PoraPLOT and COx columns). After reaching steady state values, the electronic properties were measured. The effective electrical conductivity σ was calculated according to equation 2.16 of Chapter 2.2. The effective microwave Hall mobility μ_H was derived from equation 3.8 of Chapter 3.3.3. Finally, the charge carrier concentration N_C was obtained (cf. equation 3.7 of Chapter 3.3.2)[24]. The averaged values of σ, μ_H, and N_C are given and the error is calculated according to the maximum error of all combined measured quantities (equation 4.28 of Appendix C). Further information can be found in Appendix D.

N_2O-chemisorption capacities and apparent Cu^0 surface areas (Cu-SA_{N_2O}) were determined by N_2O-reactive frontal chromatography (RFC)[223]. The decomposition of N_2O at the surface of Cu occurs according to: $N_2O + 2Cu \rightarrow Cu_2O + N_2$[223]. Prior to the RFC measurement with a total flow of 10 ml/min and a 1 % N_2O in He mixture, the catalyst was reduced in-situ as mentioned above. A sieved catalyst (100 - 200 μm) with a mass of 200 mg was investigated. The mass spectrometer signal at m/z = 28 (N_2) was used to determine the N_2O-capacity and for a Cu-SA_{N_2O} quantification assuming a stoichiometric reaction. According to literature, the intersection between the decreasing N_2 signal and increasing N_2O signal at the breakthrough point was used as a limit for the integration of the N_2 signal[224].

The reverse water-gas shift activity measurements were performed in a fixed bed flow-through reactor with an inner diameter of 6 mm (ex-situ experiment in an automated reactor setup, ILS-Integrated Lab Solutions GmbH, Berlin) where the reactor tubes were setup in units of eight (8-fold parallel reactor setup). The temperature of each reactor tube

was controlled by a thermocouple (Type K) placed in the reactor bed. The catalyst (50 mg, 100 - 200 μm sieve fraction) was diluted with SiC (3 g) to prevent hot spot formation and to improve heat transport. Prior to the reverse water-gas shift activity measurements, the samples were reduced in 10 vol% H_2 / 90 vol% N_2 (10 ml/min total flow) with a heating ramp of 2 °C/min from room temperature to 250 °C and a dwell time of 90 min. Then, the temperature was reduced to 230 °C and the 1 H_2 / 1 CO_2 / 8 N_2 feed was applied. The CO formation was analyzed by an online gas chromatograph (7890A Agilent, equipped with Plot-Q and Plot-MoleSieve 5A columns connected to a thermal conductivity detector and FFAP and Plot-Q columns connected to a flame ionization detector).

3.4.3 Results and discussion

The focus within this Chapter is to report the influence of Al^{3+} dopants on the absolute charge carrier concentration and catalytic properties of Cu/ZnO model catalysts under reverse water-gas shift reaction conditions. Prior to the electronic properties analysis, the impact of the accompanied structural properties is discussed to evaluate the origin of the modified catalytic performance.

Sample characterization

The elemental composition (Al, Zn, and Cu) of the samples were analyzed by XRF. The measured Al content for all samples were slightly less than the nominal values, c.f. Table 3.2. In the following, it is referred to the experimental Al values given in wt%. The Cu loadings after impregnation and calcination were identical for all samples (12 wt% CuO, cf. Table 3.2).

By way of example, Figure 3.4.1a illustrates a full powder XRD pattern of ZnO:Al (1.7 wt% Al) together with a Rietveld analysis. The theoretical Rietveld fit of ZnO (red line), which is the only detectable phase, agrees perfectly with the experiment (black circles). Only tiny deviations in the difference curve (blue line) are detected. The full ZnO:Al sample series is presented in Figure D.1a of Appendix D. The full pattern analysis and Rietveld analysis of the impregnated and calcined CuO/ZnO:Al (1.7 wt% Al) model catalyst are shown in in Figure D.2a of Appendix D, where the CuO(111) reflection at 38.6° = 2θ is pronounced. The diffraction patterns of all other CuO/ZnO:Al samples are also provided in the Appendix D (cf. Figure D.1b).

Table 3.2: *Chemical composition of Al, Zn, and CuO determined by XRF, and BET surface areas of pure ZnO:Al supports and CuO/ZnO:Al model catalysts.*

ZnO:Al supports						
Al nominal value / *mol%*	4	3	1	0.5	0.1	0
FHI-ID	25147	25110	25131	25138	25145	25445
Al / *wt%*	1.1	1.7	0.6	0.3	0.1	0
Zn / *wt%*	98.9	98.3	99.4	99.7	99.9	100
BET-SA / m^2g^{-1}	85	84	68	54	59	50
CuO/ZnO:Al model catalysts						
FHI-ID	25398	25397	25396	25395	25394	25651
Al / *wt%*	0.8	1.3	0.4	0.1	0	0
Zn / *wt%*	86.7	86.1	87.3	87.5	87.4	87.9
Cu (CuO) / *wt%*	12.5	12.6	12.4	12.4	12.6	12.1
BET-SA / m^2g^{-1}	42	41	40	36	34	34

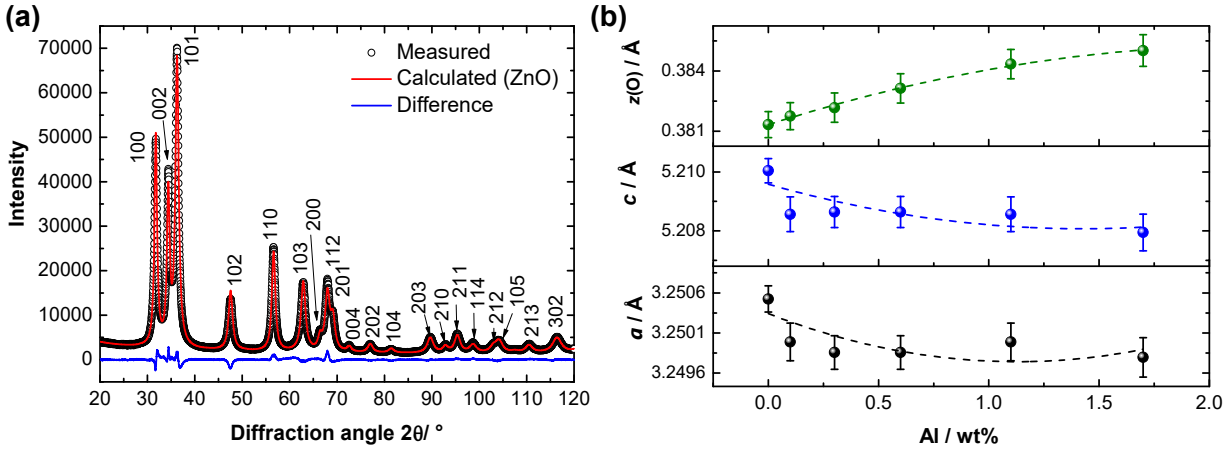

Figure 3.4.1: ***(a)*** *Rietveld fit of ZnO:Al (1.7 wt% Al) with the measured (black circles), calculated (red line) diffraction patterns, the corresponding difference curve (blue line) and* ***(b)*** *Lattice parameters a, and c, and atomic coordinate z of oxygen from the Rietveld refinements as a function of Al content determined by XRF.*

Overall the powder XRD analysis indicates no formation of crystalline minor by-phases. Therefore, it is concluded that Al is incorporated into the ZnO lattice and occupies the

tetrahedral sites in the ZnO structure[23,120]. As shown in Figure 3.4.1b, this incorporation leads to a contraction of the ZnO unit cell since Al^{3+} (0.39 Å)[141] has a smaller effective ionic radius than Zn^{2+} (0.6 Å)[141]. The hexagonal unit cell of ZnO has two lattice parameters a and c which are analyzed in more detail. The refinement analysis yields a decrease in a (0.0007 Å), a decrease in c (0.002 Å), and an increase in the atomic coordinate z of oxygen (0.004 Å) with increasing Al content. The coherently scattering domain sizes extracted from Rietveld fitting results show a decrease for ZnO ranging from 11 to 18 nm (14 - 20 nm for impregnated and calcined samples, cf. Table D.4 of Appendix D) with increasing Al content. From nitrogen-physisorption experiments, the specific BET-SA are gained (cf. Table 3.2). The BET-SA of ZnO:Al increases from 50 to 84 m^2g^{-1} with increasing Al content (and from 34 to 42 m^2g^{-1} for CuO/ZnO:Al). This trend matches perfectly with the domain sizes from powder XRD analysis where the unpromoted ZnO sample shows the largest crystallite size and the lowest BET-SA. Whereas the highest promoted ZnO:Al (1.7 wt%) sample shows the smallest crystallite size and the highest BET-SA. The same trends are observable for the impregnated and calcined CuO/ZnO:Al model catalysts (cf. Table 3.2 and Table D.4 of Appendix D).

Table 3.3: *Al content determined by XRF, N_2O capacity, and corresponding Cu-SA_{N_2O} of the Cu/ZnO:Al model catalysts after reduction.*

Cu/ZnO:Al model catalysts						
Al / *wt%*	1.7	1.1	0.6	0.3	0.1	0
N_2O capacity* / *$\mu mol\ g^{-1}$	64	69	70	78	79	84
$Cu - SA_{N_2O}$ / *m^2g^{-1}	5.2	5.6	5.8	6.4	6.5	6.9

Using N_2O-reactive frontal chromatography, apparent Cu^0 surface areas (Cu-SA_{N_2O}) between 5.2 m^2g^{-1} and 6.9 m^2g^{-1} were determined (calculated from the N_2O capacities, cf. Table 3.3). The highest promoted Cu/ZnO:Al model catalyst (1.7 wt% Al) had the lowest Cu-SA_{N_2O} (5.2 m^2g^{-1}) while the unpromoted Cu/ZnO model catalyst yielded a Cu-SA_{N_2O} of 6.9 m^2g^{-1}. As a consequence of the powder XRD and BET-SA results discussed before, the Cu-SA_{N_2O} for Al promoted Cu/ZnO should increase with increasing Al content due to smaller crystallite sizes and higher surface areas. However, despite the identical Cu loading of the samples (XRD 10 wt% and XRF 12 wt% after calcination) these findings show a decreasing trend with increasing Al content in N_2O-chemisorption capacity (and Cu-SA_{N_2O}). To monitor the state of the Cu-moieties after reduction, the Cu domain sizes

of the unpromoted Cu/ZnO and the highest promoted Cu/ZnO:Al (1.7 wt% Al) were investigated with in-situ powder XRD at 250 °C under hydrogen atmosphere (5 vol% H_2 in Ar). For the unpromoted Cu/ZnO sample, 9.6 ± 0.3 wt% Cu-metal with a domain size of 6.3 nm is measured. The model catalyst with 1.7 wt% Al incorporated into ZnO shows 10.6 ± 0.3 wt% Cu-metal and domain sizes of 5.7 nm (cf. Table D.5 of Appendix D). Therefore, also in the reduced state, the promoted sample exhibits a smaller domain size and a slightly higher Cu-moiety which should result in a higher Cu-SA_{N_2O} if the surface is accessible. This can be understood in terms of a change in the so-called strong metal support interaction (SMSI). The SMSI between Cu and ZnO has been explained by spreading of the metallic Cu particles over the support with their surfaces covered by Zn species[114,215]. For methanol synthesis, the promotional effect of ZnO as part of the industrial $Cu/ZnO/Al_2O_3$ catalyst is partly attributed to the reducibility of the ZnO support (oxygen defects)[67,225,226]. An amorphous overlayer of partially reduced ZnO_x is formed and grows over the Cu particles[216] which in turn influences the Cu adsorption behavior probed by N_2O[224]. Hence, the N_2O-chemisorption capacity is more complex and attributed to both Cu surface and oxygen defects at the Cu-ZnO interface[224,227]. Here, a similar behavior was found suggesting that the reducibility of ZnO support is increased with increasing Al content which leads to wetting of the Cu particle. Due to the migration of ZnO_x species to the Cu surface, the N_2O-chemisorption capacity decreased while i.e., smaller fraction of exposed Cu^0 surface areas are available for the reaction with N_2O.

In-situ electronic properties and corresponding reverse water-gas shift reaction activity

Herein, the influence of Al^{3+} is identified on the absolute charge carrier concentration N_C in Cu/ZnO and its effect on CO_2 activation and CO formation. Prior to the charge carrier investigations, the impregnated samples were reduced and activated. Subsequently, electrical conductivity σ and Hall mobility μ_H experiments were performed for all Cu/ZnO:Al catalysts under reverse water-gas shift reaction conditions. The results in Figure 3.4.2 (normalized to Cu/ZnO) show an increase in σ and a slight reduction of μ_H with increasing Al content. The conductivity increased rapidly for 0 - 0.6 wt% Al whereas it seems to reach a plateau for 1.1 and 1.7 wt% Al content. The mobility decreased slightly for the first three Cu/ZnO catalysts (0 - 0.3 wt% Al) and similar values were observed for the last three model catalysts (0.6 - 1.7 wt% Al).

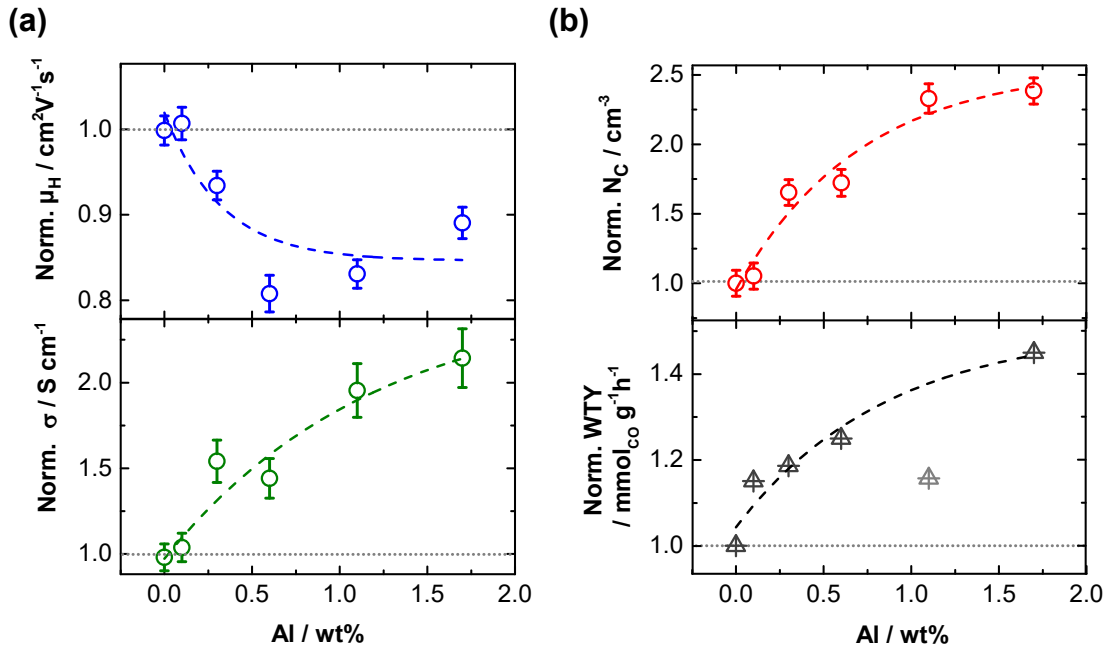

Figure 3.4.2: *Normalized (to Cu/ZnO)* ***(a)*** *Microwave Hall mobility μ_H (blue) and microwave conductivity σ (green) as a function of the Al content which was determined by XRF, and* ***(b)*** *Calculated absolute charge carrier concentration N_C (red) and weight time yield (WTY) of CO formation under reaction conditions (1 H_2/ 1 CO_2/ 8 N_2 at 230 °C). The gray highlighted sample disagrees from the trend line.*

It is known that electrons are the majority type of charge carriers in ZnO due to oxygen vacancies and zinc interstitials[117]. As discussed above, Al in the formal oxidation state +3 is incorporated into the ZnO lattice as shown by powder XRD. This leads to changes in the unit cell and the formation of shallow donor states in the ZnO band gap (additional partially unoccupied energy levels near the lower conduction band edge). The n-type doping increases the absolute conductivity (free charge carrier density) in the conduction band due to this additional donor levels. Electron paramagnetic resonance studies have confirmed the formation of shallow donor states in ZnO with Al[23,228]. Since microwaves penetrate through the sample, bulk electronic properties were probed (here, given by effective values for the powders)[15,24,39]. From these observations, it is concluded that Al acts as strong electronic promoter for ZnO given by the distinct increase in electronic bulk conductivity. The mobility is related to the scattering time according to, $\mu = (q\langle\tau\rangle)/m^*$, where q is the electronic charge, $\langle\tau\rangle$ is the relaxation time averaged over the distribution of electrons, and m^* is the effective electron mass[110]. Therefore, the decreasing carrier mobility can be explained by a reduction of the scattering time due to higher promotion with Al[117].

In Figure 3.4.2b, a pronounced increase in the charge carrier concentration N_C was calculated (cf. equation 3.7 of Chapter 3.3.2) which strongly supports the explanation that the change in conductivity σ is related to an increase of the electron density. The charge carrier concentration N_C increases by almost 50 % and overcompensates the slightly reduced μ_H which decreases by about 15 % between 0 and 1.7 wt% Al, c.f. Figure 3.4.2b. In order to allow a reliable comparison between the modified electronic properties and the catalytic activity, CO formation was monitored simultaneously revealing a change in the WTY for CO. The WTY increases strongly by i.e., 40 % for the highly promoted catalyst (1.7 wt% Al) compared with the unpromoted Cu/ZnO catalyst which agrees with literature[23,120]. In this context, a direct correlation between N_C and the WTY for CO can be drawn since with increasing N_C a comparable increase in CO formation was observed. These findings give strong experimental evidence of a direct influence of the N_C on the CO_2 activation and finally the reverse water-gas shift activity.

Activity in reverse water-gas shift reaction

The activity in the reverse water-gas shift reaction was additionally measured ex-situ in a tube bundle reactor setup. The catalysts were tested at different temperatures and H_2/CO_2 ratios to obtain the apparent activation energy (app. E_a) and the reaction order of H_2 and CO_2, respectively. The app. E_a values for CO formation were obtained from Arrhenius plots (cf. Figure D.4 of Appendix D).

The same activity trend for CO formation was found as in the in-situ MHE experiment, from less to high activity of Cu/ZnO:Al: 0 wt% < 0.1 wt% < 0.3 wt% < 0.6 wt% < 1.7 wt% Al (except the outlier 1.1 wt% Al). The deviation of the so-called outlier model catalyst might be attributed to a different electronic structure same deviation in the electronic structure as seen in powder XRD, and BET-SA. Obviously, the 4 mol% Al doping was not successful which needs to be repeated for further analysis to confirm the deviation from the trend line. A comparison between relative ex-situ and in-situ reverse water-gas shift activity is shown in Figure D.5 of Appendix D. From this linear relationship, it is concluded that a comparison between the in-situ electronic properties and catalytic activity can be made and it further underlines the applicability of the microwave absorption setup as reactor.

Figure 3.4.3a depicts the E_a results as a function of the Al content. The E_a value decreases from 97 ± 3 kJ mol^{-1} for the unpromoted Cu/ZnO to 87 ± 6 kJ mol^{-1} for the promoted Cu/ZnO:Al (1.7 wt% Al). The same difference in the E_a value has been found by Schumann *et al.* (Cu/ZnO 99 kJ mol^{-1}, and Cu/ZnO:Al 87 kJ mol^{-1})[23]. Furthermore,

Dutta *et al.* reported forward activation barriers for the CO_2 activation on Al promoted ZnO of 87 kJ mol^{-1} which is consistent with the present measurements[229]. This indicates that Al^{3+} influences the nature of the active site for the reverse water-gas shift reaction positively resulting in a lower activation barrier of the rate-determining step.

A reaction order for H_2 of ≈ 0.15 was found while the reaction order of CO_2 increased from 0.25 to 0.36 with increasing amount of Al content (cf. Figure 3.4.3a and Table D.6 of Appendix D). These reaction orders agree well with those of similar Cu/ZnO based catalyst studies[23,71,77] and indicate that the activation of CO_2 is directly involved in the rate-determining step for the reverse water-gas shift reaction.

Based on concepts from solid state physics, the Cu/ZnO system represents a metal/semiconductor junction (or Schottky-Mott junction) which forms a Schottky barrier. Frost[74] suggested, that electrons are transferred via this junction where the direction of charge transfer between Cu and ZnO is still not completely understood[75,76]. It is known, that this Cu/ZnO (or in general metal/semiconductor[230]) interface plays an important role as an active catalytic site in the reverse water-gas shift reaction[77]. Therefore, the increase in CO formation for the presented system is explained by a charge transfer presumably from the metal-oxide interface to the lowest occupied $2\pi_u$ anti-bonding orbital of CO_2[222]. This charge transfer would lead to a bending of the linear CO_2 molecule and to form an anionic CO_2^- species[64,222,231]. This activated, meta-stable CO_2^- species would then be further transformed into a surface intermediate (e.g., carboxylate, formate or carbonate)[64] which acts as a precursor to CO formation. The relevance of the Cu-ZnO interface was already reported for methanol synthesis, where oxophilic $Zn^{\delta+}$ sites from $Zn^{\delta+}O_x$-covered Cu particles are suggested as adsorption sites for CO_2[224].

Further, Schwab reported an increasing E_a value with increasing conductivity for formic acid dehydration over Ni/Al_2O_3[230]. Figure 3.4.3b shows a direct correlation between the apparent activation energy E_a and the absolute charge carrier concentration N_C (related to the conductivity as explained before). In contrast to Schwab's results, a decreasing E_a value is found with increasing N_C and increasing CO formation. These experimental results point again to a positive effect of Al on the nature of the active sites for the reverse water-gas shift reaction resulting in a lowered E_a, an increased N_C, and an increased catalytic activity. Hence, it is concluded that the charge carriers of the catalyst participate in the CO_2 activation process, schematically summarized in Figure 3.4.4. Here, the assumption of downward band bending was made due to different work functions of Cu and ZnO. The work function Φ of Cu ($\Phi = 4.9$ eV) is smaller than ZnO ($\Phi = 5.3$ eV) as reported by

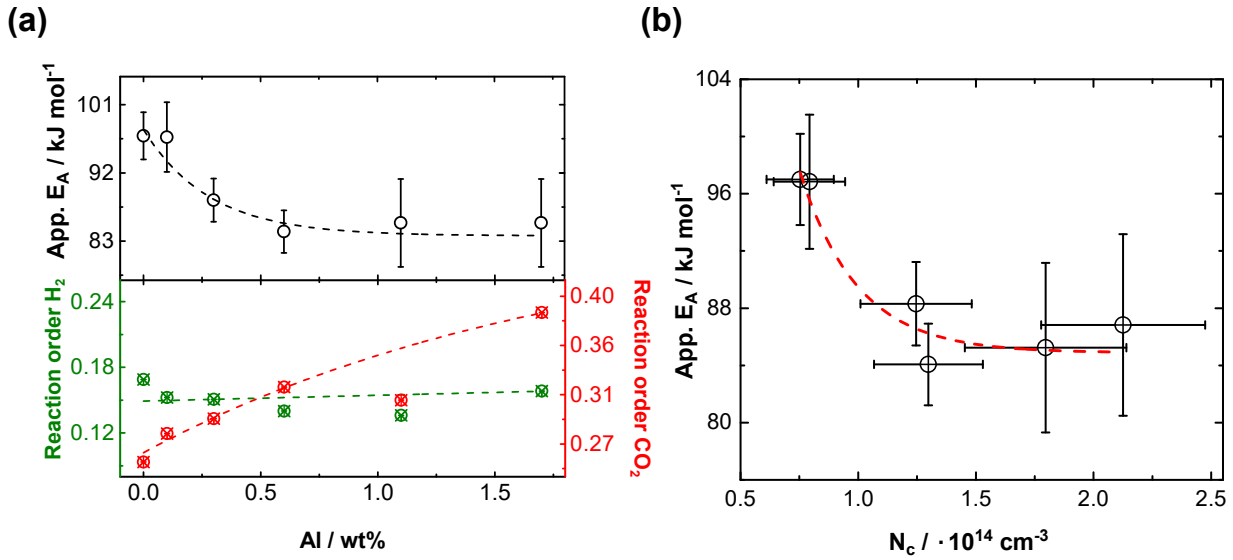

Figure 3.4.3: ***(a)*** *The apparent activation energy E_a of CO formation, the reaction order of H_2 and CO_2 as function of the Al content, and* ***(b)*** *The apparent activation energy E_a as a function of the absolute charge carrier concentration N_C. The dashed lines are drawn to guide the eye.*

Sheini *et al.*[76]. The increase in the reducibility of ZnO due to the incorporation of Al leads to partially covered Cu particles (lower Cu-SA_{N_2O}) and a higher Cu/ZnO interface. Due to this increased metal/semiconductor interface the number of available sites for CO_2 activation via electron transfer increases. As a consequence, these findings give strong experimental indications for a correlation between the availability of charge carriers and an increase in the CO formation as well as the CO_2 activation as part of the critical step in the reverse water-gas shift reaction. Finally, for this Cu/ZnO:Al doping series it should be noted that in addition to a modification of the electronic structure (increase in free charge carriers) a change of the morphology and surface properties is also observed. Thus, the contribution of the structural part has to be considered as well. But due to the fact that the structural and surface variations point in the opposite direction in terms of the available BET-SA, Cu-SA_{N_2O} and domain sizes of ZnO and Cu-metal. It can be stated that the electronic modifications overcompensate clearly the structural ones and as a consequence the observed trends in reverse water-gas shift activity are strongly coupled to the electronic properties.

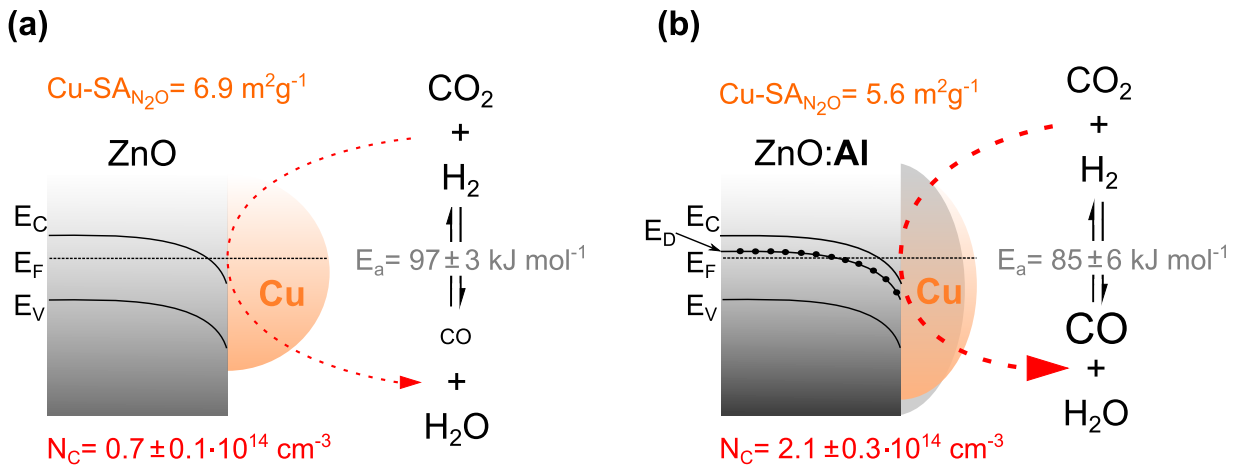

Figure 3.4.4: *Simplified sketch illustrating the charge transfer process (red line) for CO_2 activation over* ***(a)*** *Unpromoted Cu/ZnO and* ***(b)*** *Promoted Cu/ZnO:Al based model catalysts. The reverse water-gas shift reaction is shown and E_C is the conduction band, E_F is the Fermi level, E_D is the additional donor level, E_V is the valence band, E_a is the apparent activation energy, and N_C is the absolute charge carrier concentration.*

3.4.4 Conclusions

The in-situ microwave Hall effect experiments on a series of Al-doped Cu/ZnO model catalysts demonstrate a correlation between the charge carrier concentration and the activity in reverse water-gas shift and CO_2 activation, respectively. The increased availability of free charge carriers introduced by the trivalent dopant Al enhances charge transfer under catalytically relevant conditions. This finding provides experimental evidence of the importance of charge transfer and charge transport in catalysis research and implies that electronic properties are decisive descriptors for understanding and explaining catalytic properties. This new methodology based on the microwave Hall effect opens the way towards studies yielding a fundamental understanding of other materials and heterogeneously catalyzed reactions.

4 Summary and final conclusions

The development of in-situ techniques has increased in recent years in the quest of examining details of the active state of heterogeneous catalysts. However, only few techniques allow the simultaneous measurement of catalytic performance and electronic properties of the catalyst under working conditions. Since heterogeneous catalysts are typically powders, the use of non-contact techniques is essential. Therefore, the focus of the present work is the implementation of in-situ and contact-free methods to measure charge transport and related parameters of heterogeneous catalysts in a reaction environment. The methods are based on microwave cavity perturbation and microwave Hall effect techniques enabling a detailed view of the microwave conductivity, of the microwave Hall mobility, and of the absolute charge carrier concentration.

The first part of this thesis describes the development of an in-situ microwave conductivity apparatus using cylindrical TM_{0n0} ($n = 1, 2$) cavities. Here, the dynamic charge carrier response in unpromoted and differently promoted (Ga, Al, Mg) ZnO to reducing and oxidizing gas feeds serves as a first application. Under reducing conditions the conductivity is found to increase while applying oxidizing conditions decreases the conductivity, identifying ZnO as a n-type semiconductor. Added impurities into the ZnO of wurtzite structure, which are prepared by co-precipitation, influence the electrical behavior. Al and Ga increase, but Mg decreases the initial intrinsic n-type conductivity of ZnO. In addition, the change in electrical conductivity by reducing and oxidizing feed proves that electrons are the major (free) charge carriers under reaction conditions. The gas-phase-dependent microwave conductivity changes are consistent with reference experiments using a contact technique. To further elucidate the nature of charge carriers multi-frequency and temperature-dependent conductivity measurements are carried out and reveal the dominating contribution of free charge carriers at higher (reaction) temperature. These findings are corroborated by time-domain THz spectroscopy measurements.

In a subsequent study, the industrial oxidation catalyst vanadyl pyrophosphate is investigated under dry and wet propane feed. The presence of steam leads to an increase

in selectivity towards the selective oxidation products (acrylic acid, propylene). This is accompanied by a lowered conductivity and decreased work function whereas no shift of the valence band edge is observed. Complementary XP core level analysis show that the VPP surface is irreversibly depleted in phosphorous which is combined with an increased average vanadium oxidation state when adding steam to the propane feed. The loss of phosphorus changes the acceptor level which leads to a modified surface dipole and, hence, to a decreased work function. In addition, an electronically different V^{5+} peak in the XP spectrum at a binding energy of 517.8 eV is observed and increases in the presence of steam. Hence, steam leads to a chemically changed VPP catalyst and explains the incomplete reversibility of the conductivity behavior. At a microscopic level, the electrical conductivity is governed by the mobility and the concentration of charge carriers. A modification of the charge carrier concentration by steam in the subsequent treatment seems unlikely since no changes in a reference experiment without propane were found. This is consistent with the unaffected XP valence band edge position and with the V3d pre-edge states. Therefore, a variation in the charge carrier mobility is discussed as the origin of the decreasing conductivity with steam.

The second part of this thesis describes in-situ microwave Hall effect measurements on different catalysts. The microwave Hall effect allows the simultaneous measurement of microwave conductivity and microwave Hall mobility. Here, the design and tuning procedures of the bimodal in-situ TE_{112} cavity are described in detail. The calibration of the in-situ setup is performed with well-known single crystals (n- and p-type Si and Ge as well as ZnO) to obtain Hall mobility values of the catalytic powder materials under consideration. Temperature-dependent conductivity and Hall mobility measurements for a reference ZnO single crystal are used to test the sensitivity of the bulk electrical properties with respect to temperature changes. The sensitivity allows also the analysis of polycrystalline ZnO in a flow-through reactor relevant for catalysis. A corresponding case study, where ZnO and Cu/ZnO model catalysts are tested for the reverse water-gas shift reaction, demonstrates the applicability of in-situ measurements.

In subsequent experiments, the role of Al as a promoting agent on the ZnO support for CO_2 activation via reverse water-gas shift reaction is examined using Cu/ZnO model catalysts of varying Al content. ZnO is found to be influenced strongly by increasing its Al content which leads, on the one hand, to smaller domain sizes and to larger surface areas and, on the other hand, to an increased conductivity. The electronic structure changes can be explained by an increased charge carrier concentration which overcompensate the slightly

reduced carrier mobility. A comparison with the activity measurements reveals a correlation between the increase in charge carriers and the amount of CO formation. This suggests that the increased availability of charge carriers plays a key role in the CO_2 activation and CO formation. Additional support is provided by the concurrent decrease of the apparent activation energy and by an increased reaction order of CO_2. The N_2O capacity is found to decrease with increasing Al content which points to a change in the strong metal support (Cu-ZnO) interaction. The increased availability of free charge carriers introduced by the trivalent dopant Al enhances charge transfer under catalytically relevant conditions. This illustrates the relevance of electron transfer in this interfacial region with respect to CO_2 activation and implies that electronic properties are decisive descriptors for understanding and explaining catalytic properties.

In conclusion, the present work can contribute to a better understanding of charge transfer processes in heterogeneous catalysts under realistic working conditions. This thesis shows the fundamental need of in-situ and contact-free microwave absorption methods to understand the underlying charge transport and charge transfer mechanisms. The knowledge obtained in the interrelation between catalytic and electronic properties may be used to design and synthesize novel catalysts for efficient selective oxidation reactions or for CO_2 activation processes. An interesting extension to the in-situ microwave Hall effect experiments performed during this thesis would be to further investigate the influence of steam in selective oxidation reactions. The idea of constant charge carrier density can be proven by in-situ microwave Hall effect measurements. From these investigations, the importance of constant charge carrier mobility could be further determined and may shed some light on the selectivity of transition metal oxide catalysts. Furthermore, the in-situ microwave Hall effect could be applied to various other metal/semiconductor systems (for example Ni/ZnO for methanation of CO_2) to confirm the role of charge carriers and charge transport in heterogeneous catalysis.

Appendix

A Supporting information of Chapter 3.1

Content:

- Sample preparation and characterization

- Multi-frequency microwave cavity perturbation setup

- Conductivity (complex permittivity) measurements using THz spectroscopy

Sample preparation and characterization

The samples ZnO and ZnO:M with 3 mol% doping (M = Al, Ga, and Mg) were prepared by co-precipitation. The precursor solutions contained a mixed Zn- and M-nitrate solution and a base (Na_2CO_3) were added simultaneously into a reactor. An automated reactor (Labmax from Mettler-Toledo) was used to keep the pH (6.5) and temperature (115 °C) constant during the precipitation process. The precipitate $(Zn)_5(CO_3)_2(OH)_6$ was subsequently aged, washed, spray-dried, and calcined at 230 °C (with a heating rate of 2 °C/min) for 180 min[23].

Table A.1: *Brunauer-Emmett-Teller surface areas (BET-SA), and XRD crystallite sizes (L_{Vol}-IB in c-direction as determined form Rietveld fit) of all ZnO:M catalyst supports.*

	ZnO	**ZnO:Al**	**ZnO:Ga**	**ZnO:Mg**
FHI-ID	19390	19364	19351	19340
BET-SA / m^2g^{-1}	38	63	66	50
Crystallite size ZnO/ nm	13	9	8	12

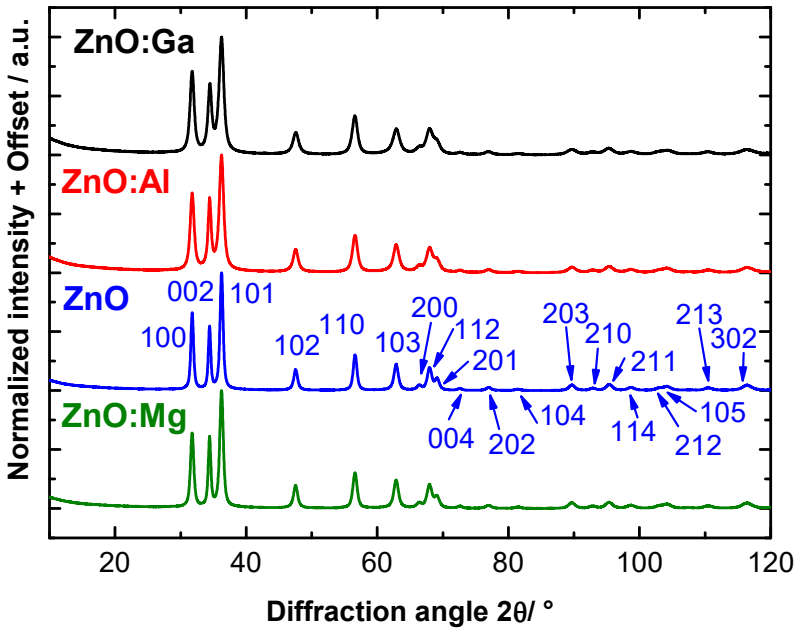

Figure A.1: *Powder XRD patterns of polycrystalline ZnO:M samples and characteristic reflections are shown for pure ZnO, exemplary.*

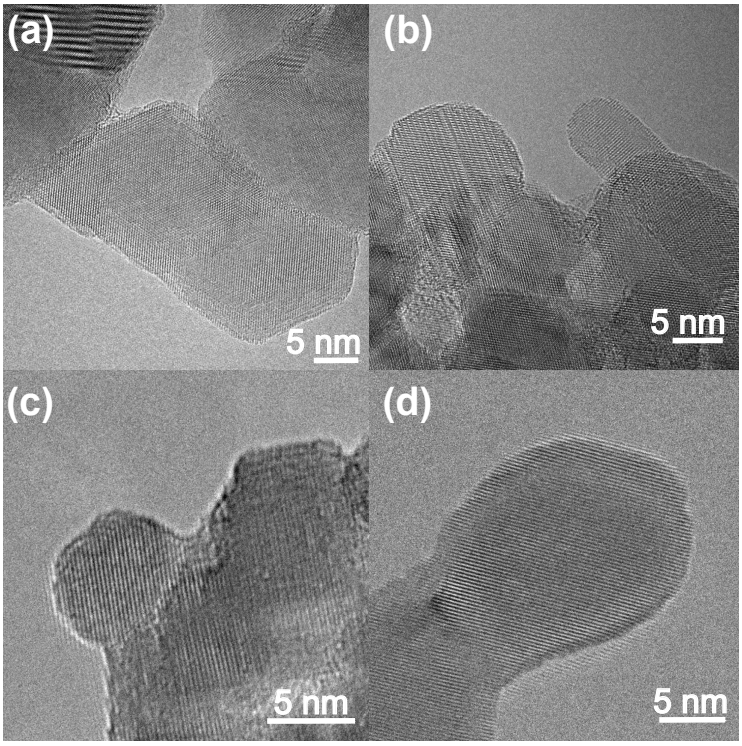

Figure A.2: *High resolution TEM images of* ***(a)*** *ZnO,* ***(b)*** *ZnO:Ga,* ***(c)*** *ZnO:Al, and* ***(d)*** *ZnO:Mg.*

Multi-frequency microwave cavity perturbation setup

The cylindrical form of the TM_{0n0} ($n = 1, 2$) cavity was used. The first (TM_{010}) and second mode (TM_{020}) of this transverse magnetic (TM) field were investigated. As discussed in Chapter 2.1.1, the electric field inside a TM_{mnp} (with $m = 0$, $p = 0$) cavity has a radial E_r, an angular E_ϕ, and a longitudinal component E_z (cf. equation 2.1). From this follows that the electric field distribution has one electric field maximum in the center of the cavity. The sample is located in this maximum, see Figure 2.1.2b. For the TM_{0n0} mode only the longitudinal component is important and depends on the cavity diameter, see Chapter 2.1.1 and equation 2.2. Thus, the cavity diameter was decreased and Table A.2 shows a summary of the invested cavities. The letter (L, S, C, and J) comes from the electromagnetic spectrum. These cavities were calibrated with known single-crystal and powder reference materials using the reported procedure[15]. As a result, the calibration constant A was 1.72 ± 0.17 for the TM_{010} and 3.94 ± 0.68 for the TM_{020} mode. These values are in good agreement with a large body of literature[24,232,233]. Another option is the theoretical calculation which is shown exemplary in equation 4.26 of Appendix C for a TE_{112} mode. For TM_{0n0}, the cavity constant B is $2A$[24,232,233].

Table A.2: *TM_{0n0} cavities with different inner radius (R) and corresponding resonance frequency (f_1) for the TM_{010} mode and resonance frequency (f_2) for the TM_{020} mode.*

TM_{0n0} cavity	**L-band**	**S-band**	**C-band**	**J-band**
R / mm	41	34	22.5	15
f_1 / GHz	1	3	5	7
f_2 / GHz	3	7	11	17

Conductivity (complex permittivity) measurements using THz spectroscopy

Ultra-fast and contact-free THz spectroscopy was performed on polycrystalline ZnO:Ga. The complex permittivity can be obtained from the THz transmission experiment. The THz radiation of the sample $E_{Sample}(t)$ and the N_2 reference $E_0(t)$ are measured and Fourier-

transformed with respect to t. The complex spectrum of the sample pulse $E_{Sample}(\omega)$ and the reference spectrum $E_0(\omega)$ are connected through the following function

$$\frac{E_{Sample}(\omega)}{E_0(\omega)} = t_{12}t_{21}Re^{iL(k-k_0)} \tag{4.1}$$

where $R = 1/(1 + r_{12}r_{21}e^{2ikL})$ accounts for all multiple reflections at the interfaces between N_2 ($i = 1$) and sample ($i = 2$); t_{ij} and r_{ij} are Frensel transmission and reflection coefficients, L is the sample thickness, and $k(\omega) = n(\omega/c)$ is the wave vector of the THz wave. The frequency-dependent refractive index $n(\omega)$ is related to the permittivity of the sample, $\varepsilon(\omega) = n^2(\omega)$. Once the complex refractive index is obtained, the complex permittivity (conductivity) of the sample is

$$\varepsilon(\omega) = \varepsilon_{DC} + \frac{i\sigma(\omega)}{\omega\varepsilon_0} \tag{4.2}$$

where ε_{DC} is a low-frequency permittivity constant. A ZnO single crystal was measured as reference in both setups (MCPT and THz-TDS) at 23 °C. As a result, the real part was about 8 and the imaginary part of the complex permittivity increased with increasing frequency.

The polycrystalline ZnO:Ga sample was analyzed with frequency-dependent MCPT and THz spectroscopy. For this comparison all powder values were transformed into bulk values using the effective medium theory. The complex permittivity of the powder sample ε_p was converted into the complex permittivity of the solid sample ε_s using the Landau-Liftshitz-Looyenga formalism

$$\varepsilon_{1,p}^{1/3} - 1 = \beta(\varepsilon_{1,s}^{1/3} - 1)\ ,\ \varepsilon_{2,s} = \frac{\varepsilon_{2,p}}{\beta}\left(\frac{\varepsilon_{1,s}}{\varepsilon_{1,p}}\right)^{2/3} \tag{4.3}$$

where β is the powder volume fraction (ratio of powder density and crystallographic bulk density)[20,94].

The following fit functions are a first try to simulate the experimental data with simplified models which can be improved further in future work. The experimental data at 23 °C was fitted with a Lorentz-Oscillator function[128] according to

$$\varepsilon = \varepsilon_\infty + \frac{\omega_{p,L}^2}{\omega_0^2 - \omega^2 - i\gamma_L\omega} \tag{4.4}$$

where ε_∞ is the background permittivity, ω_p is the plasma frequency, ω is the angular frequency of the sample, γ is the damping rate. The ε_∞ with 2.6, the $\omega_{p,L}/2\pi$ with 16.2 THz, the $\omega_0/2\pi$ with 12.4 THz, and the $\gamma_L/2\pi$ with 16 THz were used for the simulation [234,235]. The experimental data at 330 °C was fitted with a Drude function [128] according to

$$\varepsilon = \varepsilon_\infty - \frac{\omega_{p,D}^2}{\omega^2 - i\gamma_D\omega} \tag{4.5}$$

where ε_∞ with 2.2, $\omega_{p,D}/2\pi$ with 3.3 THz, and $\gamma_D/2\pi$ with 17.15 THz were used for the simulation.

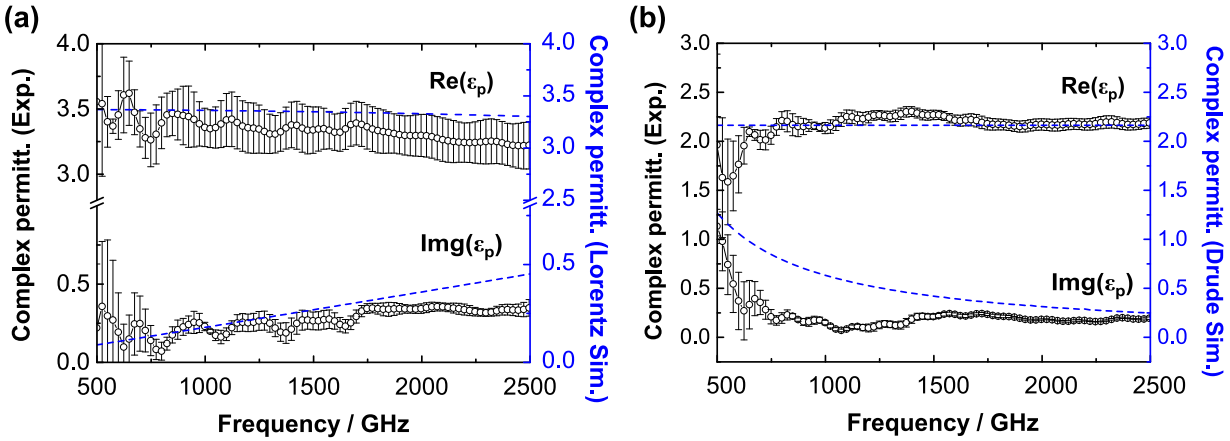

Figure A.3: ***(a)*** *Experimental complex permittivity and Lorentz oscillator simulation for ZnO:Ga at 23 °C and* ***(b)*** *Experimental complex permittivity and Drude model simulation for ZnO:Ga at 330 °C.*

B Supporting information of Chapter 3.2

Content:

- Powder X-ray diffraction of fresh and used catalyst
- In-situ microwave conductivity of VPP
- Near-ambient pressure X-ray photoelectron spectroscopy

Powder X-ray diffraction

The powder XRD measurements were performed in Bragg-Brentano geometry on a Bruker AXS D8 Advance II theta/theta diffractometer with Ni filtered Cu Kα radiation. A position sensitive energy dispersive LynxEye silicon strip detector was used. Figure B.1 shows the powder XRD pattern before (fresh catalyst) and after (used catalyst) the in-situ microwave conductivity experiment.

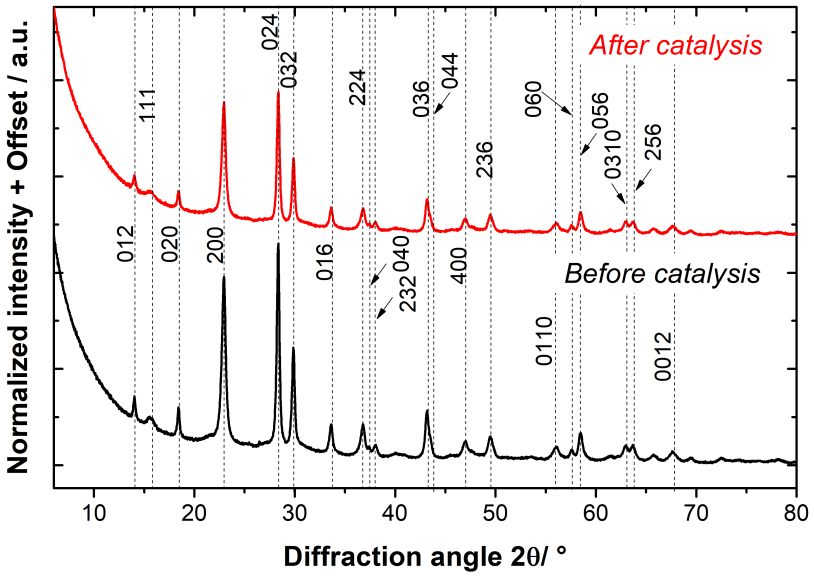

Figure B.1: *Powder XRD pattern of polycrystalline VPP before and after use in propane oxidation at 400 °C under the various feed compositions specified in the Chapter 3.2.*

In-situ microwave conductivity of VPP

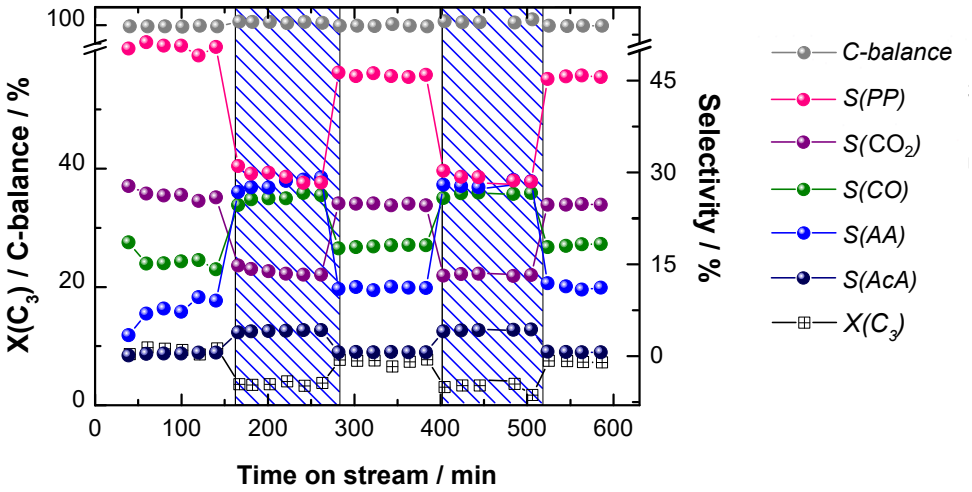

Figure B.2: *Catalytic performance under dry (3 vol% C_3, 6 vol% O_2, inert) and wet (3 vol% C_3, 6 vol% O_2, 5 vol% steam, inert) feed conditions at 400 °C measured in the MCPT setup; X describes the conversion of propane; S describes the selectivity to propylene (PP), acrylic acid (AA), acetic acid (AcA), CO and CO_2.*

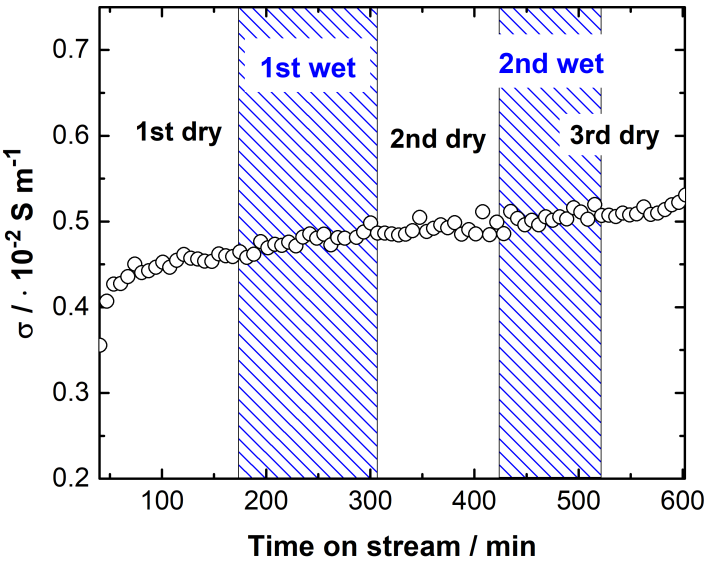

Figure B.3: *Microwave conductivity of VPP under dry (6 vol% O_2, inert) and wet (6 vol% O_2, 5 vol% steam, inert) feed conditions at 400 °C.*

Near-ambient pressure X-ray photoelectron spectroscopy

Table B.3: *$V2p_{3/2}$ fit parameters (cf. Figure 3.2.4 in Chapter 3.2) where FWHM is the full width at half maximum, and GL is the Gaussian-Lorentzian ratio as defined in CasaXPS[179].*

Species	$V2p_{3/2}$ V^{4+}	$V2p_{3/2}$ V^{5+} (I)	$V2p_{3/2}$ V^{5+} (II)
FWHM	1.72 - 1.66	1.58 - 1.61	1.58 - 1.61
Peak position / eV	516.9	518.0	517.8
Line shape	GL(45)	GL(45)	GL(45)

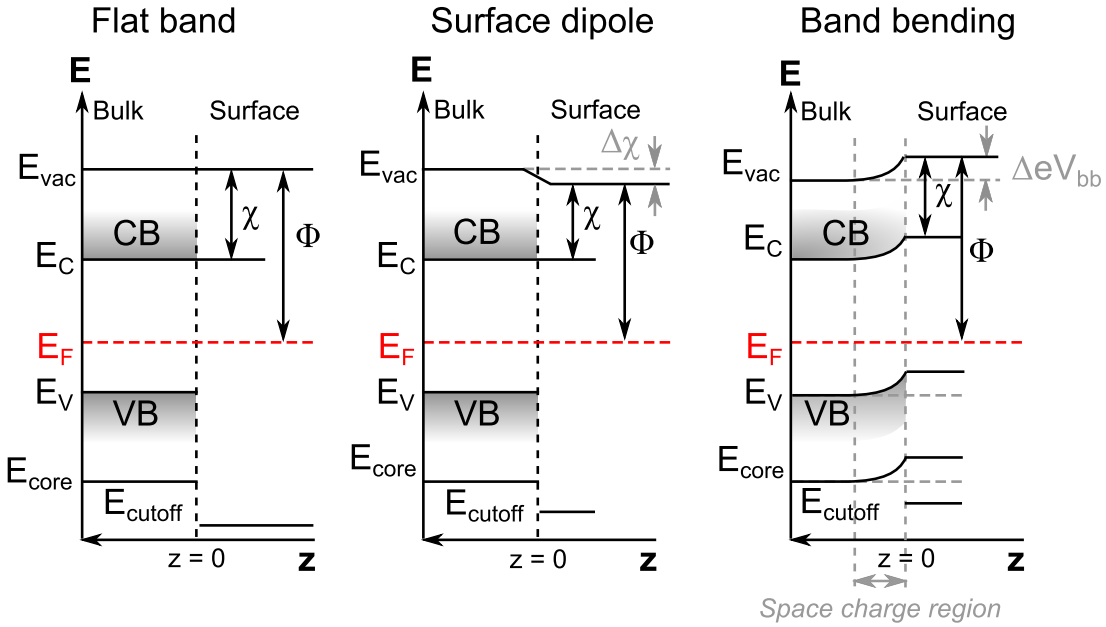

Figure B.4: *Schematic changes of energetic conditions at a p-type semiconductor interface for flat band, surface dipole, and band bending situations. Further, E_{vac} is the vacuum level, E_C is the conduction band (CB) edge, E_F is the Fermi level, E_V is the valence band (VB) edge, E_{core} is the core level, E_{cutoff} is the secondary electron cutoff edge, χ is the electron affinity, and Φ is the work function. The changes of surface dipole modification shifts $\Delta\chi$. The term ΔeV_{bb} considers band bending (according to[236]).*

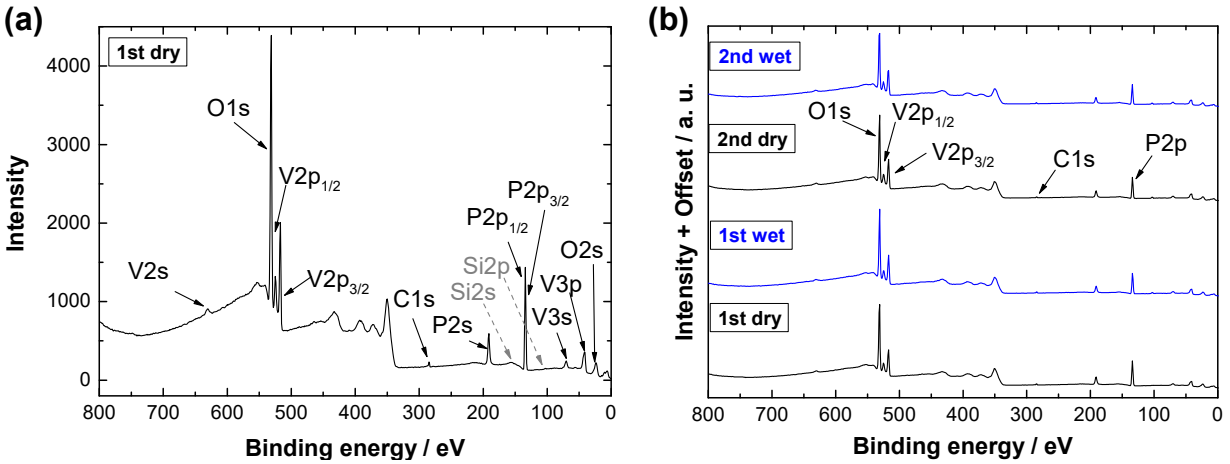

Figure B.5: *The XPS core level peak assignment of the survey spectra (according to[237]) of VPP for the 1st dry feed* ***(a)****, and XP survey spectra (E_{ph} of 860 eV) of VPP for all applied gas feeds* ***(b)****.*

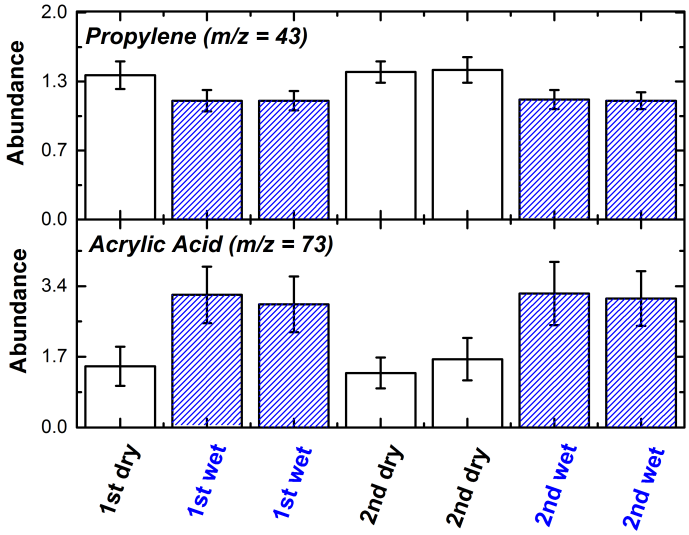

Figure B.6: *PTR-MS trace of propylene (top, protonated mass m/z = 43) and acrylic acid (bottom, protonated mass m/z = 73) under the various feed compositions as indicated on the abscissa.*

C Supporting information of Chapter 3.3

Content:

- Sample preparation
- Powder X-ray diffraction of CuO/ZnO
- Microwave Hall effect setup
  (i) Equations for different conductivity regions, (ii) Apparent filling factor α,
  (iii) Tuning and iris screws, (iv) Comsol simulation, (v) Error propagation
- Temperature dependent behavior of ZnO

Sample preparation

The precursor solutions contained a mixture of Zinc-nitrate solution and a sodium carbonate base. Both were added simultaneously into an automated reactor (Labmax from Mettler-Toledo). The pH (6.5) and temperature (115 °C) were kept constant during the precipitation process. The $(Zn)_5(CO_3)_2(OH)_6$ precipitate was subsequently aged, washed, spray dried, and calcined at 330 °C (with a heating rate of 2 °C/min) for 180 min. Nitrogen adsorption experiments were carried out at -196 °C on a Quantachrome Autosorb-1 analyzer. Prior to the measurement, the sample was out-gassed in vacuum at 70 °C for 2 h. The specific surface area was 38 m^2g^{-1} (Brunauer-Emmett-Teller method).

In a subsequent step, the Cu citrate route was used for impregnation where $Cu_2C_6H_4O_7{\cdot}xH_2O$ was dissolved in aqueous ammonia solution (12.5 vol%). The copper containing solution was added to the ZnO support, stirred, dried overnight, and calcined (330 °C for 180 min with 2 °C/min). The nominal Cu loading was 10 wt% for the model Cu/ZnO catalyst. The synthesis and characterization of ZnO and Cu/ZnO were already published[23].

Powder X-ray diffraction of CuO/ZnO

The powder XRD pattern of ZnO is shown in Figure A.1 while the powder XRD pattern of CuO/ZnO is presented in Figure C.1. Powder XRD verified the phase purity for ZnO and CuO/ZnO. The measurements were performed in Bragg-Brentano geometry on a Bruker AXS D8 Advance II theta/theta diffractometer, using Ni filtered Cu Kα radiation and a position sensitive energy dispersive LynxEye silicon strip detector. The sample powder was

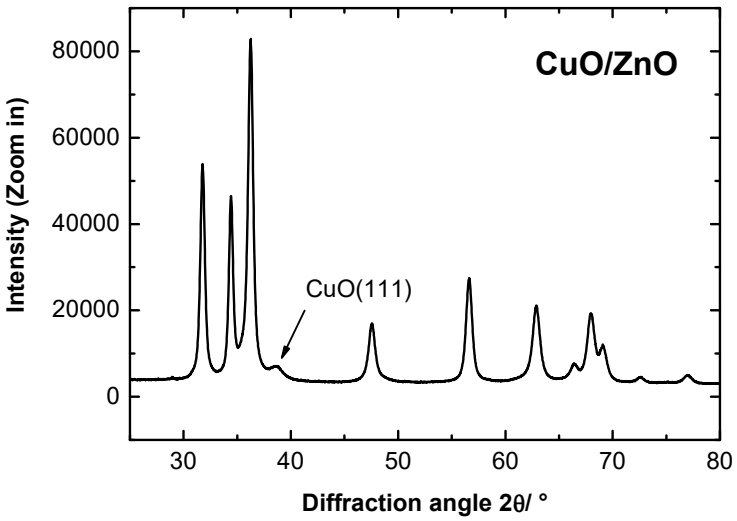

Figure C.1: *Powder XRD pattern of CuO/ZnO.*

filled into the recess of a cup-shaped sample holder, the surface of the powder bed being flush with the sample holder edge (front loading).

Microwave Hall effect setup

(i) Equations for different conductivity regions

The cavity perturbation equations provide the relationship between the frequency shift and the change in quality factor. In addition, they are based on the so-called quasi-static approximation (cf. Chapter 2.1.1)[32,100,238]. After various transformations (Lui[238], cf. page 237 ff.), the alternative form of these equations is obtained

$$1 + \frac{N}{\alpha}\frac{\Delta\omega}{\omega_e} = \frac{1 + N(\varepsilon_1 - 1)}{\left[1 + N(\varepsilon_1 - 1)\right]^2 + (N\varepsilon_2)^2} \tag{4.6}$$

$$\frac{N}{\alpha}\Delta\left(\frac{1}{2Q}\right) = \frac{N\varepsilon_2}{\left[1 + N(\varepsilon_1 - 1)\right]^2 + (N\varepsilon_2)^2} \tag{4.7}$$

where N is the polarization factor, α the filling factor, ω_e the angular resonance frequency of the empty cavity, $\Delta\omega = \omega_e - \omega_l$ is the difference between empty and sample-loaded angular resonance frequency, Q the quality factor, and $\Delta(1/2Q)$ is $(1/Q_l) - (1/Q_e)$ assuming $Q_e > Q_l$. The complex electrical permittivity ε (cf. Chapter 2.1.1) is defined as

$$\varepsilon = \varepsilon_1 + i\varepsilon_2 \tag{4.8}$$

Furthermore, its imaginary part ε_2 is related to the microwave conductivity σ (cf. Chapter 2.1.1) according to

$$\sigma = \varepsilon_0 \omega_l \, \varepsilon_2 = 2\pi f_l \, \varepsilon_0 \varepsilon_2 \tag{4.9}$$

where ε_0 is the vacuum permittivity ($8.854 \cdot 10^{-12}$ F m^{-1}).

Intermediate conductivity region

For the intermediate conductivity region, it is defined that $N\varepsilon_2 > N(\varepsilon_1 - 1) >> 1$ [32]. Equations 4.6 and 4.7 reduce to 4.10 and 4.11, respectively[a].

$$\frac{\Delta\omega}{\omega_e} = \frac{\alpha}{N} \tag{4.10}$$

$$\Delta\left(\frac{1}{2Q}\right) = \frac{\alpha}{N^2 \varepsilon_2} \tag{4.11}$$

From equations 4.10 and 4.11 the equation for σ is deduced

$$\begin{aligned} \Delta\left(\frac{1}{2Q}\right) &= \frac{1}{\alpha}\left(\frac{\Delta\omega}{\omega_e}\right)^2 \frac{2\pi f_l \varepsilon_0}{\sigma} \\ \sigma &= \left(\frac{\Delta\omega}{\omega_e}\right)^2 2\pi f_l \varepsilon_0 \frac{1}{\alpha} 2 \left(\frac{Q_e - Q_l}{Q_e Q_l}\right)^{-1} \\ \sigma &= 4\pi\varepsilon_0 f_l \left(\frac{\Delta\omega}{\omega_e}\right)^2 \left(\frac{Q_e Q_l}{Q_e - Q_l}\right) \frac{1}{\alpha} \end{aligned} \tag{4.12}$$

Equation 4.12 is consistent with Liu *et al.* [32] and Na *et al.* [38].

Low conductivity region

For the low conductivity region, it is defined that $N\varepsilon_2 < N(\varepsilon_1 - 1) << 1$ [32,100,239]. Equations 4.6 and 4.7 reduce to 4.13 and 4.14, respectively.

$$\frac{\Delta\omega}{\omega_e} = -\alpha\,(\varepsilon_1 - 1) \tag{4.13}$$

$$\Delta\left(\frac{1}{2Q}\right) = \alpha\varepsilon_2 \tag{4.14}$$

[a] Note: Ong *et al.* used $\Delta\omega/\omega_e = -\alpha/N$ [31]

From equations 4.13 and 4.14 the equation for σ is deduced

$$\begin{aligned} \alpha\varepsilon &= \frac{1}{2}\left(\frac{Q_e - Q_l}{Q_e Q_l}\right) \\ \frac{\sigma}{2\pi f_l \varepsilon_0} &= \frac{1}{2\alpha}\left(\frac{Q_e - Q_l}{Q_e Q_l}\right) \\ \sigma &= \pi f_l \varepsilon_0 \left(\frac{Q_e - Q_l}{Q_e Q_l}\right)\frac{1}{\alpha} \end{aligned} \tag{4.15}$$

Equation 4.15 is again consistent with Liu *et al.*[32] and Na *et al.*[38].

(ii) Apparent filling factor α

On the basis of quasi-static approximation the apparent filling factor α is given by[32]

$$\alpha = \frac{\int |E_i|^2 \, dV_S}{2\int |E_0|^2 \, dV_C} \tag{4.16}$$

The volume integrals of the sample E_i and cavity E_0 is shown in the following. Figure 2.1.1 shows a simplified geometric structure of a cylindrical cavity resonator which will be used in the following paragraph. The expression of the TE_{112} electric field distribution in cylindrical coordinates is given by

$$E_r = -E_{0,max}\left[\frac{J_1(k_c r)}{k_c r}\right]\sin(\phi)\sin(k_z z) \tag{4.17}$$

$$E_\phi = -E_{0,max} J_1'(k_c r)\cos(\phi)\sin(k_z z) \tag{4.18}$$

$$E_z = 0 \tag{4.19}$$

where $E_{0,max}$ is the intensity of electric field antinode, $k_c = (k_c\mathrm{R})'_{11}/\mathrm{R}$ with $(k_c\mathrm{R})'_{11} = 1.841$ is the Bessel root of the Bessel function $J_1'(k_c R) = 0$[82,85], and $k_z = 2\pi/d$.

The volume integral of the cavity E_0 is

$$\int |E_0|^2 \, dV_C = \int |E_r|^2 \, dV_C + |E_\phi|^2 \, dV_C + |E_z|^2 \, dV_C \tag{4.20}$$

and referring to the expression of the TE_{112} electric field distribution mentioned above, equation 4.20 reduces to

$$\int |E_0|^2 \, dV_C = \int |E_r|^2 \, dV_C + |E_\phi|^2 \, dV_C \tag{4.21}$$

The integrals of $\int |E_r|^2 \, dV_C$ and $\int |E_\phi|^2 \, dV_C$ are solved. The result of the last step is

$$\begin{aligned} \int |E_0|^2 \, dV_C = |E_{0,max}|^2 \frac{\pi d}{2} \Bigg(& \frac{R^2}{1.841^2} \int_0^1 \frac{\left[J_1 \left(1.841 \frac{r}{R} \right) \right]^2}{\frac{r}{R}} d\frac{r}{R} \\ & + R^2 \int_0^1 \left[J_1' \left(1.841 \frac{r}{R} \right) \right]^2 \left(\frac{r}{R} \right) d\frac{r}{R} \Bigg) \end{aligned} \tag{4.22}$$

The numerical integration solution of equation 4.22 is

$$\begin{aligned} \int |E_0|^2 \, dV_C &= |E_{0,max}|^2 \frac{\pi R^2 d}{2} \left(\frac{0.2807}{1.841^2} + 0.036537 \right) \\ &= |E_{0,max}|^2 \, V_C \frac{1}{2} \left(\frac{0.2807}{1.841^2} + 0.036537 \right) \\ &= |E_{0,max}|^2 \, V_C 0.0597 \end{aligned} \tag{4.23}$$

It is known, that the sample is located in the electric field maxima (cf. Figure 3.3.2b in Chapter 3.3.3). Therefore, the integral of the electric field E_i (r = 0, $\phi = 0$, and z = d/4) over the sample is

$$\begin{aligned} E_{r,sample} &= 0 \\ E_{\phi,sample} &= -E_{0,max} J_1'(k_c r) \cos(\phi) \sin(k_z z) \\ &= -E_{0,max} J_1'(0) \cos(0) \sin\left(\frac{2\pi d}{d4} \right) \\ &= -\frac{1}{2} E_{0,max} \\ E_{z,sample} &= 0 \end{aligned} \tag{4.24}$$

Thus, the volume integral of the sample E_i is

$$\int |E_i|^2 \, dV_S = \left| \frac{1}{2} E_{0,max} \right|^2 V_S = \frac{1}{4} |E_{0,max}|^2 \, V_S \tag{4.25}$$

After solving the volume integrals of the cavity (equation 4.21) and sample (equation 4.25) the apparent filling factor α is

$$\alpha = \frac{\int |E_i|^2 \, dV_S}{2 \int |E_0|^2 \, dV_C} = \frac{\frac{1}{4} |E_{0,max}|^2 V_S}{2 |E_{0,max}|^2 V_C 0.0597} = 2.1 \frac{V_S}{V_C} \tag{4.26}$$

(iii) Tuning and iris screws

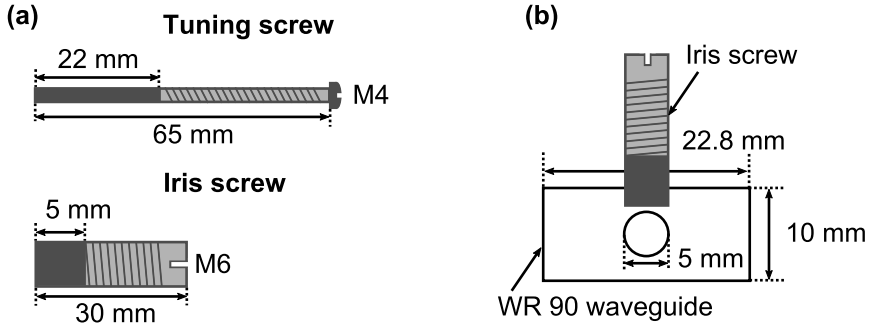

Figure C.2: *Side view and detailed description of the* ***(a)*** *Tuning and iris screws, and* ***(b)*** *Position of the iris screw and iris hole.*

(iv) Comsol simulation

The simulation was performed with COMSOL Multiphysics 5.1 finite element method software package using the RF module.

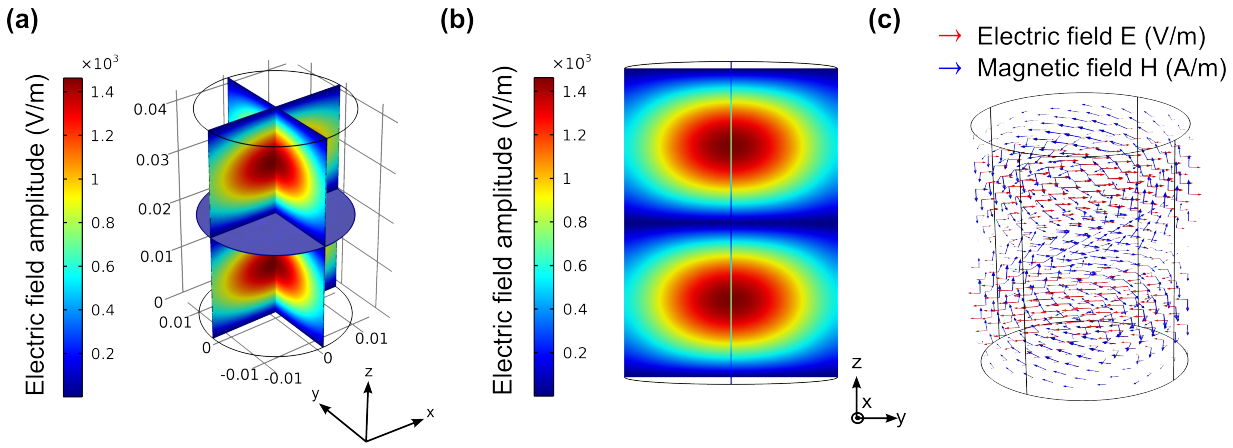

Figure C.3: *Electric field amplitude for a bimodal TE_{112} cavity* ***(a)*** *3D overview* ***(b)*** *Yz-plane, and* ***(c)*** *The electric and magnetic field are shown in arrows (COMSOL 5.1 simulation).*

(v) Error propagation

The error bars for the calibration constant K, the Hall mobility μ_H, the absolute charge carrier concentration N_C, and the conductivity σ are defined as follows. These errors were given as the maximum error of a combined measured quantity. The partial derivatives were computed due to the fact that our variables (K, μ_H, and σ) can be a function of multiple parameters.

The calibration constant K is given by

$$K \pm \Delta K = \frac{\mu_{H,DC}}{\frac{10^4}{B}\frac{Q_e}{Q_e - Q_l}\Delta S_{21}} \tag{4.27}$$

Equation 4.28 shows the highest possible error using the total differential of K. The maximum error ΔK is the arithmetic (linear) addition of all single errors and is given by

$$\begin{aligned}\Delta K &= \left|\frac{\partial K}{\partial \mu_{H,DC}}\right| \Delta\mu_{H,DC} + \left|\frac{\partial K}{\partial B}\right| \Delta B + \left|\frac{\partial K}{\partial Q_e}\right| \Delta Q_e + \left|\frac{\partial K}{\partial Q_l}\right| \Delta Q_l + \left|\frac{\partial K}{\partial \Delta S_{21}}\right| \Delta\Delta S_{21} \\ &= \left|\frac{B\,(Q_e - Q_l)}{10^4 Q_e \Delta S_{21}}\right| \Delta\mu_{H,DC} + \left|\frac{(Q_e - Q_l)\,\mu_{H,DC}}{10^4 Q_e \Delta S_{21}}\right| \Delta B + \left|-\frac{B\mu_{H,DC}}{10^4 Q_e \Delta S_{21}}\right| \Delta Q_l \\ &+ \left|\frac{BQ_l\mu_{H,DC}}{10^4 Q_e^2 \Delta S_{21}}\right| \Delta Q_e + \left|-\frac{B\,(Q_e - Q_l)\,\mu_{H,DC}}{10^4 Q_e \Delta S_{21}^2}\right| \Delta\Delta S_{21}\end{aligned} \tag{4.28}$$

where $\Delta\mu_{H,DC}$, ΔB, ΔQ_e, ΔQ_l, $\Delta\Delta S_{21}$ are standard deviations of their arithmetic means. The same procedure was performed for $\Delta\mu_H$, ΔN_C, and $\Delta\sigma$.

Temperature dependent behavior of ZnO

Comparative measurements were performed on a single crystal with the static Hall effect technique (contact van-der-Pauw-method) to evaluate and to validate our MHE measurements (cf. Figure 3.3.5). Figure C.4 presents the temperature-dependent conductivity and Hall mobility.

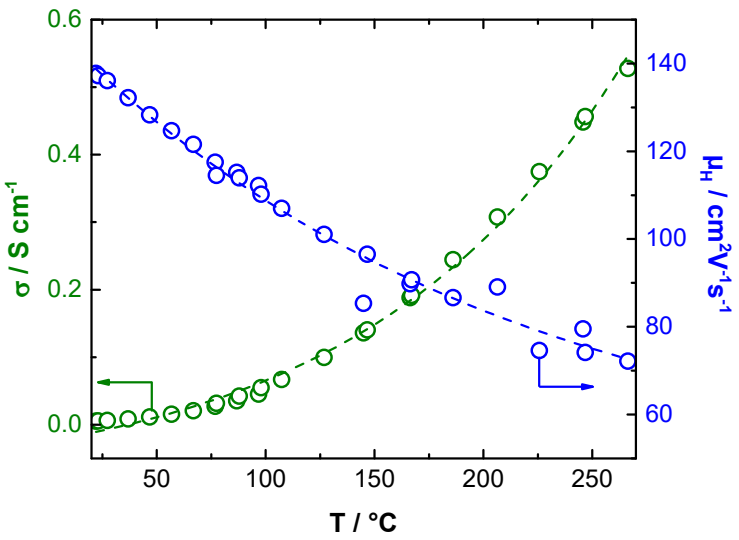

Figure C.4: *Temperature dependent conductivity σ (green), and Hall mobility μ_H (blue) measured with the van-der-Pauw technique. A trend line was added to guide the eye.*

D Supporting information of Chapter 3.4

Content:

- Sample preparation
- Powder X-ray diffraction
- In-situ microwave Hall effect
- Apparent activation energy and reaction order

Sample preparation

The catalyst preparation was based on the synthesis route published by Schumann *et al.*[23]. The ZnO supports were prepared by a pH-controlled co-precipitation (1 M metal nitrates and 1.6 M Na_2CO_3) in an automated Labmax reactor, aged, washed, spray-dried and calcined (330 °C for 180 min with 2 °C/min). The ratio of $[Al^{3+}]/([Al^{3+}] + [Zn])$ was varied to achieve a varying Al content (nominal 0 - 4 mol%). In a subsequent step, the Cu citrate route was used for impregnation, where $Cu_2C_6H_4O_7 \cdot xH_2O$ was dissolved in aqueous ammonia solution (12.5 vol%). The solution (3 ml) was added to the catalyst support (3 g), stirred, dried overnight, and calcined (330 °C for 180 min with 2 °C/min). The nominal Cu loading was 10 wt%.

Powder X-ray diffraction

The powder XRD data were analyzed by full pattern fitting using the Rietveld method as implemented in the TOPAS software [TOPAS version 5, copyright 1999-2014 Bruker AXS]. TOPAS uses a convolution approach to synthesize the diffraction profiles from instrumental and sample contributions.

ZnO forms a wurtzite type crystals which reflects the thermodynamically stable phase. Its crystal structure belongs to the hexagonal space group C_{6v}^4 (Schoenflies notation)[110]. For ZnO, the lattice parameters a and c and the z coordinate of the oxygen atom were refined. The peak profiles of ZnO exhibit anisotropic broadening, i.e. the peak widths are not a smooth function of the diffraction angle but are also a function of *hkl*. The best overall agreement for the whole sample series was achieved using a peak shape model which combined isotropic strain broadening (Voigt profile with width proportional to $\tan(\theta)$) and anisotropic size broadening (Lorentz profile). For the latter contribution,

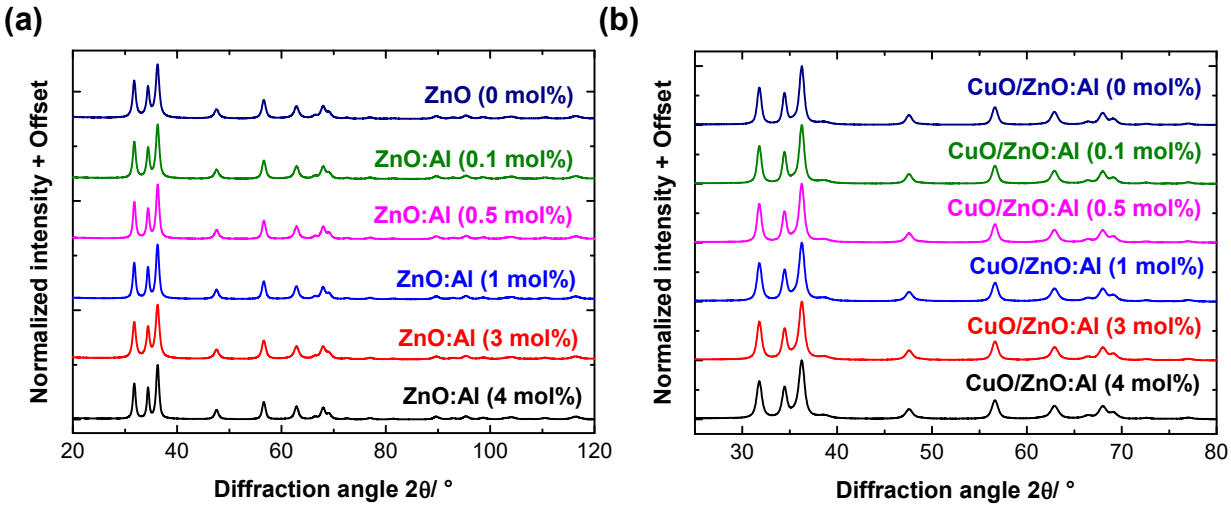

Figure D.1: *Powder XRD patterns of* ***(a)*** *All ZnO:Al supports, and* ***(b)*** *All CuO/ZnO:Al model catalysts.*

the *hkl* dependence published by Stephens[240], originally proposed for anisotropic strain broadening, was combined with a $1/\cos(\theta)$ dependence to represent a crystallite size effect. However, the systematic disagreement seen in the difference curves of the fits indicates that this model is still not completely satisfactory. Hence, the extracted size and strain parameters are not expected to be very accurate. Concerning CuO, the reflections are relatively small and extensively overlapping with ZnO. Thus, neither lattice parameters nor atomic coordinates were refined, but kept fixed at the literature values (ICSD 43179). The peak shapes were refined as Voigt profiles with isotropic crystallite size broadening.

The volume-weighted mean column lengths L_{Vol}-IB along the *c*-direction are listed in Table 3.2 and were used as an approximate measure for the crystallite sizes.

Table D.4: *XRD crystallite size (L_{Vol}-IB in c-direction as determined form Rietveld fit) of ZnO for pure ZnO:Al supports and impregnated ZnO:Al catalysts.*

Pure ZnO:Al supports						
Al / *wt%*	1.7	1.1	0.6	0.3	0.1	0
Crystallite size ZnO / *nm*	11.3	11.4	13.5	15	15.5	17.7
Impregnated ZnO:Al catalysts						
Crystallite size ZnO / *nm*	15	14	15.5	17.7	18.7	20.3

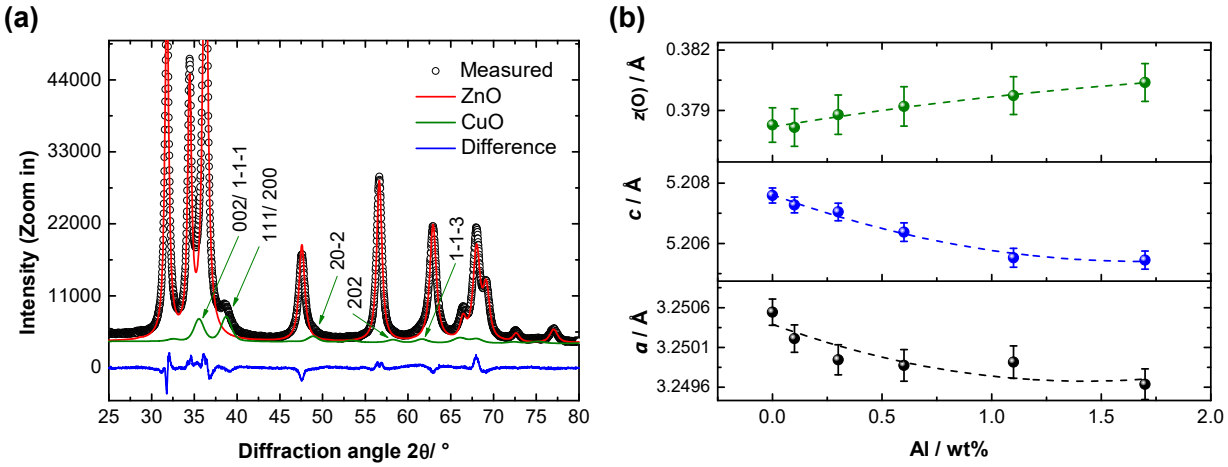

Figure D.2: ***(a)*** *Rietveld fit of CuO/ZnO:Al (1.7 wt% Al) with the measured (black circles), calculated (red line for ZnO, and green line for CuO) powder XRD patterns, the corresponding difference curve (blue line) and* ***(b)*** *Lattice parameters a, and c, and atomic coordinate z of oxygen from the Rietveld refinements as a function of Al content determined by XRF.*

Table D.5: *Cu content and domain size determined by in-situ powder XRD measurements in reducing atmosphere(5 vol% H_2 in He) for 1 h at 250°C.*

	FHI-ID	**Cu / *wt%***	$L_{Vol} - IB$ **/ *nm***
Cu/ZnO	25651	9.6 ± 0.3	6.3 ± 0.3
Cu/ZnO:Al	25397	10.6 ± 0.3	5.7 ± 0.3

In-situ microwave Hall effect

The final setup, which was introduced at the beginning of the present work, was used. Figure 2.2.3a in Chapter 2.2.3 shows the sketch of the experimental setup and Figure 2.2.3b presents the in-situ TE_{112} bimodal cavity. The principle of in-situ MHE measurements was introduced in Chapter 3.3.

The reactor tube was filled with the catalyst (sieve fraction 100 - 200 μm) to a bed length of 2.6 - 2.7 mm corresponding to a weight of 12 mg. The catalysts were reduced in-situ followed by the reverse water-gas shift feed (contact time of 0.295 g s ml^{-1}), see Chapter 3.4.2 in the main thesis. The gas purity was 99.9 % for CO_2, 99.999 % for H_2, and 99.998 % for Ar (Westfalen AG). The MHE measurements were started after reaching steady-state values and the average of at least ten consecutive cycles is shown. The gas composition was monitored and the average CO formation is presented for at least 2 h.

Here, the absolute values are depicted in Figure D.3 while the normalized values are shown in Figure 3.4.2.

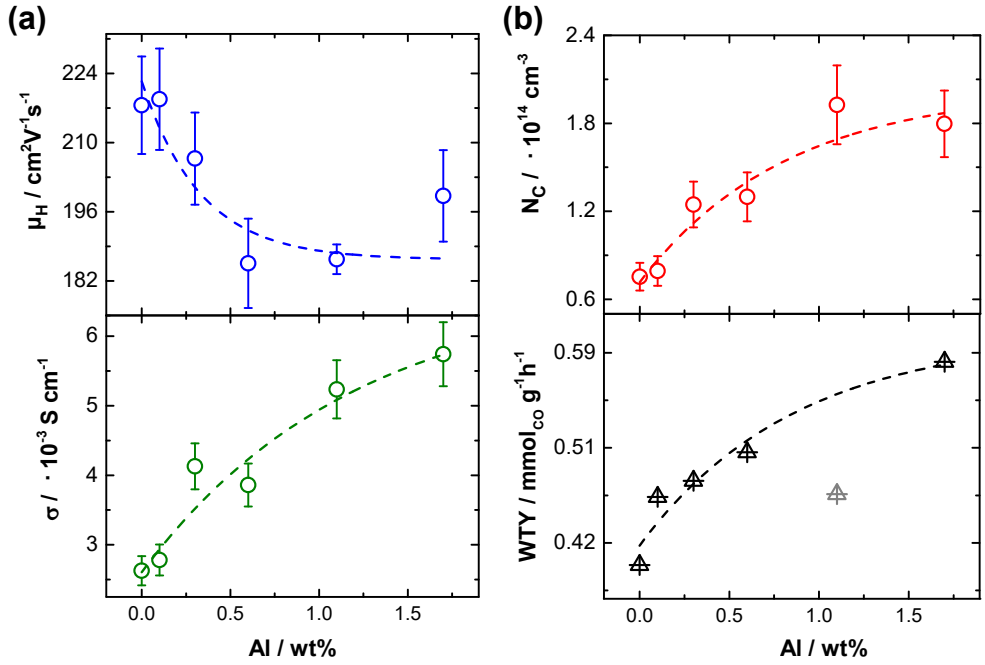

Figure D.3: ***(a)*** *Microwave Hall mobility μ_H (blue) and microwave conductivity σ (green) as a function of the Al content, which was determined by XRF, and* ***(b)*** *Calculated absolute charge carrier concentration N_C and weight time yield (WTY) of CO formation under reaction conditions (1 H_2/ 1 CO_2/ 8 Ar) at 230 °C.*

Apparent activation energy and reaction order

The apparent activation energies E_a of CO formation were derived from the Arrhenius plot

$$ln(k) = ln(A) - \frac{E_a}{R}\frac{1}{T} \tag{4.29}$$

where k is the CO formation rate, A is the pre-exponential factor, R is the universal gas constant, and T is the temperature. The E_a was calculated from the linear relationship (*ln(k)* vs. *1/T*) which is illustrated in Figure D.4.

The reaction order for H_2 and CO_2 was obtained by varying the ratio of H_2/CO_2 (1/1; 1/2; 1/3; and 1/1; 2/1; 3/1) with a flow of 10 ml/min at 230 °C. Table D.6 presents the results of E_a, and the reaction order of H_2 and CO_2. The errors for the reaction order and E_a were determined from the uncertainty of the linear fit function. The relative value for the reaction orders were lower than 3.6 % and are not specifically shown. For two samples

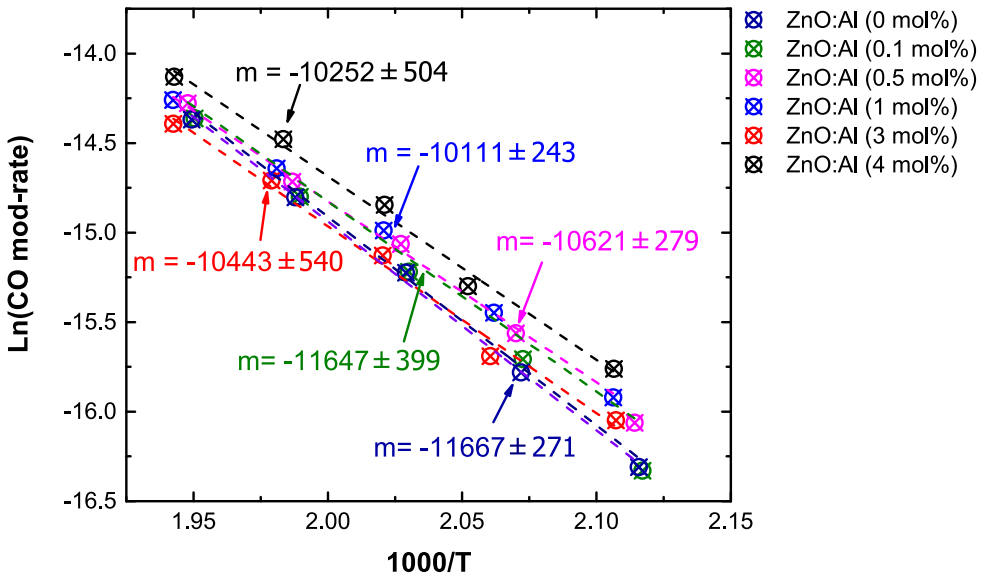

Figure D.4: *Arrhenius plots of the Cu/ZnO:Al based model catalysts.*

(1.7 wt% and 1.1 wt% Al) traces of methanol were detected but the peak area was below the quantification limit.

Table D.6: *Apparent activation energies E_a in reverse water-gas shift for a temperature range between 200 - 240 °C and the reaction order of H_2 and CO_2 taken at different gas feeds at 230 °C.*

Cu/ZnO:Al model catalysts						
Al nominal value / *mol%*	4	3	1	0.5	0.1	0
***App.* E_a / *kJ mol*$^{-1}$**	85 ± 6	87 ± 6	84 ± 3	88 ± 3	97 ± 5	97 ± 3
Reaction order H_2	0.14	0.16	0.14	0.15	0.15	0.17
Reaction order CO_2	0.31	0.39	0.32	0.29	0.28	0.25

Figure D.5 shows the comparison between relative ex-situ and in-situ reverse water-gas shift activity.

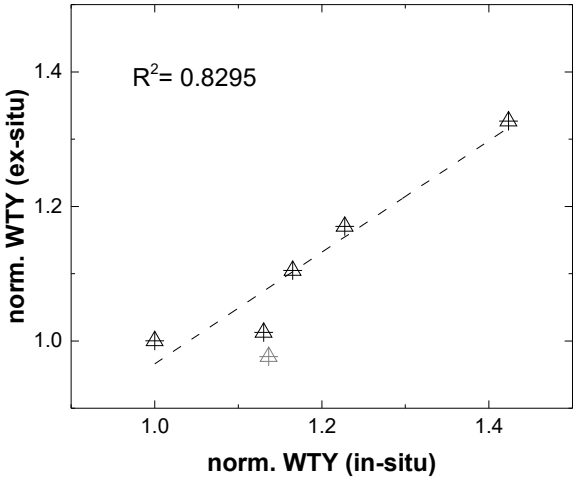

Figure D.5: *Comparison of in-situ and ex-situ activity of all Cu/ZnO:Al model catalysts (normalized to Cu/ZnO), where Cu/ZnO:Al (1.1 wt%) is gray highlighted.*

Abbreviations

AA	Acrylic Acid
AcA	Acetic Acid
AC	Alternating Current
BE	Binding Energy
BET-SA	Brunauer Emmett Teller Surface Area
DC	Direct Current
FWHM	Full Width at Half Maximum
GC	Gas Chromatography
GL	Gaussian-Lorentzian
HR-TEM	High Resolution Transmission Electron Microscopy
IMFP	Inelastic Mean Free Path
NAP-XPS	Near-Ambient-Pressure X-ray Photoelectron Spectroscopy
NEXAFS	Near-Edge X-ray Absorption Fine Structure
MCPT	Microwave Cavity Perturbation Technique
MHE	Microwave Hall Effect
PP	Propylene
PTR-MS	Proton Transfer-Reaction Mass Spectrometry
RFC	Reactive Frontal Chromatography

SA	Surface Area
SMSI	Strong Metal Support Interaction
TE	Transverse Electric
TEY	Total Electron Yield
TEM	Transmission Electron Microscopy
THz-TDS	Terahertz Time-domain Spectroscopy
TM	Transverse Magnetic
VPO	Vanadium-Phosphorous Oxide
VPP	Vanadyl Pyrophosphate
WGS	Water-Gas-Shift
WTY	Weight Time Yield
XAS	X-ray Absorption Spectroscopy
XRF	X-ray Fluorescence Spectroscopy
XRD	X-ray Diffraction
XPS	X-ray Photoelectron Spectroscopy

List of symbols

$\langle\tau\rangle$	Relaxation time averaged over the distribution of electrons
$\Delta(\frac{P_H}{P_l})^{1/2}$	Power difference between magnetic field on and off
Δf_e	Full half width at half maximum of the power peak of the empty cavity
Δf_l	Full half width at half maximum of the power peak of the sample-loaded cavity
ΔH	Reaction enthalpy
ΔS_{21}	Difference between magnetic field on and off for the scattering coefficient S_{21}
$A,\ B$	Calibration constants for the TM_{0n0} cavity
a_{mn}	Nth order root of the mth order Bessel function
B	Magnetic induction (magnetic field)
c	Speed of light
d	Cavity height
E	Electric field
e	Elementary charge
E_a	Apparent activation energy
E_{cutoff}	Secondary electron cutoff
E_C	Conduction band edge
E_{core}	Core level

E_D	Donor level
E_F	Fermi level
E_H	Hall field
E_r	Radial component of the electric field
E_V	Valence band edge
E_{Vac}	Vacuum level
E_z	Longitudinal component of the electric field
E_Φ	Angular component of the electric field
f_e	Resonance frequency of the empty cavity
f_l	Resonance frequency of the sample-loaded cavity
F_l	Lorentz force
f_{mnp}	Resonance frequency of the cavity (general form)
H	Magnetic field
I	Current
I_p	Sample current
J_m	mth order of the Bessel function
J'_m	First derivative mth order of the Bessel function
k	Boltzmann's constant
K	Calibration constant for the bimodal cavity
m	Slope
m^*	Effective mass
N_C	Charge carrier concentration
N_e	Electron concentration

N_{eff}^{V}	Effective hole density of states in the valance band
P_1	Microwave power of the incident primary mode
P_H	Microwave Hall power detected for the secondary mode
P_{i1}	Microwave input power at port 1
P_{o2}	Microwave output power at port 2
Q	Quality factor
q	Electronic charge
Q_e	Quality factor of the empty cavity
Q_l	Quality factor of the sample-loaded cavity
R	Radius of the cavity
R_H	Hall coefficient
R_{meas}	Electrical resistance
S_{11}	Reflection coefficient of port 1
S_{12}	Transmission coefficient from port 2 to port 1
S_{22}	Reflection coefficient of port 2
S_{21}	Transmission coefficient from port 1 to port 2
T	Temperature
U_H	Hall voltage
U_p	Sample voltage
V_C	Volume of the cavity
V_S	Volume of the sample
α	Apparent filling factor
Γ	Reflection coefficient

ε_0	Electrical permittivity of vaccum
$\varepsilon_{1,p}$	Real part of the powder permittivity (= Re(ε_p))
$\varepsilon_{1,s}$	Real part of the bulk permittivity (= Re(ε_s))
$\varepsilon_{2,p}$	Imaginary part of the powder permittivity (= Img(ε_p))
$\varepsilon_{2,s}$	Imaginary part of the bulk permittivity (= Img(ε_s))
ε_p	Powder permittivity
ε_s	Bulk permittivity
κ	Coupling coefficient
λ	Resonance wavelength
μ	Magnetic permeability
μ_0	Magnetic permeability of vacuum
μ_H	Microwave Hall mobility (= $\mu_{H,MW}$)
$\mu_{H,DC}$	Static Hall mobility
$\mu_{H,e}$	Hall mobility of the electron
$\mu_{H,h}$	Hall mobility of the electron hole
υ	Velocity
ρ	Electrical resistivity
σ	(Microwave) conductivity
σ_{DC}	Direct current conductivity
σ_p	Powder conductivity
σ_s	Bulk conductivity
Φ	Work function
χ	Electron affinity

ω_e	Angular resonance frequency of the empty cavity
ω_l	Angular resonance frequency of the sample-loaded cavity

List of Figures

List of Tables

Bibliography

[1] R. Schlögl, *ChemCatChem* **2017**, *9*, 533.

[2] K. Doroodian, R. Boyd, *Energy Policy* **2003**, *31*, 989.

[3] T. R. Karl, K. E. Trenberth, *Science* **2003**, *302*, 1719.

[4] J. Zachos, M. Pagani, L. Sloan, E. Thomas, K. Billups, *Science* **2001**, *292*, 686.

[5] R. Schlögl, *Angewandte Chemie International Edition in English* **1993**, *32*, 381.

[6] R. Schlögl, *Angewandte Chemie International Edition* **2015**, *54*, 3465.

[7] R. Schlögl, *Topics in Catalysis* **2016**, *59*, 772.

[8] A. Pantazidis, A. Auroux, J.-M. Herrmann, C. Mirodatos, *Catalysis Today* **1996**, *32*, 81.

[9] M. Caldararu, M. Scurtu, C. Hornoiu, C. Munteanu, T. Blasco, J. L. Nieto, *Catalysis Today* **2010**, *155*, 311.

[10] O. V. Safonova, B. Deniau, J.-M. M. Millet, *The Journal of Physical Chemistry B* **2006**, *110*, 23962.

[11] Z. Zhang, X. E. Verykios, M. Baerns, *Catalysis Reviews* **1994**, *36*, 507.

[12] F. Rouvet, J.-M. Herrmann, J.-C. Volta, *Journal of the Chemical Society, Faraday Transactions* **1994**, *90*, 1441.

[13] K. Ait-Lachgar, A. Tuel, M. Brun, J. Herrmann, J. Krafft, J. Martin, J. Volta, M. Abon, *Journal of Catalysis* **1998**, *177*, 224.

[14] M. Abon, J. Herrmann, J. Volta, *Catalysis Today* **2001**, *71*, 121.

[15] M. Eichelbaum, R. Stößer, A. Karpov, C.-K. Dobner, F. Rosowski, A. Trunschke, R. Schlögl, *Physical Chemistry Chemical Physics* **2012**, *14*, 1302.

[16] J. C. Slater, *Reviews of Modern Physics* **1946**, *18*, 441.

[17] M. Eichelbaum, R. Glaum, M. Hävecker, K. Wittich, C. Heine, H. Schwarz, C.-K. Dobner, C. Welker-Nieuwoudt, A. Trunschke, R. Schlögl, *ChemCatChem* **2013**, *5*, 2318.

[18] M. Eichelbaum, M. Hävecker, C. Heine, A. Karpov, C.-K. Dobner, F. Rosowski, A. Trunschke, R. Schlögl, *Angewandte Chemie International Edition* **2012**, *51*, 6246.

[19] C. Heine, M. Hävecker, E. Stotz, F. Rosowski, A. Knop-Gericke, A. Trunschke, M. Eichelbaum, R. Schlögl, *The Journal of Physical Chemistry C* **2014**, *118*, 20405.

[20] C. Heine, F. Girgsdies, A. Trunschke, R. Schlögl, M. Eichelbaum, *Applied Physics A* **2013**, *112*, 289.

[21] C. Heine, M. Hävecker, M. Sanchez-Sanchez, A. Trunschke, R. Schögl, M. Eichelbaum, *The Journal of Physical Chemistry C* **2013**, *117*, 26988.

[22] C. Heine, M. Hävecker, A. Trunschke, R. Schlögl, M. Eichelbaum, *Physical Chemistry Chemical Physics* **2015**, *17*, 8983.

[23] J. Schumann, M. Eichelbaum, T. Lunkenbein, N. Thomas, M. C. Alvarez Galvan, R. Schlögl, M. Behrens, *ACS Catalysis* **2015**, *5*, 3260.

[24] L. F. Chen, C. Ong, C. Neo, V. V. Varadan, V. K. Varadan, *Microwave Electronics: Measurement and Materials Characterization*, John Wiley & Sons, **2004**.

[25] E. Trukhan, *Instruments and Experimental Techniques-USSR* **1965**, 947.

[26] E. Trukhan, *Biofizika* **1966**, *11*, 412.

[27] D. Eley, R. Pethig, *Discussions of the Faraday Society* **1971**, *51*, 164.

[28] D. Eley, N. Lockhart, *Journal of Physics E: Scientific Instruments* **1983**, *16*, 47.

[29] R. Pethig, *Journal of Biological Physics* **1973**, *1*, 193.

[30] A. Al-Zoubi, O. Hasan, in *Journal of Physics: Conference Series*, Vol. 13, IOP Publishing, p. 430.

[31] N. Ong, W. Bauhofer, C.-J. Wei, *Review of Scientific Instruments* **1981**, *52*, 1367.

[32] C.-C. Liu, B.-K. Na, A. B. Walters, M. A. Vannice, *Catalysis Letters* **1994**, *26*, 9.

[33] S. Liu, Y. Nishina, R. Good Jr, *Review of Scientific Instruments* **1961**, *32*, 784.

[34] Y. Nishina, G. Danielson, *Review of Scientific Instruments* **1961**, *32*, 790.

[35] E. Prati, S. Faralli, M. Martinelli, G. Annino, G. Biasiol, L. Sorba, *Review of Scientific Instruments* **2003**, *74*, 154.

[36] A. R. Hutson, *Physical Review* **1957**, *108*, 222.

[37] A. Gire, M. Jouffroy, J.-G. Théobald, O. Bohnké, G. Frand, P. Lacorre, *Journal of Physics and Chemistry of Solids* **1997**, *58*, 577.

[38] B.-K. Na, A. Walters, M. Vannice, *Journal of Catalysis* **1993**, *140*, 585.

[39] B.-K. Na, M. A. Vannice, A. B. Walters, *Physical Review B* **1992**, *46*, 12266.

[40] H. Chon, J. Pajares, *Journal of Catalysis* **1969**, *14*, 257.

[41] A. Walters, B.-K. Na, C.-C. Liu, M. Vannice, *Journal of Molecular Catalysis A: Chemical* **2000**, *162*, 287.

[42] H. Chon, C. D. Prater, *Discussions of the Faraday Society* **1966**, *41*, 380.

[43] S. R. Morrison, *Journal of Catalysis* **1974**, *34*, 462.

[44] G.-M. Schwab, *Angewandte Chemie* **1961**, *73*, 399.

[45] F. F. Volkenshtein, *The Electronic Theory of Catalysis on Semiconductors*, Pergamon Press, **1963**.

[46] R. K. Grasselli, *Topics in Catalysis* **2002**, *21*, 79.

[47] M. Eichelbaum, M. Hävecker, C. Heine, A. M. Wernbacher, F. Rosowski, A. Trunschke, R. Schlögl, *Angewandte Chemie International Edition* **2015**, *54*, 2922.

[48] M. M. Lin, *Applied Catalysis A: General* **2001**, *207*, 1.

[49] G. Centi, F. Cavani, F. Trifirò, *Selective Oxidation by Heterogeneous Catalysis*, Springer Science & Business Media, **2012**.

[50] T. Ushikubo, H. Nakamura, Y. Koyasu, S. Wajiki, Method for producing an unsaturated carboxylic acid, **1995**, uS Patent 5,380,933.

[51] F. Cavani, F. Trifiro, *Applied Catalysis A: General* **1992**, *88*, 115.

[52] J.-C. Volta, *Comptes Rendus de l'Académie des Sciences-Series IIC-Chemistry* **2000**, *3*, 717.

[53] G. Centi, F. Trifiro, J. R. Ebner, V. M. Franchetti, *Chemical Reviews* **1988**, *88*, 55.

[54] M. Ai, *Journal of Catalysis* **1986**, *101*, 389.

[55] M. Ai, *Catalysis Today* **1992**, *13*, 679.

[56] G. Landi, L. Lisi, G. Russo, *Journal of Molecular Catalysis A Chemical* **2005**, *239*, 172.

[57] T. Quandt, *Untersuchung von VPO-Katalysatoren für die partielle Oxidation von Propan zu Acrylsäure*, PhD thesis, Dissertation Bochum, **1999**.

[58] R. Schlögl, *Topics in Catalysis* **2016**, *59*, 1461.

[59] R. Naumann d'Alnoncourt, L.-I. Csepei, M. Hävecker, F. Girgsdies, M. E. Schuster, R. Schlögl, A. Trunschke, *Journal of Catalysis* **2014**, *311*, 369.

[60] M. Lin, T. B. Desai, F. W. Kaiser, P. D. Klugherz, *Catalysis Today* **2000**, *61*, 223.

[61] A. Kaddouri, C. Mazzocchia, E. Tempesti, *Applied Catalysis A: General* **1999**, *180*, 271.

[62] E. A. Quadrelli, G. Centi, J.-L. Duplan, S. Perathoner, *ChemSusChem* **2011**, *4*, 1194.

[63] X. Lim, *Nature* **2015**, *526*, 628.

[64] H.-J. Freund, M. W. Roberts, *Surface Science Reports* **1996**, *25*, 225.

[65] G. Centi, S. Perathoner, *Catalysis Today* **2009**, *148*, 191.

[66] M. Bukhtiyarova, T. Lunkenbein, K. Kähler, R. Schlögl, *Catalysis Letters* **2017**, *147*, 416.

[67] M. Behrens, F. Studt, I. Kasatkin, S. Kühl, M. Hävecker, F. Abild-Pedersen, S. Zander, F. Girgsdies, P. Kurr, B.-L. Kniep, *Science* **2012**, *336*, 893.

[68] O.-S. Joo, K.-D. Jung, I. Moon, A. Y. Rozovskii, G. I. Lin, S.-H. Han, S.-J. Uhm, *Industrial & Engineering Chemistry Research* **1999**, *38*, 1808.

[69] K.-H. Ernst, C. T. Campbell, G. Moretti, *Journal of Catalysis* **1992**, *134*, 66.

[70] S.-I. Fujita, M. Usui, N. Takezawa, *Journal of Catalysis* **1992**, *134*, 220.

[71] M. Ginés, A. Marchi, C. Apesteguia, *Applied Catalysis A: General* **1997**, *154*, 155.

[72] T. Salmi, R. Hakkarainen, *Applied Catalysis* **1989**, *49*, 285.

[73] Y. Yang, C. A. Mims, D. Mei, C. H. Peden, C. T. Campbell, *Journal of Catalysis* **2013**, *298*, 10.

[74] J. Frost, *Nature* **1988**, *334*, 577.

[75] J. Yoshihara, J. Campbell, C. Campbell, *Surface Science* **1998**, *406*, 235.

[76] F. J. Sheini, J. Singh, O. Srivasatva, D. S. Joag, M. A. More, *Applied Surface Science* **2010**, *256*, 2110.

[77] C. Á. Galván, J. Schumann, M. Behrens, J. L. G. Fierro, R. Schlögl, E. Frei, *Applied Catalysis B: Environmental* **2016**, *195*, 104.

[78] J. Graciani, K. Mudiyanselage, F. Xu, A. E. Baber, J. Evans, S. D. Senanayake, D. J. Stacchiola, P. Liu, J. Hrbek, J. F. Sanz, et al., *Science* **2014**, *345*, 546.

[79] S. D. Senanayake, P. J. Ramirez, I. Waluyo, S. Kundu, K. Mudiyanselage, Z. Liu, Z. Liu, S. Axnanda, D. J. Stacchiola, J. Evans, et al., *The Journal of Physical Chemistry C* **2016**, *120*, 1778.

[80] S. Kuld, M. Thorhauge, H. Falsig, C. F. Elkjær, S. Helveg, I. Chorkendorff, J. Sehested, *Science* **2016**, *352*, 969.

[81] M. Behrens, *Angewandte Chemie* **2016**, *128*, 15128.

[82] J. D. Jackson, *Classical Electrodynamics*, Wiley, **1999**.

[83] A. Frieser, *Mikrowellenmesstechnik*, Akademie-Verlag Berlin, **1965**.

[84] R. P. Feynman, R. B. Leighton, M. Sands, *The Feynman Lectures on Physics Vol 2 Mainly Electromagnetism and Matter*, Addison-Wesley, **1979**.

[85] M. Abramowitz, I. A. Stegun, *Applied Mathematics Series* **1966**, *55*, 62.

[86] A. S. Khan, *Microwave Engineering: Concepts and Fundamentals*, CRC Press, **2014**.

[87] V. V. Tyurnev, *Progress In Electromagnetics Research B* **2010**, *21*, 47.

[88] G. R. Eaton, S. S. Eaton, D. P. Barr, R. T. Weber, *Quantitative EPR*, Springer Science & Business Media, **2010**.

[89] O. Klein, S. Donovan, M. Dressel, G. Grüner, *International Journal of Infrared and Millimeter Waves* **1993**, *14*, 2423.

[90] C. Heine, *The Electronic Structure of Vanadium Oxides as Catalysts in the Selective Oxidation of Small Alkanes*, PhD thesis, TU Berlin, **2014**.

[91] R. Waldron, *Proceedings of the IEE-Part C: Monographs* **1960**, *107*, 272.

[92] L. D. Landau, E. Lifshitz, *Course of Theoretical Physics. Vol. 8: Electrodynamics of Continuous Media*, Oxford, **1960**.

[93] H. Looyenga, *Physica* **1965**, *31*, 401.

[94] D. Dube, *Journal of Physics D: Applied Physics* **1970**, *3*, 1648.

[95] E. H. Hall, *American Journal of Mathematics* **1879**, *2*, 287.

[96] Y. Peter, M. Cardona, *Fundamentals of Semiconductors: Physics and Materials Properties*, Springer Science & Business Media, **2010**.

[97] H. Lüth, *Solid surfaces, Interfaces and Thin Films*, Vol. 4, Springer, **2001**.

[98] M. M. Sayed, C. R. Westgate, *Review of Scientific Instruments* **1975**, *46*, 1074.

[99] M. Schrape, H. Tributsch, M. Klein, F. Wünsch, M. Kunst, *Materials Science and Engineering B* **2003**, *102*, 409.

[100] N. Ong, *Journal of Applied Physics* **1977**, *48*, 2935.

[101] N. Ong, W. Bauhofer, C. jun Wei, *Review of Scientific Instruments* **1981**, *52*, 1367.

[102] D. Murthy, V. Subramanian, V. Murthy, *Review of Scientific Instruments* **2006**, *77*, 066108.

[103] W. Bauhofer, *Journal of Physics E: Scientific Instruments* **1981**, *14*, 934.

[104] B.-K. Na, S. Kelly, M. Vannice, A. B. Walters, *Measurement Science and Technology* **1991**, *2*, 770.

[105] R. J. Collier, A. D. Skinner, *Microwave Measurements*, Vol. 12, IET, **2007**.

[106] Fundamentals of vector network analysis version 1.1, `http://rohde-schwarz-scopes.com/designcon/VNA%20fundamentals%20primer.pdf`, accessed: 2016-12-04.

[107] P. J. Petersan, S. M. Anlage, *Journal of Applied Physics* **1998**, *84*, 3392.

[108] D. Kajfez, *Q factor Measurements using Matlab*, Artech House, **2011**.

[109] C. Nguyen, *Radio-frequency Integrated-circuit Engineering*, John Wiley & Sons, **2015**.

[110] H. Morkoç, Ü. Özgür, *Zinc oxide Fundamentals, Materials and Device Technology*, John Wiley & Sons, **2008**.

[111] H. Ibach, H. Lüth, *Advanced Texts in Physics, Springer-Verlag Berlin Heidelberg New York* **2003**.

[112] J. Fletcher, *Journal of Physics E: Scientific Instruments* **1976**, *9*, 481.

[113] M. Spencer, *Topics in Catalysis* **1999**, *8*, 259.

[114] J.-D. Grunwaldt, A. Molenbroek, N.-Y. Topsøe, H. Topsøe, B. Clausen, *Journal of Catalysis* **2000**, *194*, 452.

[115] G. Chinchen, K. Waugh, D. Whan, *Applied Catalysis* **1986**, *25*, 101.

[116] J. B. Hansen, P. E. Højlund Nielsen, *Handbook of Heterogeneous Catalysis* **2008**.

[117] Ü. Özgür, Y. I. Alivov, C. Liu, A. Teke, M. Reshchikov, S. Doğan, V. Avrutin, S.-J. Cho, H. Morkoc, *Journal of Applied Physics* **2005**, *98*, 041301.

[118] D. C. Look, *Materials Science and Engineering: B* **2001**, *80*, 383.

[119] D. P. Norton, Y. Heo, M. Ivill, K. Ip, S. Pearton, M. F. Chisholm, T. Steiner, *Materials Today* **2004**, *7*, 34.

[120] M. Behrens, G. Lolli, N. Muratova, I. Kasatkin, M. Hävecker, R. N. d'Alnoncourt, O. Storcheva, K. Köhler, M. Muhler, R. Schlögl, *Physical Chemistry Chemical Physics* **2013**, *15*, 1374.

[121] J. Han, P. Mantas, A. Senos, *Journal of the European Ceramic Society* **2001**, *21*, 1883.

[122] Z. Zhou, K. Kato, T. Komaki, M. Yoshino, H. Yukawa, M. Morinaga, K. Morita, *Journal of the European Ceramic Society* **2004**, *24*, 139.

[123] M. V. Twigg, M. S. Spencer, *Topics in Catalysis* **2003**, *22*, 191.

[124] M. Kurtz, N. Bauer, C. Büscher, H. Wilmer, O. Hinrichsen, R. Becker, S. Rabe, K. Merz, M. Driess, R. Fischer, *Catalysis Letters* **2004**, *92*, 49.

[125] M. Behrens, S. Zander, P. Kurr, N. Jacobsen, J. Senker, G. Koch, T. Ressler, R. W. Fischer, R. Schlögl, *Journal of the American Chemical Society* **2013**, *135*, 6061.

[126] G.-M. Schwab, J. Block, D. Schultze, *Angewandte Chemie* **1959**, *71*, 101.

[127] M. Saito, K. Murata, *Catalysis Surveys from Asia* **2004**, *8*, 285.

[128] R. Ulbricht, E. Hendry, J. Shan, T. F. Heinz, M. Bonn, *Reviews of Modern Physics* **2011**, *83*, 543.

[129] P. Drude, *Annalen der Physik* **1900**, *306*, 437.

[130] Y. Kobayashi, H. Nakai, F. Suzuki, Z. Ma, in *2007 Asia-Pacific Microwave Conference*, IEEE, pp. 1–4.

[131] J. Lloyd-Hughes, T.-I. Jeon, *Journal of Infrared, Millimeter, and Terahertz Waves* **2012**, *33*, 871.

[132] M. Dietrich, D. Rauch, A. Porch, R. Moos, *Sensors* **2014**, *14*, 16856.

[133] M. Behrens, *Journal of Catalysis* **2009**, *267*, 24.

[134] S. Sänze, A. Gurlo, C. Hess, *Angewandte Chemie International Edition* **2013**, *52*, 3607.

[135] N. Barsan, U. Weimar, *Journal of Physics: Condensed Matter* **2003**, *15*, R813.

[136] M. Tonouchi, *Nature Photonics* **2007**, *1*, 97.

[137] B. Ferguson, X.-C. Zhang, *Nature Materials* **2002**, *1*, 26.

[138] R. Farra, S. Wrabetz, M. E. Schuster, E. Stotz, N. G. Hamilton, A. P. Amrute, J. Pérez-Ramírez, N. López, D. Teschner, *Physical Chemistry Chemical Physics* **2013**, *15*, 3454.

[139] S. Basu, A. Dutta, *Sensors and Actuators B Chemical* **1994**, *22*, 83.

[140] N. Vorobyeva, M. Rumyantseva, R. Vasiliev, V. Kozlovskii, Y. M. Soshnikova, D. Filatova, A. Baranchikov, V. Ivanov, A. Gaskov, *Russian Journal of Inorganic Chemistry* **2014**, *59*, 403.

[141] R. Shannon, *Acta Crystallographica Section A: Crystal Physics, Diffraction, Theoretical and General Crystallography* **1976**, *32*, 751.

[142] C. G. Van de Walle, *Physical Review Letters* **2000**, *85*, 1012.

[143] C. F. Windisch Jr, G. J. Exarhos, C. Yao, L.-Q. Wang, *Journal of Applied Physics* **2007**, *101*, 123711.

[144] C. Kılıça, A. Zungerb, *Applied Physics Letters* **2002**, *81*, 73.

[145] D. Thomas, J. Lander, *The Journal of Chemical Physics* **1956**, *25*, 1136.

[146] N. Nickel, *Physical Review B* **2006**, *73*, 195204.

[147] C. Wang, G. Zhou, J. Li, B. Yan, W. Duan, *Physical Review B* **2008**, *77*, 245303.

[148] A. Usseinov, E. Kotomin, A. Akilbekov, Y. F. Zhukovskii, J. Purans, *Thin Solid Films* **2014**, *553*, 38.

[149] A. Katoch, S.-W. Choi, H. W. Kim, S. S. Kim, *Journal of Hazardous Materials* **2015**, *286*, 229.

[150] V. Khranovskyy, J. Eriksson, A. Lloyd-Spetz, R. Yakimova, L. Hultman, *Thin Solid Films* **2009**, *517*, 2073.

[151] H. Haneda, I. Sakaguchi, A. Watanabe, T. Ishigaki, J. Tanaka, *Journal of Electroceramics* **1999**, *4*, 41.

[152] M. Pollak, T. Geballe, *Physical Review* **1961**, *122*, 1742.

[153] A. K. Jonscher, *Nature* **1977**, *267*, 673.

[154] J. Sinkkonen, *Physica Status Solidi (b)* **1981**, *103*, 231.

[155] M. Beller, G. Centi, L. Sun, *ChemSusChem* **2017**, *10*, 6.

[156] G. Centi, F. Trifiro, *Catalysis Today* **1988**, *3*, 151.

[157] P. DeSanto Jr, D. Buttrey, R. Grasselli, W. Pyrz, C. Lugmair, A. Volpe Jr, T. Vogt, B. Toby, *Topics in Catalysis* **2006**, *38*, 31.

[158] Y. Moro-oka, W. Ueda, K.-H. Lee, *Journal of Molecular Catalysis A: Chemical* **2003**, *199*, 139.

[159] H. Murayama, D. Vitry, W. Ueda, G. Fuchs, M. Anne, J. Dubois, *Applied Catalysis A: General* **2007**, *318*, 137.

[160] D. Vitry, J.-L. Dubois, W. Ueda, *Journal of Molecular Catalysis A: Chemical* **2004**, *220*, 67.

[161] R. Schlögl, *Topics in Catalysis* **2011**, *54*, 627.

[162] K. Amakawa, Y. V. Kolen'ko, A. Villa, M. E. Schuster, L.-I. Csepei, G. Weinberg, S. Wrabetz, R. Naumann d'Alnoncourt, F. Girgsdies, L. Prati, *ACS Catalysis* **2013**, *3*, 1103.

[163] T. Ushikubo, H. Nakamura, Y. Koyasu, S. Wajiki, *Mitsubishi Kasei Corporation* **1997**.

[164] F. Cavani, *Catalysis Today* **2010**, *157*, 8.

[165] K. Kalz, R. Kraehnert, M. Dvoyashkin, R. Dittmeyer, R. Gläser, U. Krewer, K. Reuter, J.-D. Grunwaldt, *ChemCatChem* **2016**.

[166] J.-M. Herrmann, P. Vernoux, K. E. Béré, M. Abon, *Journal of Catalysis* **1997**, *167*, 106.

[167] P. Nguyen, R. Hoffman, A. Sleight, *Materials research bulletin* **1995**, *30*, 1055.

[168] M. Hävecker, A. Knop-Gericke, R. W. Mayer, M. Fait, H. Bluhm, R. Schlögl, *Journal of Electron Spectroscopy and related Phenomena* **2002**, *125*, 79.

[169] M. A. Pepera, J. L. Callahan, M. J. Desmond, E. C. Milberger, P. R. Blum, N. J. Bremer, *Journal of the American Chemical Society* **1985**, *107*, 4883.

[170] J. Haber, M. Witko, *Journal of Catalysis* **2003**, *216*, 416.

[171] V. Sokolovskii, *Catalysis Reviews Science and Engineering* **1990**, *32*, 1.

[172] J. C. Vedrine, G. Coudurier, J.-M. M. Millet, *Catalysis Today* **1997**, *33*, 3.

[173] J. C. Vedrine, J. M. M. Millet, J.-C. Volta, *Catalysis Today* **1996**, *32*, 115.

[174] A. C. Sanfiz, T. W. Hansen, D. Teschner, P. Schnörch, F. Girgsdies, A. Trunschke, R. Schlögl, M. H. Looi, S. B. A. Hamid, *The Journal of Physical Chemistry C* **2010**, *114*, 1912.

[175] H. Bluhm, M. Hävecker, A. Knop-Gericke, M. Kiskinova, R. Schlögl, M. Salmeron, *Mrs Bulletin* **2007**, *32*, 1022.

[176] E. M. Vass, M. Hävecker, S. Zafeiratos, D. Teschner, A. Knop-Gericke, R. Schlögl, *Journal of Physics: Condensed Matter* **2008**, *20*, 184016.

[177] S. Tanuma, C. Powell, D. Penn, *Surf. Interface Anal* **1993**, *21*, 165.

[178] H. Shinotsuka, S. Tanuma, C. Powell, D. Penn, *Surface and Interface Analysis* **2015**, *47*, 871.

[179] Casaxps software, `http://www.casaxps.com/`, accessed: 2017-01-17.

[180] Peak fitting in xps, `http://www.casaxps.com/help_manual/manual_updates/peak_fitting_in_xps.pdf`, accessed: 2017-01-17.

[181] R. Hesse, P. Streubel, R. Szargan, *Surface and Interface Analysis* **2005**, *37*, 589.

[182] Y. Ma, C. Chen, G. Meigs, K. Randall, F. Sette, *Physical Review A* **1991**, *44*, 1848.

[183] G. Landi, L. Lisi, J.-C. Volta, *Catalysis Today* **2004**, *91*, 275.

[184] E. Antonides, E. Janse, G. Sawatzky, *Physical Review B* **1977**, *15*, 4596.

[185] R. Zimmermann, R. Claessen, F. Reinert, P. Steiner, S. Hüfner, *Journal of Physics: Condensed Matter* **1998**, *10*, 5697.

[186] J. Taftø, O. Krivanek, *Physical Review Letters* **1982**, *48*, 560.

[187] J. Chen, C. Kirn, B. Frühberger, B. DeVries, M. Touvelle, *Surface Science* **1994**, *321*, 145.

[188] J. G. Chen, *Surface Science Reports* **1997**, *30*, 1.

[189] Y. Suchorski, L. Rihko-Struckmann, F. Klose, Y. Ye, M. Alandjiyska, K. Sundmacher, H. Weiss, *Applied Surface Science* **2005**, *249*, 231.

[190] M. Abon, K. Bere, A. Tuel, P. Delichere, *Journal of Catalysis* **1995**, *156*, 28.

[191] P. Delichere, K. Bere, M. Abon, *Applied Catalysis A: General* **1998**, *172*, 295.

[192] L. Rihko-Struckmann, Y. Ye, L. Chalakov, Y. Suchorski, H. Weiss, K. Sundmacher, *Catalysis Letters* **2006**, *109*, 89.

[193] G. Sawatzky, D. Post, *Physical Review B* **1979**, *20*, 1546.

[194] M. A. Eberhardt, A. Proctor, M. Houalla, D. M. Hercules, *Journal of Catalysis* **1996**, *160*, 27.

[195] L. Cornaglia, E. Lombardo, *Applied Catalysis A: General* **1995**, *127*, 125.

[196] A. Trunschke, J. Noack, S. Trojanov, F. Girgsdies, T. Lunkenbein, V. Pfeifer, M. Hävecker, P. Kube, C. Sprung, F. Rosowski, R. Schlögl, *in preparation* **2017**.

[197] N. H. Batis, H. Batis, A. Ghorbel, J. Vedrine, J. Volta, *Journal of Catalysis* **1991**, *128*, 248.

[198] S. Hüfner, *Photoelectron Spectroscopy: Principles and Applications*, Springer Science & Business Media, **2013**.

[199] M. Alonso, R. Cimino, K. Horn, *Physical Review Letters* **1990**, *64*, 1947.

[200] R. L. Kurtz, V. E. Henrich, *Physical Review B* **1983**, *28*, 6699.

[201] R. L. Kurtz, V. E. Henrich, *Physical Review B* **1987**, *36*, 3413.

[202] M. Helander, M. Greiner, Z. Wang, Z. Lu, *Applied Surface Science* **2010**, *256*, 2602.

[203] J. Meyer, K. Zilberberg, T. Riedl, A. Kahn, *Journal of Applied Physics* **2011**, *110*, 033710.

[204] A. Gurlo, R. Riedel, *Angewandte Chemie International Edition* **2007**, *46*, 3826.

[205] Y. Nishina, W. Spry, *Journal of Applied Physics* **1958**, *29*, 230.

[206] R. Stößer, U. Marx, W. Herrmann, J. K. Jabor, A. Brückner, *Journal of the American Chemical Society* **2010**, *132*, 9873.

[207] F. Wang, R. Büchel, A. Savitsky, M. Zalibera, D. Widmann, S. E. Pratsinis, W. Lubitz, F. Schüth, *ACS Catalysis* **2016**, *6*, 3520.

[208] E. Trukhan, *Radio Eng. & Electron. Phys* **1966**, *15*, 1097.

[209] S. M. Sze, K. K. Ng, *Physics of Semiconductor Devices*, John Wiley & Sons, **2006**.

[210] D. C. Look, D. C. Reynolds, J. Sizelove, R. Jones, C. W. Litton, G. Cantwell, W. Harsch, *Solid State Communications* **1998**, *105*, 399.

[211] J. Albrecht, P. Ruden, S. Limpijumnong, W. Lambrecht, K. Brennan, *Journal of Applied Physics* **1999**, *86*, 6864.

[212] H. Rupprecht, *Journal of Physics and Chemistry of Solids* **1958**, *6*, 144.

[213] A. Hutson, *Journal of Physics and Chemistry of Solids* **1959**, *8*, 467.

[214] M. Behrens, *Angewandte Chemie International Edition* **2016**, *55*, 14906.

[215] R. N. d'Alnoncourt, X. Xia, J. Strunk, E. Löffler, O. Hinrichsen, M. Muhler, *Physical Chemistry Chemical Physics* **2006**, *8*, 1525.

[216] T. Lunkenbein, J. Schumann, M. Behrens, R. Schlögl, M. G. Willinger, *Angewandte Chemie* **2015**, *127*, 4627.

[217] B.-K. Na, *Measurement of electrical properties of small particles, using a microwave Hall effect (MHE) technique*, PhD thesis, The Pennsylvania State University, **1991**.

[218] G. Chinchen, P. Denny, J. Jennings, M. Spencer, K. Waugh, *Applied Catalysis* **1988**, *36*, 1.

[219] T. Lunkenbein, F. Girgsdies, T. Kandemir, N. Thomas, M. Behrens, R. Schlögl, E. Frei, *Angewandte Chemie* **2016**, *128*, 12900.

[220] D. Grenoble, M. Estadt, D. Ollis, *Journal of Catalysis* **1981**, *67*, 90.

[221] S.-G. Wang, D.-B. Cao, Y.-W. Li, J. Wang, H. Jiao, *The Journal of Physical Chemistry B* **2005**, *109*, 18956.

[222] J. Ko, B.-K. Kim, J. W. Han, *The Journal of Physical Chemistry C* **2016**, *120*, 3438.

[223] G. Chinchen, C. Hay, H. Vandervell, K. Waugh, *Journal of Catalysis* **1987**, *103*, 79.

[224] M. B. Fichtl, J. Schumann, I. Kasatkin, N. Jacobsen, M. Behrens, R. Schlögl, M. Muhler, O. Hinrichsen, *Angewandte Chemie International Edition* **2014**, *53*, 7043.

[225] S. Polarz, J. Strunk, V. Ischenko, M. W. Van den Berg, O. Hinrichsen, M. Muhler, M. Driess, *Angewandte Chemie International Edition* **2006**, *45*, 2965.

[226] M. Kurtz, J. Strunk, O. Hinrichsen, M. Muhler, K. Fink, B. Meyer, C. Wöll, *Angewandte Chemie International Edition* **2005**, *44*, 2790.

[227] S. Kuld, C. Conradsen, P. G. Moses, I. Chorkendorff, J. Sehested, *Angewandte Chemie International Edition* **2014**, *53*, 5941.

[228] S. B. Orlinskii, J. Schmidt, P. G. Baranov, V. Lorrmann, I. Riedel, D. Rauh, V. Dyakonov, *Physical Review B* **2008**, *77*, 115334.

[229] G. Dutta, A. A. Sokol, C. R. A. Catlow, T. W. Keal, P. Sherwood, *ChemPhysChem* **2012**, *13*, 3453.

[230] G.-M. Schwab, *Angewandte Chemie International Edition in English* **1967**, *6*, 375.

[231] Y. Wang, R. Kováčik, B. Meyer, K. Kotsis, D. Stodt, V. Staemmler, H. Qiu, F. Traeger, D. Langenberg, M. Muhler, *Angewandte Chemie International Edition* **2007**, *46*, 5624.

[232] A. Frieser, *Mikrowellenmesstechnik*, Akademie Verlag, Berlin, **1965**.

[233] H. Kawabata, H. Tanpo, Y. Kobayashi, *IEICE Transactions on Electronics* **2003**, *86*, 2371.

[234] R. Collins, D. Kleinman, *Journal of Physics and Chemistry of Solids* **1959**, *11*, 190.

[235] C. Arguello, D. Rousseau, S. P. d. S. Porto, *Physical Review* **1969**, *181*, 1351.

[236] A. Aruchamy, *Photoelectrochemistry and photovoltaics of layered semiconductors*, Vol. 14, Springer Science & Business Media, **2013**.

[237] F. M. John, F. S. William, E. S. Peter, D. Kenneth, *Perkin-Elmer Corporation Physical Electronics Division* **1992**.

[238] C.-C. Liu, *Measurement of electrical properties of powders using microwave Hall effect and absorption techniques*, PhD thesis, The Pennsylvania State University, **1995**.

[239] C.-C. Liu, A. Walters, M. Vannice, *Carbon* **1995**, *33*, 1699.

[240] P. W. Stephens, *Journal of Applied Crystallography* **1999**, *32*, 281.